

**Measurement of Xenon Diffusing Capacity by Hyperpolarized
 ^{129}Xe MR Imaging and Dynamic Spectroscopy in Rats with
Stachybotrys chartarum Spore Induced Pneumonitis**

by

Nishard Abdeen

B.Sc. (Acadia University) 1984

M.D.C.M (McGill University) 1988

A thesis submitted to
the Faculty of Graduate Studies and Research
in partial fulfillment of
the requirements for the degree of
Master of Science

Department of Physics

Carleton University

Ottawa, Ontario

May 30, 2005

©2005, Nishard Abdeen



Library and
Archives Canada

Bibliothèque et
Archives Canada

Published Heritage
Branch

Direction du
Patrimoine de l'édition

395 Wellington Street
Ottawa ON K1A 0N4
Canada

395, rue Wellington
Ottawa ON K1A 0N4
Canada

Your file *Votre référence*
ISBN: 0-494-10130-X
Our file *Notre référence*
ISBN: 0-494-10130-X

NOTICE:

The author has granted a non-exclusive license allowing Library and Archives Canada to reproduce, publish, archive, preserve, conserve, communicate to the public by telecommunication or on the Internet, loan, distribute and sell theses worldwide, for commercial or non-commercial purposes, in microform, paper, electronic and/or any other formats.

The author retains copyright ownership and moral rights in this thesis. Neither the thesis nor substantial extracts from it may be printed or otherwise reproduced without the author's permission.

AVIS:

L'auteur a accordé une licence non exclusive permettant à la Bibliothèque et Archives Canada de reproduire, publier, archiver, sauvegarder, conserver, transmettre au public par télécommunication ou par l'Internet, prêter, distribuer et vendre des thèses partout dans le monde, à des fins commerciales ou autres, sur support microforme, papier, électronique et/ou autres formats.

L'auteur conserve la propriété du droit d'auteur et des droits moraux qui protègent cette thèse. Ni la thèse ni des extraits substantiels de celle-ci ne doivent être imprimés ou autrement reproduits sans son autorisation.

In compliance with the Canadian Privacy Act some supporting forms may have been removed from this thesis.

Conformément à la loi canadienne sur la protection de la vie privée, quelques formulaires secondaires ont été enlevés de cette thèse.

While these forms may be included in the document page count, their removal does not represent any loss of content from the thesis.

Bien que ces formulaires aient inclus dans la pagination, il n'y aura aucun contenu manquant.


Canada

Abstract

A novel non invasive measurement of gas exchange in rat lung, the xenon diffusing capacity, was defined analogously to the carbon monoxide diffusion capacity as the product of alveolar volume (determined by hyperpolarized ^{129}Xe MR imaging volumetry) and the reciprocal of the gas transfer time of xenon from the alveoli into the lung parenchyma and red blood cells (determined by hyperpolarized ^{129}Xe dynamic spectroscopy). The hypothesis that these measures could distinguish diseased and control rats was tested in a rat model of pneumonitis induced by fungal (*Stachybotrys chartarum*) spores. Lung volumes (11 ± 2 ml vs 16 ± 2 ml, $p<0.01$) were lower and the gas transfer times for the lung parenchyma were longer (35 ± 8 ms vs 22 ± 3 ms, $p<0.01$) in the spore instilled rats ($n=6$). The lung parenchyma component of the diffusion capacity for xenon was significantly lower for the diseased group (27 ± 9 ml/min/mmHg vs 57 ± 10 ml/min/mmHg, $p<0.001$). The red blood cell component of the diffusion capacity of xenon was not significantly different and showed considerable variation in diseased vs control rats (42 ± 27 ml/min/mmHg vs. 64 ± 35 ml/min/mmHg, $p<0.15$). These results provide quantification of gas exchange abnormalities in fungal spore induced pneumonitis, as well as resolution of diffusion capacity into a red blood cell component and a lung parenchyma component. The technique can easily be applied to other models of lung disease and may have potential applications in clinical medicine.

Acknowledgements

I would like to thank my supervisor, Giles Santyr, for his guidance and support throughout this project, particularly with respect to the high standard of intellectual rigour he exemplified, as well as his monumental patience and tact. His encouragement and motivation was much appreciated.

I would like to thank my wife, Judith Linthorst, and my children Jozephine, Rhys, and Lienke, for their steadfast love and support .

A large number of people provided scientific and technical backing for the project, as well as becoming friends. Albert Cross wrote the pulse sequences and did most of the technical development. Greg Cron taught me rat surgery. Steve White's thesis work on xenon volume measurements was essential for the work described here. Mihai Gherase, Ken Nkongchu, and Julia Wallace were generous with their time, advice and experience. Thomas Walker provided assistance with many experiments.

Collinda Thivierge and Ann Hogarth at the Carleton Animal Care Centre were unfailingly helpful with issues related to animal care and anesthesia. Diane Trenouth was very helpful with respect to protocols.

Dr. Thomas Rand at St. Mary's University in Halifax provided the spore instilled rats and did the histological grading. Dr. David Miller suggested *Stachybotrys chartarum* as a disease model.

Table of Contents

Abstract	iii
Acknowledgements	iv
Table of Contents	v
List of Tables	ix
List of Figures	x
List of Abbreviations	xii
1. Introduction	1
1.1 Introduction to Thesis.....	1
1.2 Gas exchange in the lung.....	1
1.3 Experimental Measurements of Gas Exchange.....	5
1.3.1 Alveolar Arterial Oxygen Tension.....	7
1.3.2 Distribution of Ventilation.....	8
1.3.3 Distribution of Perfusion.....	9
1.3.3.1 Single breath radioactive labelled CO ₂	9
1.3.3.2 Radiolabelled Macroaggregated Albumen Particles.....	10
1.3.3.3 Plastic Microspheres.....	10
1.3.4 Ventilation-Perfusion Relationships.....	11
1.3.4.1 Radionuclide Ventilation-Perfusion Scan.....	11
1.3.4.2 Multiple Inert Gas Elimination Technique (MIGET).....	12
1.3.5 Diffusing Capacities for Oxygen and CO ₂	13

1.4 Carbon Monoxide Lung Diffusing Capacity (D_{LCO}).....	14
1.5 Rat models of lung disease.....	19
1.5.1 <i>Stachybotrys chartarum</i> Spore Induced Pneumonitis.....	19
1.5.2 Other Models of Lung Inflammation in Rats.....	20
1.6 Hyperpolarized ^{129}Xe	20
1.6.1 Hyperpolarization of Xenon by Spin Exchange.....	22
1.6.2 Applications of Hyperpolarized Xenon <i>in vivo</i>	26
1.7 Rationale for a Xenon Lung Diffusing Capacity.....	30
1.8 Hypotheses.....	32
1.9 Organization of Thesis.....	33
2. Theory.....	35
2.1 Review of NMR spectroscopy.....	35
2.1.1 Spin, Magnetic Moment, and Larmor Precession Frequency.....	35
2.1.2 Bloch Equation, Excitation by Radio-frequency (RF) Pulses, and Rotating Frame.....	39
2.1.3 Free Induction Decay, NMR spectra, and the Fourier Transform.....	44
2.1.4 Frequency Selective RF Pulses and Magnetization Transfer.....	46
2.2 Magnetic Resonance Imaging	47
2.2.1 General MRI Principles.....	47
2.2.2 PulseSequencesforImaging.....	52
2.2.3 Hyperpolarized Xenon MRI.....	55
2.3 Derivation of Xenon Diffusing Capacity for Red Blood Cells and Lung	61
3. Methods.....	66
3.1 MR Imaging Equipment.....	66
3.2 Pulse Sequences.....	66
3.3 Imaging Procedure.....	69
3.4 Production of Hyperpolarized Xenon.....	70

3.5 Animal Preparation and Histology Grading.....	72
3.6 Data Analysis.....	73
3.6.1 Volume Calculation.....	73
3.6.2 Determination of Gas Transfer Times (T_{tr}).....	76
3.6.3 Calculation of Diffusing Capacities.....	77
3.6.4 Statistical Analysis.....	77
4. Results.....	79
4.1 Hyperpolarized Xenon Spectroscopy.....	79
4.1.1 Typical Spectrum of Hyperpolarized ^{129}Xe in rat lung <i>in vivo</i>	79
4.1.2 Gas Transfer Curves for Diseased and Control Rats.....	80
4.2 Hyperpolarized ^{129}Xe MRI and Volume Measurements.....	80
4.3 Xenon Diffusion Capacities.....	81
4.4 Histological Grade of Lung Inflammation.....	81
4.5 Comparison of the Control and Diseased Groups.....	81
5. Discussion and Future Work.....	94
5.1 Restatement of Results and Comparison with Previous Work.....	94
5.2 Comparison of Xenon Diffusing Capacity and D_{LCO}	95
5.3 Interpretation of Current Results.....	96
5.4 Sources of Error.....	99
5.5 Future Work and Conclusion.....	100
5.5.1 Measurement of Xenon Diffusing Capacity in other Experimental Models of Lung Disease.....	100
5.5.2 Measurement of Xenon Diffusing Capacity in Human Subjects.....	102

5.5.3 Conclusions.....103

6. References.....106

List of Tables

4.1 Comparison of gas transfer times and lung volumes for individual control and diseased rats.....	86
4.2 Comparison of D_{LXeRBC} , D_{LXeLP} , and D_{LXe} for individual control and diseased rats...	86
4.3 Comparison of parameter means (\pm S.D.) for the control and diseased groups.....	87

List of Figures

1.1 Overview of gas exchange processes.....	3
1.2 Lung anatomy: bronchioles, alveoli and capillaries.....	4
1.3 Spin exchange polarization of rubidium by circularly polarized light.....	23
1.4 Transfer of angular momentum in a three body collision between Rb,N ₂ and ¹²⁹ Xe.....	24
1.5 The single alveolar diffusion model.....	29
2.1. Magnetization response to RF pulse in lab and in rotating frames of reference.....	40
2.2 Graphical View of excitation showing reduction of z component of B _{eff} in the rotating frame.....	43
2.3 Frequency selective pulse in time and frequency domain.....	49
2.4 Gradient echo pulse sequence.	56
2.5 k-space trajectory for gradient echo pulse sequence.....	57
2.6 3-D FT pulse sequence.....	58
3.1 Spectroscopy pulse sequence	67
3.2 Experimental apparatus.....	71
4.1 Typical in vivo spectrum from rat lung.....	82

4.2	Stacked plot of spectra obtained during a single breath-hold.....	83
4.3 a.	Representative gas transfer curve for lung parenchyma (spore rat 2).....	84
4.3 b.	Representative gas transfer curve for RBC (spore rat 2).....	84
4.4 a.	Representative gas transfer curve for lung parenchyma (control rat 1).....	85
4.4 b.	Representative gas transfer curve for RBC (control rat 1).....	85
4.5	Volumetric 3-D image of hyperpolarized ^{129}Xe in rat lung.....	88
4.6	Photomicrographs of grade 1 and 2 inflammation in spore instilled rat lungs.....	89
4.7	Photomicrographs of grade 3 and 4 inflammation in spore instilled rat lungs.....	90
4.8	Correlation of xenon diffusing capacity for lung parenchyma (D_{LXeLP}) with histology grade.....	91
4.9	Correlation of xenon diffusing capacity for red blood cells (D_{LXeRBC}) with histology grade.....	92
4.10	Correlation of xenon diffusing capacity for lung (D_{LXe}) with histology grade.....	93
5.1	Comparison of normal and diseased groups with respect to measured Parameters.....	104
5.2	Comparison of normal and diseased groups with respect to calculated Parameters.....	105

List of Abbreviations

SNR: signal to noise ratio

D_{LCO} : lung diffusing capacity for carbon monoxide

D_{LXeLP} : lung diffusing capacity for xenon (lung parenchyma)

D_{LXeRBC} : lung diffusing capacity for xenon (red blood cells)

D_{LXe} : lung diffusing capacity for xenon (combined)

T_{tr} : gas transfer time

LPS: lipopolysaccharide

k_{CO} : transfer coefficient for carbon monoxide

V_A : alveolar volume

TLC: total lung capacity

GE: gradient echo

SE: spin echo

FT: Fourier transform

RF: radiofrequency

TE: echo time

TR: repetition time

T_1 : longitudinal relaxation time

T_2 : transverse relaxation time

LP: lung parenchyma (epithelial cells and interstitium of lung)

RBC: red blood cell

STPD: standard temperature and pressure dry

1.Introduction

1.1 Introduction to the Thesis

This thesis presents a novel method of measuring gas exchange in the lung *in vivo*, the xenon diffusing capacity. This is a physiological measurement carried out using ^{129}Xe dynamic spectroscopy and MR imaging. Chapter 1 reviews several background topics of relevance. First, gas exchange and various experimental methods for quantifying it are discussed, including the well established carbon monoxide diffusing capacity or D_{LCO} on which the xenon diffusing capacity is conceptually based. Various models of lung disease in rats are discussed, including the fungal spore inhalation model used to validate the efficacy of the xenon diffusing capacity to detect lung disease. Hyperpolarized ^{129}Xe is introduced and previous work in its application to pulmonary physiology is reviewed. The rationale for a xenon diffusing capacity is developed, and finally the remaining chapters of the thesis are outlined.

This work has been submitted for publication to the journal *Magnetic Resonance in Medicine* under the title “Measurement of Xenon Diffusing Capacity in the Rat Lung by Hyperpolarized ^{129}Xe MR Imaging and Dynamic Spectroscopy in a Single Breath-hold”.

1.2 Gas exchange in the lung

Measurement of gas exchange in the lung is an important area of research. Oxygen transport forms the basis of energy generation in the mitochondria and is essential for

organ function and life in aerobic organisms. The pathway which transports oxygen from the environment to the mitochondria involves coupling between the lungs, heart and circulation, and tissues, of which a schematic diagram is shown in Figure 1.1. Although this is an integrated process, where gas exchange in the lungs is coupled in poorly understood ways to oxygen consumption by tissues, the gas exchange in the lungs is an important component [1]. The main processes occurring in the lungs are ventilation (from mouth to alveoli) and diffusion (from alveoli into blood). Ventilation consists of convective gas flow along a pressure gradient down the branching tree like structure of airways (mainly in the first 17 generations of airways) and diffusive mixing (mainly in subsequent airways to the alveoli at generation 23) [1]. The anatomy of the alveoli is shown in Figure 1.2. The transport of gas across the alveoli into capillary blood is governed by passive diffusion along a concentration gradient. Ventilation/perfusion mismatch refers to the degree to which ventilation and pulmonary capillary blood flow are not distributed to the same alveoli. The greater the mismatch, the more impaired the gas exchange. Furthermore, the completeness of oxygen diffusion across the capillary membrane depends on three factors: the nature of the alveolar capillary membrane, the rate of blood flow through the capillaries, and the number of oxygen binding sites in the blood [2].

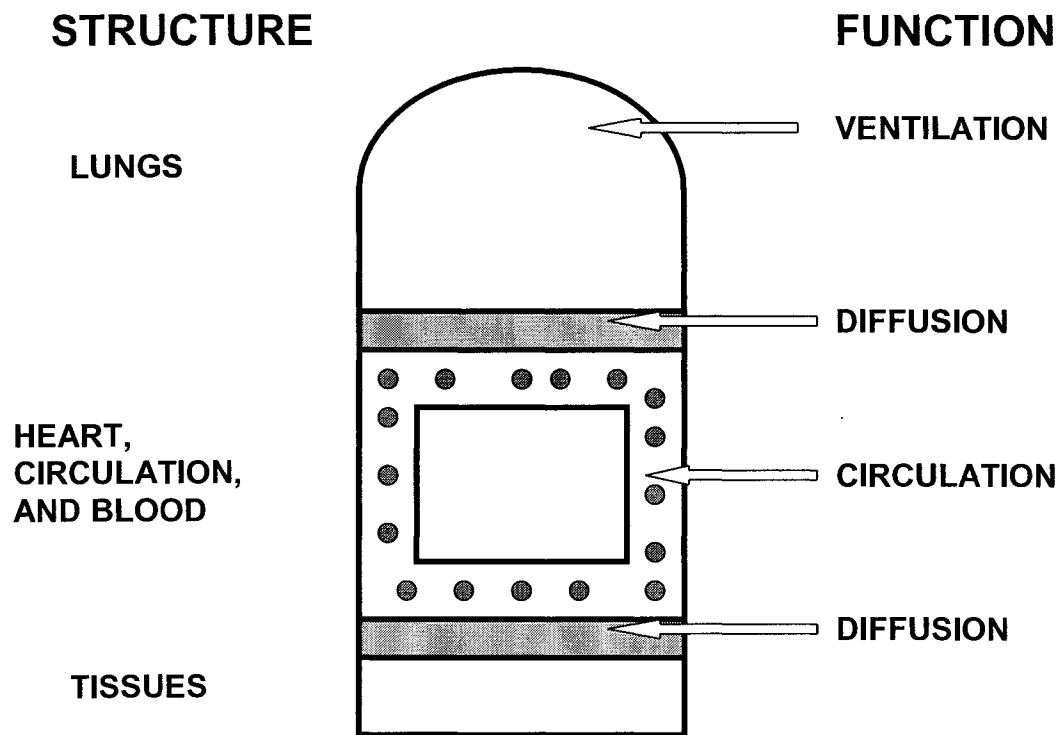


Figure 1.1
Overview of gas exchange processes
 adapted from [1].

Respiratory disease can affect all of the above steps, leading to impairment of gas exchange in a complex fashion. Measurement of these processes therefore can lead to improved understanding and hence to improved diagnosis and therapy.

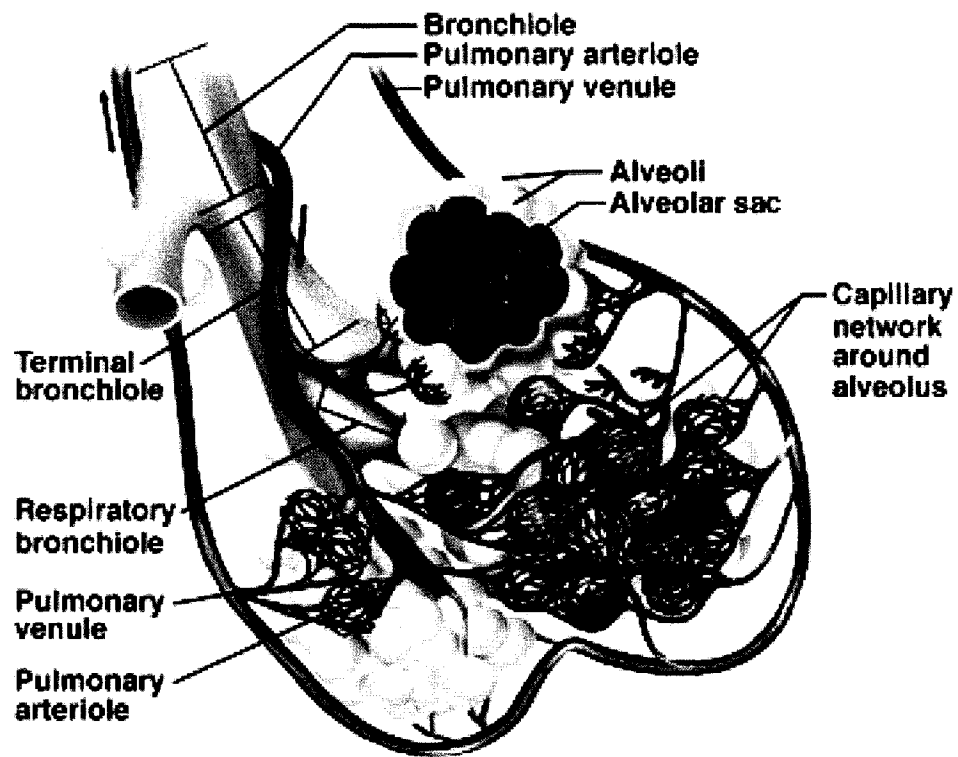


Figure 1.2
Lung anatomy: bronchioles, alveoli and capillaries.
Source: *www.bio.bmb.psu.edu*

Lung diseases constitute a common cause of mortality and morbidity, and are increasing in incidence. Chronic obstructive pulmonary disease or COPD currently ranks as the fourth leading cause of death in the United States, after heart disease, cancer, and

cerebrovascular disease [3,4]. COPD, for which prevalence and mortality rates continue to rise, constitutes an important worldwide burden which is projected to become the fifth most common disease by 2020 [5]. Improved diagnosis leading to better treatment would have a significant impact.

The advent of genome sequencing and the development of mouse models of lung disease characterized by gene deletions (“knockout mice”) has led to renewed interest in methods of evaluating lung disease phenotypes rapidly [6]. In particular, imaging of lungs of small mammals has been found to be an effective means of establishing structural and functional abnormalities in lung disease models [7]. An important application of such screening includes evaluation of novel therapies, including drug development. Measurements of gas exchange can serve to identify improvements in proxy endpoints in experimental animals. The evaluation of a candidate drug is often long and costly, and any means of reducing the time required or increasing the number of drugs screened would be economically important. Therefore, measurement of gas exchange is important in both fundamental and applied biomedical research.

1.3 Experimental Measurements of Gas Exchange

The lung consists of a fractally branching system of bronchi which terminate in air sacs or alveoli (see Figure 1.2). There are 300 million alveoli with a total surface area of 70-100 square meters and 23 generations of airways in the human lung [8]. The larger airways are termed bronchi and contain cartilage whereas smaller airways without cartilage are bronchioles. The diameter of airways varies from 2-3 cm down to 0.5 mm for the smallest terminal bronchioles. The terminal bronchioles give way to respiratory bronchioles which

branch into alveolar ducts (about 100) and finally alveoli (about 2000). All alveoli arising from a first respiratory bronchiole form a functional unit and are perfused by the branch of the pulmonary artery which accompanies that respiratory bronchiole. Each such unit is 5 mm in diameter and has a volume of 0.02 ml at functional residual capacity (lung volume at normal expiration). Each alveolus has a wall thickness of 5-6 μm and a diameter of about 200-330 μm at 75% lung volume [9]. Ventilation of the alveoli depends on convection and diffusion. Convective flow dominates air movement from the mouth to about the 17th generation of bronchi; the volume of this space is the dead space and is washed out with each breath as it is much less than the volume of air in each breath. Beyond airway generation 17 until the alveoli are reached at generation 23, diffusion is predominant. In this part of the lung, the volume is much larger (total lung capacity is 3-4 litres and tidal volume or volume of a normal breath is 500 ml) and gas mixing typically occurs [9].

The pulmonary vasculature arises in the outflow tract of the right ventricle as the main pulmonary artery, which branches into right and left pulmonary arteries and continues to branch into smaller pulmonary arteries (>0.5 mm) and the pulmonary arterioles (0.5-0.013 mm), which branch into pulmonary capillaries (0.010 mm). The capillaries are large in number and constitute 50-70 m^2 in surface area compared to 0.2 m^2 for pulmonary arteries and 1 m^2 for the pulmonary arterioles. The capillaries drain into pulmonary venules which drain into pulmonary veins, the main pulmonary vein and return to the left atrium of the heart. The pulmonary capillaries form a network ideally suited for gas exchange. Each capillary loops over 5-6 alveoli and the average red blood cell transit

time through the 0.6-0.8mm diameter capillary is approximately 0.8 s [10]. Indirect estimates in man are 0.5-1.0 s [11, 12] and 0.3-1.5s in dogs [10].

Oxygen diffusion and chemical reaction with hemoglobin is complete within 0.25 –0.35 s [31,13] so the extra transit time is available for physiological reserve during exercise, when transit time is reduced to approximately 0.25 s.

There are many techniques for assessing gas exchange in the lungs. They include anatomical and functional measurements of ventilatory capacity (\dot{V}), diffusing capacity, alveolar-arterial oxygen gradient, and cardiac output or perfusion (\dot{Q}), as well as ventilation/perfusion inequality (\dot{V}/\dot{Q}). This section will review experimental methods of assessing the efficiency of gas exchange, except for the important method of carbon monoxide diffusing capacity, which will be discussed in the subsequent section.

1.3.1 Alveolar Arterial Oxygen Tension

The difference between alveolar and arterial P_{O_2} (the alveolar-arterial gradient) is a simple measure of gas exchange. Arterial P_{O_2} is easily measured. Alveolar P_{O_2} is less easy to measure and must be estimated by a variety of methods. A simplified model [14] leads to the following equation for P_{O_2} as a function of arterial P_{CO_2} (P_{aCO_2}), inspired P_{O_2} (P_{AO_2}), fraction of O_2 in the inspired gas (F_{IO_2}), and fraction of N_2 in the inspired gas (F_{IN_2}):

$$P_{AO_2} = P_{IO_2} - P_{aCO_2} \cdot (F_{IO_2} - F_{IN_2}). \quad (1.1)$$

The advantage of this is that it is a practical clinical index of gas exchange. The higher the gradient the worse the gas exchange. The disadvantage is that it requires arterial blood sampling and does not define the mechanism of the barrier to gas exchange.

1.3.2 Distribution of Ventilation

A number of gas inhalation methods requiring a single breath or multiple breaths of inert gases (e.g. nitrogen, helium, sulfur hexafluoride) are available to measure inhomogeneity of ventilation [1]. It can be shown that the washout of inert gas is given by the equation :

$$\ln F_{A_n} = \ln F_{A_0} + n \cdot \ln R_D. \quad (1.2)$$

where F_{A_0} is the initial fractional concentration of the inert gas in the lung, F_{A_n} is the fractional concentration after n breaths, and R_D is the dilution ratio of resident alveolar gas given by :

$$R_D = \frac{1}{1 + \dot{V}_A t / V_A} \quad (1.3)$$

where \dot{V}_A is alveolar ventilation, t is the breathhold time and V_A is alveolar volume. The fractional concentrations are measured as the concentration at which the expired air plateaus. A plot of $\ln F_{A_n}$ vs the number of breaths n is linear for a homogeneous lung, and curvilinear for an inhomogeneously ventilated lung. Up to three components of the

exponential decay can be fitted, corresponding to three functional compartments of ventilation. The main advantage of the technique is simplicity. The main disadvantage is that only a limited number of compartments can be resolved.

Radioactive tracer gases (e.g. ^{133}Xe) have also been used in a single breath method to quantify ventilatory distribution between upper and dependent lung in different body positions, by measuring regional count rates with a gamma camera or gamma probe placed at different chest locations [15,16]. The main disadvantage of this technique is the exposure to radioactivity and poor spatial resolution as well as limited applicability in small animal subjects.

1.3.3 Distribution of Perfusion

1.3.3.1 Single Breath Radioactive Labelled CO_2

Gamma counting of CO_2 labelled with ^{15}O has been performed with subjects taking a single 15 second breath-hold of 3% CO_2 [17]. The CO_2 disappearance from the lung is blood flow limited unlike O_2 or CO which are removed partly by diffusion and partly by blood flow. The total blood flow or cardiac output is defined as \dot{Q} . Regional blood flow per unit lung volume (\dot{Q}_r/V_r) is calculated according to :

$$\frac{\dot{Q}_r}{V_r} = \frac{1}{\alpha(P_B - 47)} \cdot \left[\frac{\Delta \ln(CR_f)}{\Delta t} - k \right] \quad (1.4)$$

where α is the Bunsen solubility coefficient for CO_2 in blood (ml gas dissolved per ml blood at 273 K), P_B is the barometric pressure, k is the rate constant for the radioactive decay of ^{15}O , and $\Delta \ln(CR_f)/\Delta t$ is the log slope of the decay of the regional count rate CR_f . Four stacked pairs of probes have been used to demonstrate the decline in regional blood flow per unit volume from base to apex. The main disadvantage is exposure to radioactivity.

1.3.3.2 Radiolabelled Macroaggregated Albumen Particles

Regional distribution of perfusion can be measured with technetium-99m labelled macroaggregated albumen particles 10-30 microns in diameter. Approximately 100,000-300,000 particles labelled with $2\mu\text{Ci}$ of $^{99\text{m}}\text{Tc}$ are injected through an intravenous catheter and regional counts recorded with a gamma camera. The patient is usually in a supine position to minimize gravitational effects. Single photon emission computed tomography can be used to quantify regional count rates although for clinical use the scan is evaluated for perfusion defects by eye. The most common use of this technique clinically has been in ventilation-perfusion scans for the diagnosis of pulmonary embolism [1]. The advantage of this technique is its ease of performance while the disadvantage is exposure to radioactivity.

1.3.3.3 Plastic Microspheres

Plastic microspheres (15-25 μm in diameter) labelled with colored dyes or gamma emitting isotopes can be injected intravenously. The density of microsphere trapping is proportional to the local blood flow in the lungs. The lungs are removed after injection, and the excised lungs embedded in urethane foam. The sectioned lungs can then be scanned spectrophotometrically or with a gamma camera to determine the density of microspheres and hence the local blood flow under the conditions of the experiment [18]. This technique has the disadvantage of only being applicable post mortem, but since multiple colored dyes or multiple energies of gamma emitters can be used, measurements of blood flow under multiple different conditions can be made in the same lung.

1.3.4 Ventilation-Perfusion Relationships

1.3.4.1 Radionuclide Ventilation-Perfusion Scan

A combination of radionuclide ^{133}Xe ventilation scan and $^{99\text{m}}\text{Te}$ albumen macroaggregate perfusion scans can be used to qualitatively assess \dot{V}/\dot{Q} relationships where (\dot{V} is the total lung ventilation and \dot{Q} is blood flow) There is extensive clinical experience with this technique, primarily for diagnosis of pulmonary emboli.

1.3.4.2 Multiple Inert Gas Elimination Technique (MIGET)

MIGET is a technique using the pulmonary elimination of multiple inert gases of different solubilities to detect nonuniform \dot{V}/\dot{Q} ratios. Introduced by Fahri [19] for a small number of compartments, the technique was developed by Wagner into one capable of demonstrating a continuous distribution of \dot{V}/\dot{Q} ratios at rest and exercise [20,21]. The procedure involves intravenous infusion of six inert gases (sulfur hexafluoride, ethane, cyclopropane, halothane, diethylether, and acetone) dissolved in saline or 5% dextrose until a steady state is reached in 20 minutes. Arterial and mixed venous blood as well as the expired air are sampled for gas concentrations. Cardiac output is determined via a dye dilution technique and minute ventilation is measured. It has been shown [19] that the ratio of alveolar partial pressure (P_A) to mixed venous partial pressure ($P_{\bar{V}}$) can be given by :

$$\frac{P_A}{P_{\bar{V}}} = \frac{\lambda}{\lambda + \dot{V}/\dot{Q}} \quad (1.5)$$

where λ is the Ostwald solubility coefficient (which is the same as the Bunsen solubility coefficient expressed at body temperature 310K instead of 273K). A mathematical model has been developed which permits calculation of the ventilation and blood flow for each gas against the \dot{V}/\dot{Q} ratio for an arbitrary number (50) of compartments and compares this to the measured value [20]. A least squares procedure is used to fit the model to the experimentally determined distribution based on an initial assumed distribution of \dot{V}/\dot{Q} ratios among the compartments. In normal subjects, a Gaussian distribution of \dot{V}/\dot{Q} ratios around a ratio of unity with small standard deviation (0.35 and 0.44 for ventilation

and perfusion) is expected [21]. The advantage of this method is that it yields detailed analysis of ventilation-perfusion mismatch but the invasive nature of the monitoring makes routine use cumbersome.

1.3.5 Diffusing Capacities for Oxygen and CO₂

The lung diffusing capacity of oxygen (D_{LO_2}) is defined by [22] :

$$D_{LO_2} = \frac{\dot{V}_{O_2}}{P_{AO_2} - P_{cO_2}} . \quad (1.6)$$

where P_{AO_2} is the alveolar oxygen tension and P_{cO_2} is the mean oxygen tension in the red blood cell during transit through the lung capillaries. A similar diffusing capacity can be defined for CO₂. However, because the uptake of both gases is blood flow limited rather than diffusion limited [22], direct measurements of these quantities has been difficult to obtain. Lilienthal and Riley reported a method for separating the alveolar-arterial gradient for oxygen into two components, one due to ventilation-perfusion mismatch and one due to failure of equilibration of P_{O_2} between alveolar gas and capillary blood [23]. The technique involved determination of the alveolar-arterial gradient for oxygen under steady state conditions with two different inspired oxygen concentrations. This has however been criticized on the grounds that both ventilation-perfusion mismatch and D_{LO_2} change at different inspired oxygen concentrations.

The diffusing capacity for CO₂ has been measured using a mass spectrometer and ¹²C¹⁸O¹⁶O under a single breath-hold. The average in two normal subjects was 862 ml/min/mm Hg [24]. However, the measurements were difficult to perform, as the kinetics of the gas required the breath-hold to be completed in less than 3 seconds. In contrast, the diffusing capacity for CO is easier to measure and is well established.

1.4 Carbon Monoxide Lung Diffusing Capacity (D_{LCO})

One of the principal methods used in clinical medicine to measure gas exchange in the lung is the diffusing capacity of carbon monoxide or D_{LCO} [25]. This measurement has an interesting historical development which has been reviewed by Hughes and Bates [26]. A more contemporary review is given by Hughes [27]. In current practice, the single breath method is used most often. In this procedure, the patient inhales a breath of 0.3 % CO and 10% helium to vital capacity (the maximum volume that can be inhaled from normal exhalation), breath-holds for 10 seconds and exhales. The first 750 ml are discarded to avoid dead space dilution. The next litre is analysed for CO and helium concentration. The measured concentration of helium yields the factor by which the inspired gas has been diluted by mixing with alveolar gas, and allows calculation of the initial alveolar P_{CO} as well as alveolar volume. Under the assumption of an exponential decay of alveolar P_{CO} due to transfer of the CO into the lung tissue and red blood cells (RBCs), the rate constant for the decay k_{CO} can be calculated from the initial (calculated) and final (measured) alveolar CO concentration (CO₀ and CO_t respectively):

$$k_{CO} = \frac{\ln[CO_0 / CO_t]}{BHT} \quad (1.7)$$

where BHT is the breathhold time of 10 seconds [28] . The D_{LCO} is then calculated as the product of the rate constant for CO uptake (k_{CO}) and the alveolar volume (V_A) divided by the difference between barometric pressure (P_B) and the water vapour pressure at 37°C (P_{H_2O}):

$$D_{LCO} = \frac{k_{CO} \times V_A}{P_B - P_{H_2O}} \quad (1.8)$$

The diffusing capacity is expressed in units of ml/min/mmHg (traditional) or ml/min/kPa (SI), with the numerical value in the former units divided by 3 to convert to the latter. The commonly used single breath method was proposed by Ogilvie et al [29] and incorporates the original method of M. Krogh [30] with the addition of helium to the inspired mixture for determination of V_A as suggested by Fowler [26]. In the UK and Europe, the D_{LCO} is termed the T_{LCO} (transfer factor). The k_{CO} is termed the transfer coefficient for carbon monoxide and expressed as D_{LCO}/V_A or T_{LCO}/V_A . The performance of the single breath D_{LCO} has been standardized in guidelines from the American Thoracic Society [31]. The D_{LCO} is available in most pulmonary function laboratories worldwide .

Roughton and Forster showed that D_{LCO} has components due to the alveolar membrane (D_M) and the red blood cell, with the latter expressed as the product of capillary

blood volume V_C (in ml) and the specific blood transfer conductance for carbon monoxide θ_{CO} in ml CO/min/ml blood [32]. Under the assumption that the V_C and the D_{LCO} were independent of the alveolar oxygen partial pressure P_{AO_2} and that there were no concentration gradients in the capillary plasma i.e. the plasma surrounding RBCs was “well mixed”, they derived the Roughton-Forster equation :

$$\frac{1}{D_{LCO}} = \frac{1}{D_M} + \frac{1}{\theta_{CO}V_C} . \quad (1.9)$$

The value of θ_{CO} had previously been determined spectrophotometrically in vitro [33] and follows the relation [22]:

$$\frac{1}{\theta_{CO}} = 0.73 + 0.0058 \cdot P_{AO_2} . \quad (1.10)$$

Since $1/\theta_{CO}$ varies linearly with P_{AO_2} , Roughton and Forster plotted measured $1/D_{LCO}$ against $1/\theta$ at different inspired concentrations of O_2 and obtained V_C and D_M as the slope and intercept respectively. Their values of D_M (57ml/min/mmHg) and V_C (80ml) in man agree well with later measurements of 48 ml/min/mmHg and 79ml [34]. A recent refinement is the addition of nitric oxide (NO) in the single breath method [22]. For NO the corresponding θ_{NO} is large, allowing the second term in Eqn 1.9 to be neglected ; the D_{LNO} is therefore assumed equal to D_{MNO} , and since the diffusivity of NO is 1.97 times that of CO the ratio of D_{MNO}/D_{MCO} is assumed to be 1.97. Once D_{MCO} is calculated, V_C

can also be calculated, using known values of θ_{CO} . Using this method in humans Zavorsky et al measured a mean D_M of 106.7 ± 9.2 ml/min/mmHg and V_C of 116.3 ± 12.8 ml [35]. The calculated values are sensitive to the values of θ_{CO} which are measured in vitro but assumed to be the same in vivo. The importance of red cell vs alveolar membrane as rate limiting steps in the transfer of CO from gas to blood is still uncertain and values of red cell resistance as a fraction of total resistance vary from 20 to 80%, although it is more likely to be about 50% [36].

The D_{LCO} (which is in the range of 20-30 ml/min/mmHg in normal human subjects) will depend on a number of factors corresponding to the terms in the Roughton Forster equation. These have been reviewed by Hughes and Pride [28]. In normal subjects the principal variables are V_A and V_C , corresponding to the degree of lung inflation and cardiac output respectively. The k_{CO} increases with decreased V_A while D_{LCO} decreases slightly with decreased V_A . Increased cardiac output, such as in exercise, results in increased D_{LCO} . Reduction in the red cell volume (hematocrit) will reduce D_{LCO} . Body weight is also correlated with D_{LCO} in humans, and D_{LCO} scales in a log linear manner with body weight across various mammalian species [36].

In respiratory disease, the D_{LCO} may be reduced, unchanged or even increase, depending on the physiological alterations of the disease in question. It is difficult to generalize, since there is such a wide spectrum of alterations in V_A , V_C , and alveolar damage, combined with varied distribution of diseased areas within the lung. Hughes and Pride have listed alterations in the k_{CO} in various diseases [28]. Decreased k_{CO} is seen in four main groups of disease : (i). diffuse alveolar damage ; (ii). pulmonary hypertension ; (iii). intrapulmonary shunting, and (iv). obstructive lung disease. Groups (i) and (iv) are

of greater clinical importance. The physiological changes in each group correspond to quantities in the Roughton-Forster equation. The first group includes interstitial pulmonary fibrosis, including that caused by autoimmune disease, and sarcoidosis, a granulomatous lung disease, in which there is fibrosis and alveolar damage leading to barriers to gas exchange. Probable mechanisms include reduction in D_M and also V_C due to reduced pulmonary blood flow. The second group includes vasculitis (inflammation of blood vessels), pulmonary edema (accumulation of fluid in the interstitial space and alveoli) and pulmonary thromboembolism (blood clots in the pulmonary arteries). Again, various combinations of reduction in D_M and V_C are seen. The third group includes pulmonary arteriovenous malformations, in which a portion of the pulmonary blood flow is diverted back into the venous system without passing through normal lung, leading to a reduced effective V_C . The fourth group includes Chronic obstructive pulmonary disease (COPD) or emphysema in which there are areas of alveolar destruction (reduced D_M) and loss of capillaries (V_C). In addition, the measured V_A is often low in this group because of nonuniform distribution of inspired gas and incomplete mixing. In groups (i),(ii), and (iii), V_A may be low or even normal.

Corresponding to these changes in k_{CO} and V_A , the D_{LCO} is reduced in interstitial pulmonary fibrosis, sarcoidosis, pulmonary hypertension, and COPD /emphysema [25].

Although the D_{LCO} is affected by many variables, and there is some variability in the absolute values measured at different laboratories, it remains a useful tool when interpreted in the clinical context. It is simple to perform, and is most useful in detecting changes in gas exchange either with progression of disease or response to therapy. Its use in interstitial lung disease has been reviewed [37]. The D_{LCO} is a good predictor of

exercise tolerance and need for oxygen in COPD [38]. Important clinical decisions, such as lung transplantation, lung reduction surgery in emphysema, resection of lung cancer in patients with limited pulmonary reserve or commencement of immunosuppressive therapies, are in current practice based partly on the D_{LCO} [39,40].

1.5 Rat models of lung disease

1.5.1 *Stachybotrys chartarum* Spore Induced Pneumonitis

A well studied disease model of alveolar damage in rats is the pneumonitis caused by intratracheal instillation of fungal spores from *Stachybotrys chartarum*. This mold grows in water damaged building materials (“black mold”) and has been implicated in pulmonary hemorrhage in infants [41,42]. Although the association with other human disease is not unequivocally proven [43], the *Stachybotrys* spores contain a number of toxins including isosatratoxin G, a tricothecene [44]. Intranasal and intratracheal instillation of spores in mice produced severe inflammatory changes, interstitial inflammation and hemorrhagic exudate [45,46,47]. In a rat model, a single acute exposure to 9.6 million spores intratracheally caused lung inflammation and alveolar destruction with hemorrhage peaking at 24 hours post exposure [48]. Since this disease model affected both pulmonary vasculature and alveolar tissue, gas exchange is concomitantly decreased. In terms of the diseases discussed previously, this disease model corresponds to sarcoidosis or pulmonary fibrosis, with inflammation and granuloma formation, and thickening of alveolar membranes leading to reduction in D_M and V_C .

1.5.2 Other Models of Lung Inflammation in Rats

While the *Stachybotrys* spore model was chosen for the current work due to the advantages of a well defined time course of inflammation, many other rat disease models of alveolar damage have been described. Many agents when intratracheally instilled, provoke inflammatory responses in rat lung. These include the antitumour antibiotic bleomycin, which is important in cancer therapy and causes pulmonary fibrosis as a side effect [49]. Toxic concentrations of oxygen, NO₂, and ozone [50], as well as the herbicide paraquat [51], bacterial lipopolysaccharide (LPS) and ischemia reperfusion injury [52] all cause lung inflammation and oxidative damage. Silica and asbestosis when inhaled by rats lead to similar lesions as seen in the human diseases of silicosis and asbestosis i.e. fibrosis and chronic inflammation [53]. Radiation injury also causes lung inflammation in rats [54] and is important as a model of radiation pneumonitis in humans treated with radiotherapy. The aspiration of acid has also been shown to cause acute inflammation in rat lung and a rat model employing intratracheal instillation of HCl has been described [55].

1.6 Hyperpolarized ¹²⁹Xenon

Xenon is a noble gas with excellent lipid solubility. The isotope ¹²⁹Xe (hereafter referred to as ‘xenon’) is present in 26.4% abundance in natural xenon and by virtue of its spin possesses a magnetic moment permitting its use in nuclear magnetic resonance (NMR). While the low thermal magnetization of natural xenon has been used in NMR, the

discovery of “optical pumping” has permitted the production of hyperpolarized xenon with a magnetization many orders of magnitude greater, opening up the possibility of *in vivo* NMR spectroscopy and magnetic resonance (MR) imaging of xenon gas . Optical pumping uses circularly polarized light to spin polarize alkali metal vapour (usually rubidium) which then transfers polarization to xenon gas. This polarization is large, but decays exponentially with a characteristic time constant or T_1 to a low thermal equilibrium value(~ 0). Hyperpolarized xenon possesses a large chemical shift, meaning that its resonance frequency is sensitive to its chemical environment, and xenon dissolved in condensed matter can be distinguished easily from xenon in the gaseous phase. This, combined with its lipid solubility, has made xenon an ideal probe of porous media in both biological and inorganic systems. It has for example been used to investigate minerals (zeolites), porous man-made material (Porex) and the lungs of several mammalian species. There are numerous comprehensive reviews of biological and other applications of hyperpolarized xenon [56-62].

Xenon has long been viewed as a prototypical hydrophobic ligand. It is chemically non-reactive due to completely filled orbitals. However, its large polarizable electron cloud leads to xenon being extremely lipophilic, and xenon binds to specific sites on a large number of small organic molecules, lipids, and proteins. Due to long T_1 relaxation times, xenon is useful in hyperpolarized xenon spectroscopy, particularly with respect to biological systems [56]. *In vitro* investigations have included (i). investigation of xenon adsorption onto binding sites in many proteins [63,64,65,66] (ii). determination of longitudinal and transverse relaxation times in blood [65] and rat brain, kidney, liver and lung tissue homogenates [67] and (iii). development of carrier agents (saline, Intralipid,

and perfluorooctylbromine or PFOB) capable of delivering hyperpolarized xenon from blood into tissue compartments such as brain [68,69,70,71,72]. The imaging and spectroscopy of hyperpolarized xenon in rat brain after intracarotid injection has been reported [72,73].

1.6.1 Hyperpolarization of Xenon by Spin Exchange

Spin polarization of electronic states by circularly polarized light (optical pumping) was first described by Kastler [74]. Grover et al first reported efficient polarization of xenon by spin exchange with optically-pumped rubidium [75]. The transfer of polarization occurs in two steps, first from the photons to the electron spins of the rubidium, and second from the electron spins to the xenon nuclear spins. The valence electron of the rubidium is excited by the light from the $5s_{1/2}$ state to the $5p_{1/2}$ state. The wavelength corresponding to this transition (the D_1 line) is 794.8 nm. Each level is split into two sub-levels corresponding to the magnetic quantum number $m_j = +1/2$ or $-1/2$, as shown in Figure 1.3. The circularly polarized light imposes a further restriction on the permitted transition. For example, for σ^+ light (right handed polarization), only the transition from the $-1/2$ $5s_{1/2}$ sub-level to the $+1/2$ $5p_{1/2}$ sub-level conserves the angular momentum ($+\hbar$) of the photon. The populations of the two $5p_{1/2}$ excited sub-levels is equalized by collisional mixing, and both ground state sub-levels are repopulated with equal probability. A small amount of N_2 gas allows this decay to occur without the emission of a photon of the opposite handedness, say σ^- which could excite the alternate ground state sub-level. Since electrons accumulate in the non absorbing sub-level

($m_j=+1/2$), the rubidium becomes polarized to levels of almost 100% [76]. The process is shown schematically in Figure 1.3. The second stage of the process, the transfer of spin from rubidium to xenon, has been shown to be dominated by hyperfine interaction in short lived van der Waals molecules [77]. A three-body collision between a N_2 molecule, a rubidium atom and a xenon atom forms a weakly bound van der Waals molecule with a lifetime greater than 10^{-9} s, as shown in Figure 1.4. The coupling between the angular momentum of the molecule, the electron spin of the rubidium, and the nuclear spin of the xenon atom causes the latter to flip up. Only a small portion of the spin of the

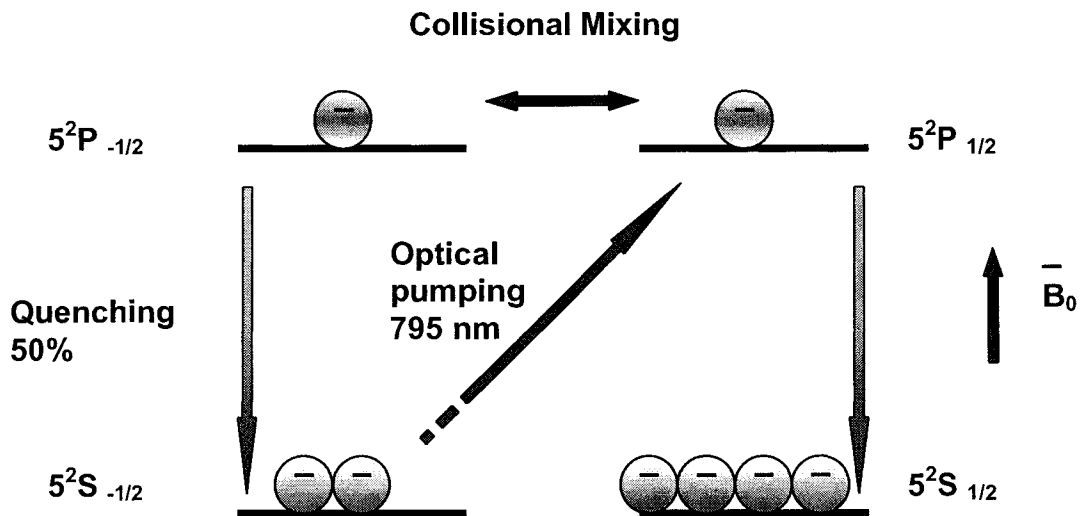


Figure 1.3
Optical pumping of rubidium electrons
by circularly polarized light. Adapted
from [73].

rubidium atom is transferred to the xenon nucleus. Because three-body collisions are rare and the coupling is weak, the spin exchange rate constant is quite low, being reported as $10^{-14} \text{ cm}^3 \text{ sec}^{-1}$ for Rb-Xe at 15 Torr N₂ pressure [77]. The hyperpolarized xenon undergoes relaxation by a number of mechanisms, including collisions with rubidium atoms and wall induced relaxation. The relaxation rates are slowed significantly in external magnetic fields of a few hundred gauss. Driehuys *et al* introduced the use of a

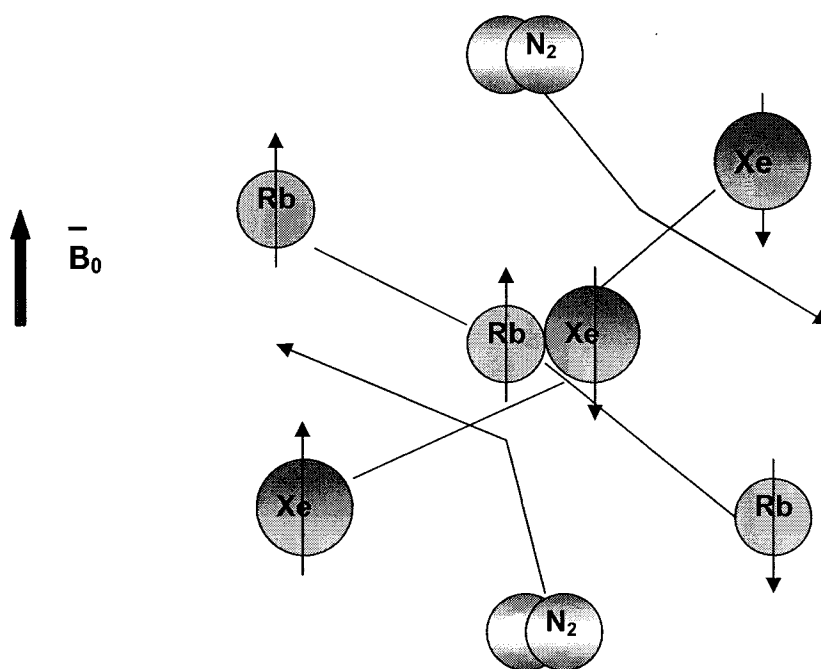


Figure 1.4
Transfer of angular momentum in a
three body collision between Rb, N₂
and ¹²⁹Xe. Adapted from [79].

mixture of 1% xenon, 1% N₂, and 98% ⁴He which broadens the D₁ line without introducing a strong spin rotation interaction, thereby increasing the absorption of laser light [78]. This is important as inexpensive laser diode arrays can be used delivering tens

of watts of power with frequency widths (1-3 nm) which are broad in comparison to the width of the atomic transition. The reaction is carried out in a glass chamber or cell containing rubidium vapour through which xenon flows. Using a cell temperature of 130-150°C, hyperpolarized xenon was accumulated cryogenically at liquid N₂ temperatures and later sublimated before use. Polarizations of 15-20% are common with this method [76].

The theoretical basis of spin exchange optical pumping of noble gas nuclei has been reviewed by Walker and Happer [79]. A number of interactions lead to relaxation of noble gas nuclei and/or alkali metal electron spins, including the spin-rotation interaction for both rubidium and noble gas nuclei, alkali metal collisions, magnetic field inhomogeneity, and wall relaxation.

Hyperpolarized xenon is generally produced in a continuous flow manner and then accumulated in the form of xenon ice prior to sublimation for use. Several reports have examined the mechanisms of relaxation in the solid phase. Between 20 and 120 K and in the presence of magnetic fields above 0.05 T, the principal mechanism of relaxation is spin-phonon scattering, and T₁ is on the order of hours. Above this temperature, the T₁ is much shorter, on the order of seconds. In the absence of a magnetic field, polarization transfer to ¹³¹Xe is an effective relaxation mechanism in natural abundance xenon [80, 81, 82]. The feasibility of prolonged storage of ¹²⁹Xe polarization has been demonstrated, implying that production and use may occur at separate sites [83].

1.6.2 Applications of Hyperpolarized Xenon *in vivo*

The most developed application of *in vivo* hyperpolarized xenon spectroscopy is to pulmonary gas exchange. Wagshul *et al* published the first *in vivo* spectra and images of mouse lungs [84]. They found the gas peak at 0 ppm to be broad and heterogeneous which was ascribed to bulk magnetic susceptibility effects. Three dissolved phase resonances at 190 ppm, 196 ppm and 198 ppm were tentatively assigned to thoracic tissues, lung parenchyma and blood respectively. Sakai *et al* observed a single gas phase resonance at 0 ppm in tracheostomized Sprague Dawley rats, and three dissolved phase resonances at 191 ppm, 199 ppm, and 213 ppm, which were attributed to plasma/adipose tissue, lung parenchyma, and red blood cells respectively [85]. Hyperpolarized ^{129}Xe spectroscopy was correlated with chemical shift imaging in one dimension in Sprague Dawley rats by Swanson *et al* who observed the *in vivo* dynamics of ^{129}Xe in rats breathing a 50:50 mixture of oxygen and xenon, and documented 1-D images of resonances in brain, thorax, and kidneys. They concurred with the previous report in regard to the identification of the blood (210 ppm) and lung tissue (199 ppm) but suggested that the resonance at 192 ppm was due to epicardial fat, as it resided exclusively in the voxels over the heart as correlated with proton imaging. Flip angles of 13 degrees permitted sufficient red blood cell magnetization to reach the brain and kidneys, where resonances at 199 ppm (tissue) were observed, while flip angles of 30 degrees reduced the RBC magnetization sufficiently to destroy the kidney and brain signal [73].

The preceding reports had not examined the spectral dynamics of the resonances identified. Ruppert *et al* addressed this issue by using frequency selective Gaussian pulses centered over the dissolved phase resonances to characterize xenon exchange dynamics on a millisecond scale in living dogs [86]. The lung parenchyma (197 ppm) and RBC (212 ppm) resonances were examined since at shorter time scales the adipose resonance did not appear. By saturating the dissolved phase resonances and allowing a variable delay time to elapse before spectra were acquired, the authors were able to characterize the recovery of magnetization in the red blood cell and lung parenchyma compartments as a function of delay time. Delay times over several ranges were explored. Over the range from 6 ms to 280 ms, and again from 70 ms to 8960 ms, this recovery was found to follow an exponential recovery. Fitting this curve to a mono-exponential recovery model, time constants of 61 ms for the tissue peak and 70 ms for the RBC peak were found [86]. In a related publication, Ruppert *et al* exploited the reduction in the relatively large gas phase signal caused by exchange with saturated dissolved phase compartments to produce images with “xenon transfer contrast”. Curves plotting the reduction in gas phase signal versus delay time also followed an exponential recovery time with a time constant of 11 ms [87]. Similar experiments in rabbits using a slightly different pulse sequence involving inversion of the dissolved phase resonances to produce reduction of the gas resonance through exchange, showed an exponential recovery with a time constant of 9.30 ms. \pm 0.02 ms [88,89]. The same authors described the method in detail and suggested that the percent depolarization of the gas phase may be used as a measure of localized lung density or surface-to-volume ratio [90].

The effect of a rat lung disease model (inflammation caused by bacterial lipopolysaccharide or LPS) on these time constants of magnetization recovery (hereafter termed transfer time or T_{tr}), was investigated by Mansson *et al* [91]. In Wistar rats, the time constants for recovery of magnetization were determined for the lung parenchyma and red blood cell resonances. Whereas the earlier references had employed a mono-exponential fit, Mansson *et al* developed a model which consisted of an exponential recovery superimposed on a linear term, by modeling the alveolar, lung tissue, and red blood cell compartments in a spherical geometry in which the lung tissue and red blood cell compartments were concentric around an alveolar air space of much larger diameter as shown in Figure 1.5. The time constants for the control animals were 29 \pm 4 ms and 25 \pm 5 ms for the lung parenchyma and red blood cell resonances respectively. For the LPS treated group the corresponding values were 40 \pm 5ms and 31 \pm 8 ms. By further refinements to their model, the authors were able to calculate a number of physiological parameters including diffusion length (made up of tissue thickness plus capillary diffusion length), perfusion, relative blood volume, and hematocrit. They found significant differences in the diffusion length but not in the relative blood volume, perfusion, or hematocrit. This suggested that hyperpolarized xenon spectroscopy could be useful in detection of medically important changes in diffusion properties in the lung which are altered by disease.

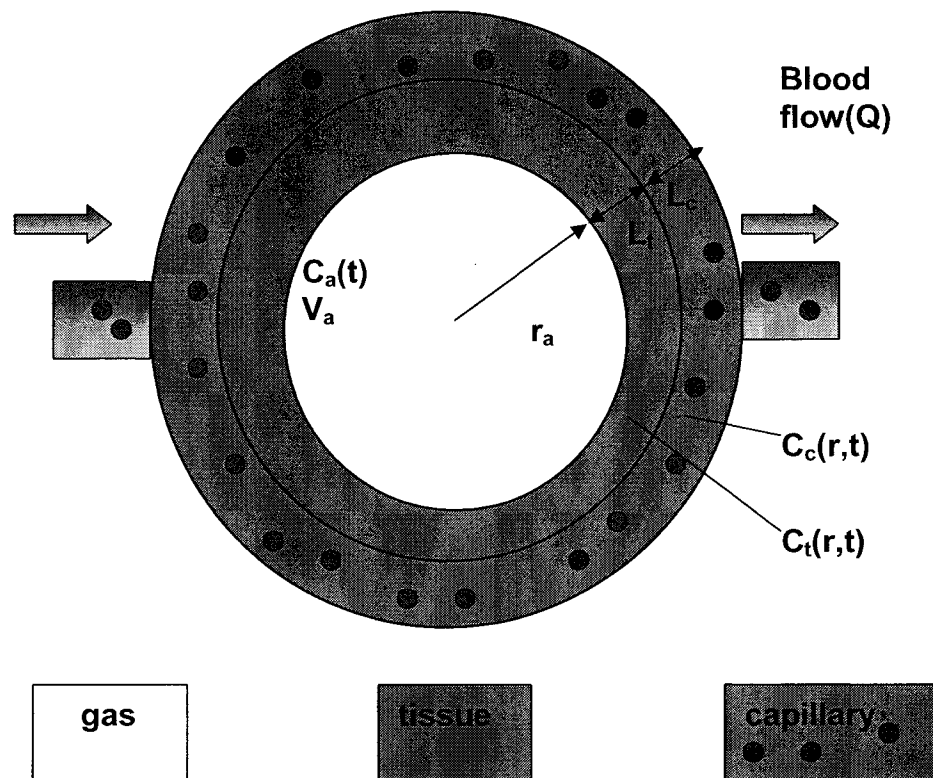


Figure 1.5

The single alveolar diffusion model.

Adapted from [91].

C_a =alveolar concentration

C_t =tissue concentration

r_a = alveolar radius L_t =tissue thickness

L_c =capillary thickness

V_a =alveolar volume

V_t =tissue volume V_c =capillary volume

1.7 Rationale for a Xenon Lung Diffusing Capacity

The current investigation was motivated by the analogy between exponential decay of CO defined by the k_{CO} and the recovery time constants (T_{tr}) obtained by dynamic hyperpolarized ^{129}Xe spectroscopy. The recovery of xenon polarization in the red blood cell and lung parenchyma compartments is paralleled by a corresponding decrease in the alveolar xenon concentration, since it is the transfer of xenon from alveolar gas to those compartments which is responsible for both processes. The inverse of the T_{tr} for the lung parenchyma and the RBC can be thought of as the equivalent of the k_{CO} insofar as these parameters quantify the transfer of gas from one compartment to another (i.e. $1/T_{tr} = K_{XeLP}$ or K_{XeRBC}). The actual transfer of xenon out of the alveolar gas has been examined by Ruppert *et al* in rabbit lungs using a series of 180/-180 frequency selective RF pulse pairs centered on the chemical shift frequency corresponding to the lung parenchyma and RBC compartments [92]. The gas phase signal was found to decay exponentially as a function of the delay time between the 180 and -180 pulses of each pair, with a time constant 9.3 ms. This decay is due to the exchange of the alveolar xenon gas with the dissolved phase, and is analogous to the exponential decay of the CO concentration in the measurement of the D_{LCO} . The recovery time constants measured separately for the red blood cell and lung parenchyma compartments is related to the inverse of the time constant representing the decrease of the xenon gas signal, although the precise relationship between the three time constants has not been established. A further motivation is the striking analogy between

CO and xenon in that diffusion of both gases is partitioned between a red blood cell compartment and a lung tissue compartment. For CO these correspond to the D_M and θV_C as discussed previously. For xenon these correspond to the red blood cell resonance at 212 ppm and the lung tissue peak at 196 ppm. The different chemical shift of xenon in the parenchyma and RBC compartments allows independent measurement of the transfer of xenon into these two compartments, suggesting that the partition of xenon diffusion capacity into these compartments could be directly measured via dynamic spectroscopy. It seems therefore reasonable (this is the central idea of the current work) to define a diffusing capacity in lung for xenon (D_{LXe}) in a similar fashion to D_{LCO} , as a product of the rate constant of diffusion and alveolar volume divided by the alveolar pressure gradient (as in Eqn 1.8). The combination of a volume measurement and a spectroscopic measurement into a diffusing capacity for xenon into the three compartments (red blood cell, lung parenchyma, and the combination of the two) is attractive for several reasons. First, it exploits the capability of hyperpolarized xenon to provide both spectroscopic and imaging measurement in an integrated study. Second, the diffusion of xenon in healthy and diseased lungs is likely to be governed by the same principles established for carbon monoxide, which have been studied for many decades. There is an extensive literature on the clinical application and standardization of D_{LCO} measurement as previously discussed, which will be useful in directing the development of the xenon diffusion study. Incorporating the lung volumes with the rate constants and defining the above diffusion capacities will provide a conceptual framework within which to connect two hitherto disparate bodies of work. Finally, the xenon measurement seems particularly sensitive to the early, rapid component of gas exchange (gas transfer times in the literature are on the

order of tens of milliseconds) whereas the D_{LCO} provides a measurement over a longer time scale of several seconds. Thirdly, it provides a new tool to investigate gas exchange abnormalities in experimental models of lung disease which may provide different information from the D_{LCO} . Finally, if the xenon diffusing capacities are useful in animal models of lung disease, the extension to human subjects would be facilitated because clinicians already have a long familiarity with the D_{LCO} .

1.8 Hypotheses

The hypotheses addressed by the current work can be stated as follows:

- (i). xenon gas transfer times (T_{tr}) for the lung parenchyma and RBC compartments can be reliably determined in normal rats and rats diseased by *Stachybotrys chartarum* spore induced pneumonitis.
- (ii). xenon diffusing capacities for lung parenchyma and RBC can be calculated reproducibly for normal and diseased rats.
- (iii). these measures of gas exchange are significantly different between the two groups.
- (iv). There is a correlation between the severity of histological changes and these measures of gas exchange in the diseased animals.

These hypotheses were tested using dynamic xenon spectroscopy to determine the gas transfer times for the lung parenchyma and red blood cell resonances in 6 normal and 6 diseased rats, concurrently with determination of alveolar volume via 3-D gradient echo imaging. Analogously to the D_{LCO} single breath measurement, the measurements were made at total lung capacity, within a single breath-hold, and hyperpolarized xenon was

administered at a controlled pressure. From the time constants, the alveolar volume, and the pressure gradient, xenon diffusing capacities were calculated for the red blood cell ($D_{LX_{eRBC}}$) and lung parenchyma ($D_{LX_{eLP}}$) compartments separately as well as being combined into an overall diffusing capacity (D_{LX_e}) and used to distinguish between control rats and rats with alveolar damage caused by intratracheal instillation of fungal spores from *Stachybotrys chartarum*. The correlation of the histological grade of lung inflammation with xenon diffusion capacity for red blood cell and lung parenchyma was also examined.

1.9 Organization of Thesis

The thesis is divided into five major sections. The background of gas exchange measurements, its clinical and scientific importance, and current experimental techniques are discussed in the Introduction. The animal model of *Stachybotrys* spore induced pneumonitis as well as current literature pertaining to hyperpolarized xenon spectroscopy *in vivo* is reviewed. A new measure of gas exchange, the xenon diffusing capacity, is defined.

The second chapter presents the theoretical basis of nuclear magnetic resonance, magnetic resonance imaging, and the xenon diffusing capacities for lung parenchyma, RBC, and whole lung.

The third chapter details the experimental methods used, including MR spectroscopy and imaging equipment, pulse sequences, production of hyperpolarized xenon, animal preparation, and data analysis.

The fourth chapter presents the results obtained. These include gas transfer curves for lung parenchyma and RBC compartments for each of 6 normal and diseased rats, the fitted gas transfer times, lung volumes, and the calculated xenon diffusing capacities. The correlation of these parameters with histology grade in the diseased animals are also shown.

The fifth chapter is a discussion of the results. Comparison is made with previous work where possible. The interpretation of the results, and their significance are discussed, as well as the prospects for future work.

2.Theory

2.1 Review of NMR Spectroscopy

2.1.1 Spin, Magnetic Moment, and Larmor Precession Frequency

Historically, NMR arose out of fundamental discoveries made by Rabi, Bloch, Hahn and others in the 1940s [93,94,95], and are reviewed in standard texts [96,97]. The development below is based on that of Nishimura [98].

Magnetic resonance is based on the existence of spin angular momentum \vec{S} which is related to the nuclear spin \vec{I} :

$$\vec{S} = \frac{h\vec{I}}{2\pi}. \quad (2.1)$$

Atoms with an odd number of either protons or neutrons or both possess a net spin angular momentum. While the proton (hydrogen nucleus) is the focus of most clinical MRI and NMR spectroscopy due to its large signal, other nuclei of interest include ^{19}F , ^{23}Na , ^{31}P , ^{13}C and the hyperpolarized gases ^3He and ^{129}Xe . The spin can be treated in a semi-classical manner as a loop of current possessing a magnetic moment $\vec{\mu}$ which is related to \vec{S} by:

$$\vec{\mu} = \gamma \vec{S} = \frac{\gamma \hbar \vec{I}}{2\pi} = \gamma \hbar \vec{I} \quad (2.2)$$

where γ is the gyromagnetic ratio which varies from one nucleus to another. The z component of spin, S_z , is quantized in units of $\hbar I$. For a proton with $I=1/2$ in a magnetic field, there are two states with $S_z = \hbar/2$ and $-\hbar/2$, corresponding to spins anti-parallel and parallel to the field. In the case of a static magnetic field (\vec{B}_0) the two states have different energies given by:

$$E = -\vec{\mu} \cdot \vec{B}_0 = -\gamma \vec{S} \cdot \vec{B}_0 \quad (2.3)$$

and the energy separation is given by:

$$\Delta E = \frac{h\gamma B_0}{2\pi} = \hbar\gamma B_0 \quad (2.4)$$

However, the energy separation is relatively small with respect to the thermal energy and the population of the spins in the two energy states is given by the Boltzmann distribution:

$$\frac{N_-}{N_+} = \exp\left(\frac{-\Delta E}{kT}\right) \quad (2.5)$$

where k is the Boltzmann constant and T is the absolute temperature in Kelvin. If a new quantity, the magnetization (\vec{M}), is defined as the vector sum of all the spins in a given volume, the magnetization at thermal equilibrium can be shown to be :

$$M_0 = \frac{N\gamma^2 \hbar^2 I_z (I_z + 1) B_0}{3kT} \quad (2.6)$$

where M is defined in units of A/m and as an example, for protons in H₂O at 310 K is given as $3.25 \times 10^{-3} B_0$ A/m and N is the number of spins per unit volume [98]. It is important to note that \vec{M} is a macroscopic vector quantity which may point in any direction, in contrast with the S_z and hence $\vec{\mu}$ which can only be parallel or antiparallel to the reference \vec{B}_0 field.

The magnetic moment is strictly speaking quantized; however a quantum mechanical treatment can be shown to be equivalent to a classical description in which magnetic moment is expressed as a vector quantity [99]. The magnetic moment undergoes a torque in a magnetic field B_0 which is given by:

$$\tau = \vec{\mu} \times \vec{B}_0. \quad (2.7)$$

Equating torque to the rate of change of spin angular momentum gives:

$$\frac{d\vec{S}}{dt} = \vec{\mu} \times \vec{B}_0 \quad (2.8)$$

and

$$\frac{d\vec{\mu}}{dt} = \vec{\mu} \times \gamma \vec{B}_0. \quad (2.9)$$

Integrating over all spins in the volume gives

$$\frac{d\vec{M}}{dt} = \vec{M} \times \gamma\vec{B}_0. \quad (2.10)$$

This is the classical equation of motion of a magnetization in a magnetic field. Thus, in a non-equilibrium situation, the magnetic moment precesses around the magnetic field vector, in an analogous fashion to a gyroscope in a gravitational field. This is in contrast to thermal equilibrium, in which \vec{M} points in the same direction as \vec{B}_0 . The angular frequency of the precession is given by the Larmor equation:

$$\omega_0 = \gamma B_0 (\text{rads/s}) \quad (2.11)$$

or alternatively

$$f = \frac{\gamma B_0}{2\pi} (\text{Hz}) \quad (2.12)$$

where, ω_0 is the Larmor frequency or angular frequency of precession around a static magnetic field \vec{B}_0 , and f is the equivalent frequency in Hz .

2.1.2. Bloch Equation, Excitation by Radio-frequency (RF) Pulses, and Rotating Frame Formalism.

The precession described above changes when a time varying magnetic field \vec{B}_1 is applied in a direction perpendicular to the main field. The \vec{B}_1 field will excite the magnetization (i.e. cause it to nutate at an angular frequency $\omega_1 = \gamma B_1$) analogously to the Larmor frequency, and the angle by which the magnetization is rotated by a B_1 pulse of duration t will equal $\gamma B_1 t$. This is termed the flip angle and is commonly set to 90° , such that the magnetization is completely rotated into the x-y plane. Figure 2.1 shows the excitation process in the frame of the laboratory and also in the rotating frame of reference. Following excitation, the magnetization vector undergoes two processes each characterized by its own time constant: it diminishes in amplitude in the x-y plane (“spin-spin relaxation”) and progressively returns to its equilibrium level in the longitudinal direction (“spin lattice relaxation”). Spin lattice relaxation occurs mainly via magnetic dipole-dipole interactions and governs the time dependence of M_z by:

$$\frac{d\vec{M}_z}{dt} = \frac{-(\vec{M}_z - \vec{M}_0)}{T_1} \quad (2.13)$$

where T_1 is the spin lattice or longitudinal relaxation time. The transverse component M_{xy} is given by:

$$\frac{d\vec{M}_{xy}}{dt} = \frac{-\vec{M}_{xy}}{T_2} \quad (2.14)$$

where T_2 is the spin-spin or transverse relaxation time. Combining the above equations with Eqn. 2.10 gives the phenomenological Bloch equation:

$$\frac{d\vec{M}}{dt} = \vec{M} \times \gamma \vec{B} - \frac{M_x \vec{i} + M_y \vec{j}}{T_2} - \frac{(M_z - M_0) \vec{k}}{T_1} \quad (2.15)$$

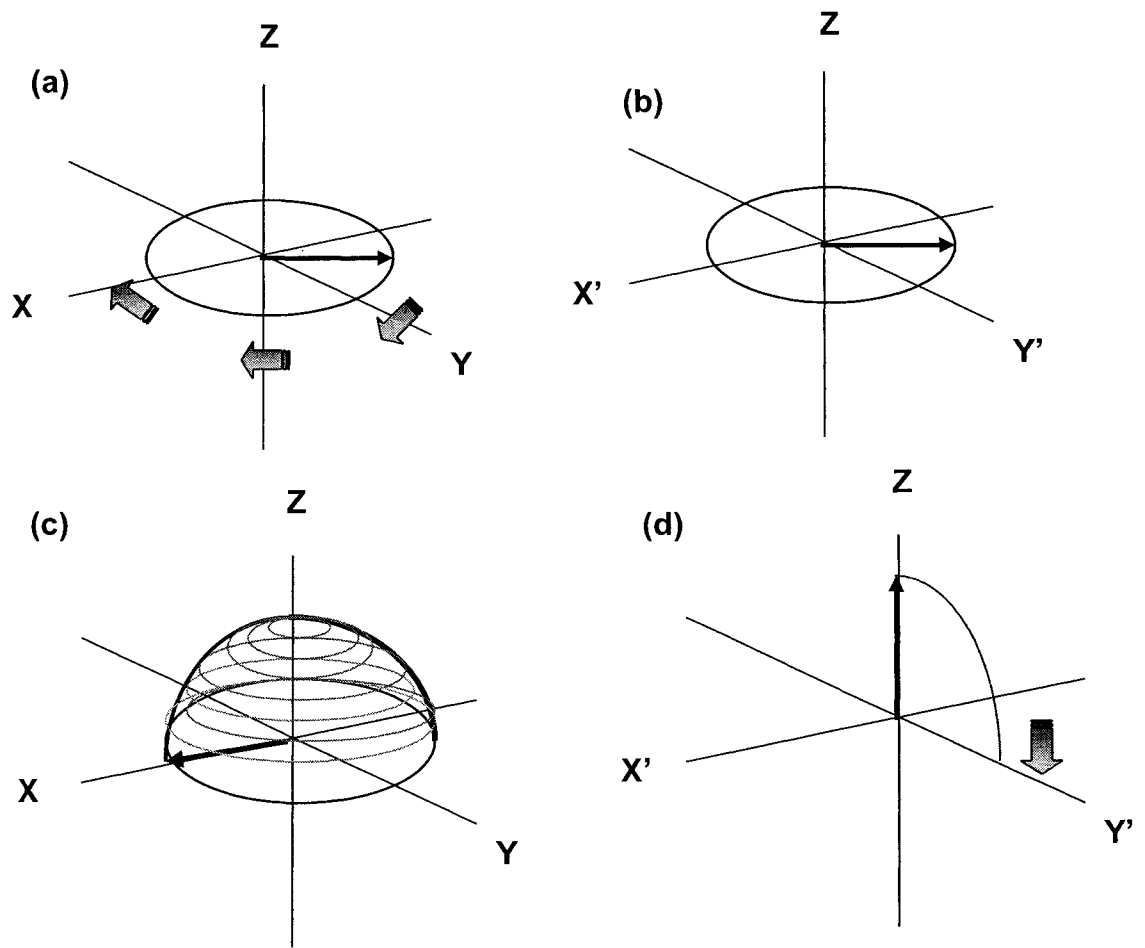


Figure 2.1 Magnetization response to RF pulse in lab and in rotating frames of reference. Relative to the laboratory frame x and y axes (a), the rotating frame x' and y' axes (b) rotate at the Larmor frequency, resulting in the spiralling precession of the magnetization in the lab frame (c) becoming a rotation about the x' axis in the rotating frame (d). Adapted from [88].

where $\vec{B} = \vec{B}_0 + \vec{B}_1$. This equation gives further insight into the nature of the excitation caused by a linearly polarized, sinusoidal magnetic field applied transversely (say along the x-axis) to the B_0 field. Qualitatively the linearly polarized field may be thought of as the sum of two circularly polarized fields rotating in opposite directions in the xy plane:

$$\vec{B}_1(t) = 2B_1(t)\cos\omega t\vec{i} \quad (2.16)$$

$$\vec{B}_1(t) = B_1(t)(\cos\omega t\vec{i} - \sin\omega t\vec{j}) + B_1(t)(\cos\omega t\vec{i} + \sin\omega t\vec{j}) \quad (2.17)$$

The second term of Eqn 2.17 describes the right-handed field which rotates counter to the spin direction, averages to zero over many rotations, and hence can be neglected. The total field then becomes:

$$\vec{B}(t) = B_1(t)(\cos\omega t\vec{i} - \sin\omega t\vec{j}) + B_0\vec{k} \quad (2.18)$$

By assuming that the B_1 field pulses occur over a time much shorter than T_1 or T_2 , the relaxation terms can be neglected and the Bloch equation becomes:

$$\frac{d\vec{M}}{dt} = \vec{M} \times \gamma [B_1(t)(\cos\omega t\vec{i} - i\sin\omega t\vec{j}) + B_0\vec{k}] \quad (2.19)$$

It has been shown that a particularly simple expression for the precession of the magnetization can be obtained by transforming to a frame of reference rotating clockwise about the z axis at the same frequency ω of the Larmor precession, the so called “rotating frame formalism” introduced by Rabi and Schwinger [100]. In general, for a frame rotating about some arbitrary vector with angular velocity $\vec{\omega}_{rot}$:

$$\frac{d\vec{M}_{rot}}{dt} = \vec{M}_{rot} \times \gamma \vec{B}_{eff} \quad (2.20)$$

$$\vec{B}_{eff} = \vec{M}_{rot} \times \gamma [\vec{B}_{rot} + \vec{\omega}_{rot} / \gamma] \quad (2.21)$$

For the particular frame mentioned above, the \vec{B}_{rot} and \vec{B}_{eff} are shown to be [88]:

$$\vec{B}_{rot} = (B_1(t), 0, B_0) \quad (2.24)$$

$$\vec{B}_{eff} = (B_1(t), 0, B_0 - \omega / \gamma) \quad (2.25)$$

Referring to Figure 2.2, \vec{B}_{eff} has a reduced z component which is zero when the \vec{B}_1 frequency ω equals the Larmor frequency ω_0 . Resonance is said to exist between the \vec{B}_1 and \vec{B}_0 fields and \vec{B}_{eff} points along the x' axis. M_{rot} precesses in the y'-z' plane. The tip angle between the magnetization vector and the z axis is given by (for constant B_1):

$$\theta = \omega_1 t \quad (2.26)$$

where t is the length of the B_1 pulse in time. A \bar{B}_1 field which causes the magnetization to tip completely into the x-y plane is referred to as an excitation or 90° pulse, while one which causes the magnetization to point along the $-z$ direction is termed an inversion or 180° pulse.

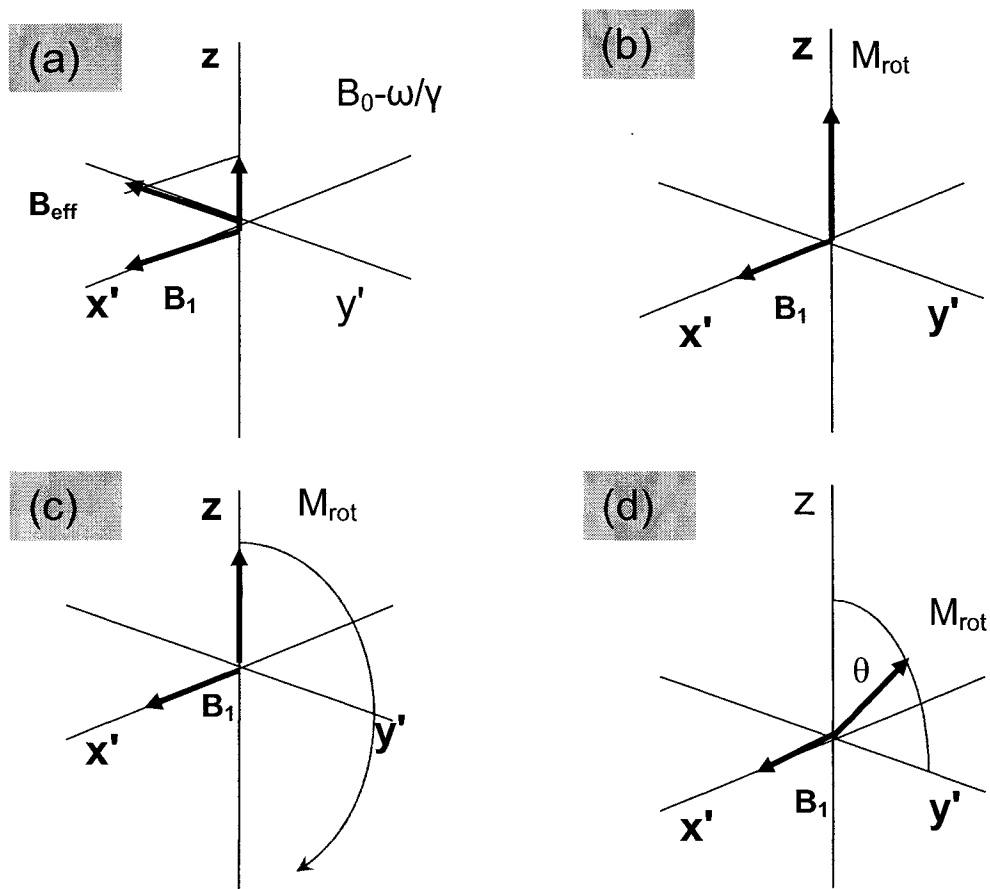


Figure 2.2 Graphical view of excitation showing :
(a) reduction of the z component of B_{eff} in the rotating frame
(b) $B_{\text{eff}} = B_1$ when $\omega = \gamma B_0$
(c) Larmor precession of the magnetization M_{rot} around B_1 by
(d) flip angle θ . Adapted from [92].

2.1.3 Free Induction Decay, NMR spectra, and the Fourier Transform

The magnetization vector, once rotated away from the z axis, possesses a component in the transverse plane which can induce an electromotive force ε in an appropriately positioned coil by Faraday's law [92]:

$$\varepsilon = -\frac{\partial\Phi}{\partial t} \quad (2.27)$$

where Φ is the rate of change of flux in the coil. Because of dephasing of the transverse magnetization by spin-spin interactions and magnetic field inhomogeneities, this electromotive force decays with a T_2^* dependence. The T_2^* (which is usually much shorter than T_2) is given by:

$$\frac{1}{T_2^*} = \frac{1}{T_2} + \frac{1}{\gamma\Delta B} \quad (2.28)$$

where ΔB is the magnetic field inhomogeneity and γ is the gyromagnetic ratio.

The time-dependent signal induced in the coil is called a free induction decay or FID.

Fourier transformation of the FID produces the NMR spectrum in the frequency domain.

The peaks of the spectrum are commonly described by a Lorentzian function, corresponding to the exponential decay of the components of the FID. Otherwise identical spins in a given system may have a variety of resonant frequencies due to chemical shift. Chemical shift refers to the change in resonant frequency caused by any variation in the chemical environment of a nuclear spin due to shielding by the surrounding electrons, which are displaced by the B_0 field. The nuclear spin therefore experiences a different field given by:

$$B' = B_0 - B_0\sigma = B_0(1 - \sigma) \quad (2.29)$$

where σ is the shielding constant. The corresponding resonant frequency is proportional to B_0 and is given by :

$$\omega' = \omega_0(1 - \sigma) \quad (2.30)$$

It is customary to express chemical shift in a way that is independent of B_0 , by defining it with respect to a reference frequency ω_R . If the resonance frequency of the spin of

interest is ω_S , the chemical shift δ is defined in parts per million (ppm) as:

$$\delta = \frac{\omega_S - \omega_R}{\omega_R} \times 10^6 \text{ ppm} \quad (2.31)$$

In proton NMR spectroscopy of a molecule, protons at different positions on the molecule yield different peaks in the NMR spectrum. In hyperpolarized xenon spectroscopy, xenon spins in different compartments, such as red blood cells, lung tissue, or adipose tissue correspond to different peaks by virtue of different frequency shifts dependent on the environment. The reference frequency for proton NMR spectroscopy is usually taken to be that of protons in tetramethylsilane (TMS), and by convention the frequency decreases from left to right [98]. In hyperpolarized xenon spectroscopy, the reference frequency is that of xenon gas, and the frequency also decreases from left to right.

2.1.4. Frequency Selective RF Pulses and Magnetization Transfer

Magnetization transfer refers to the application of a pulse which selectively suppresses signal from spins which exchange with or reside in macromolecules [99]. An example of this would be proton spins in fat or the xenon spins in lung parenchyma or RBCs. Such a

pulse must be frequency selective, meaning that only a limited range of frequencies are excited. A RF pulse represented by a rectangular function of width $2a$ has a Fourier transform which is a sinc function with zeros at $1/a$ [101]. Any change in the duration of the rectangular RF pulse will result in an opposite change in the location of the zero or “null” in the frequency domain, and the null can be made to fall at any desired frequency. For example, xenon spins in the lung parenchyma or RBC are approximately 200 ppm or 4400Hz from the resonant frequency of the xenon gas spins. A rectangular RF pulse of duration $1/4400 \text{ Hz} = 225 \mu\text{s}$ will therefore have a null at the resonant frequency of the gas spins (assuming that the carrier frequency is centred at the resonant frequency of the lung parenchyma and RBC spins. Such a pulse would be frequency selective for the latter spins while minimally affecting the gas spins. A graphic representation of this is shown in Figure 2.3.

2.2 Magnetic Resonance Imaging

2.2.1 General MR Imaging Principles

Conventional proton MRI is based on the idea of encoding spatial position of elements of a spin density distribution $\rho(x,y,z)$ by connecting the frequency and or phase of the spin precession to its position [102]. Both frequency and phase encoding are implemented by means of magnetic field gradients (G_x , G_y and G_z) which are superimposed on the main

field \bar{B}_0 . Following the derivation in Haacke et al [99] and considering the 1-D case for example in the z direction, the z component of the field is:

$$B_z(z,t) = B_0 + zG_z(t). \quad (2.32)$$

The gradient $G_z(t)$ is a gradient pulse given by :

$$G_z \equiv \partial B_z / \partial z \quad (2.33)$$

and is usually constant for a given image acquisition. The resonant angular frequency of a spin subject to $G(t) = G_z(t)$ then has a dependence on position along the z direction:

$$\omega_G(z,t) = \omega_0 + \gamma z G(t). \quad (2.34)$$

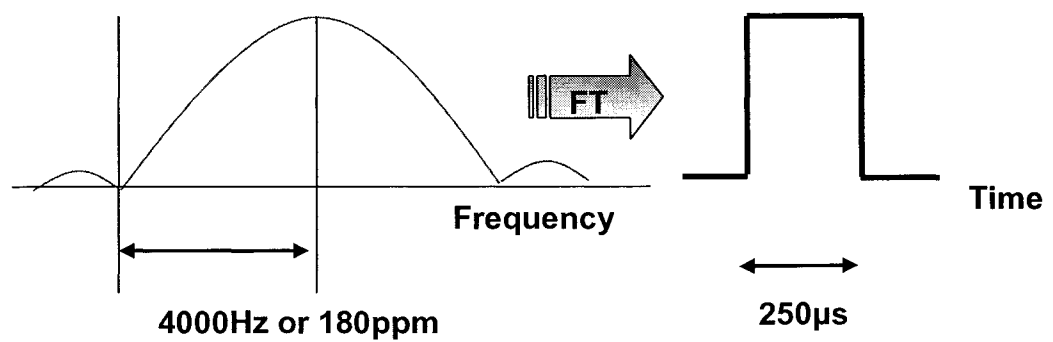
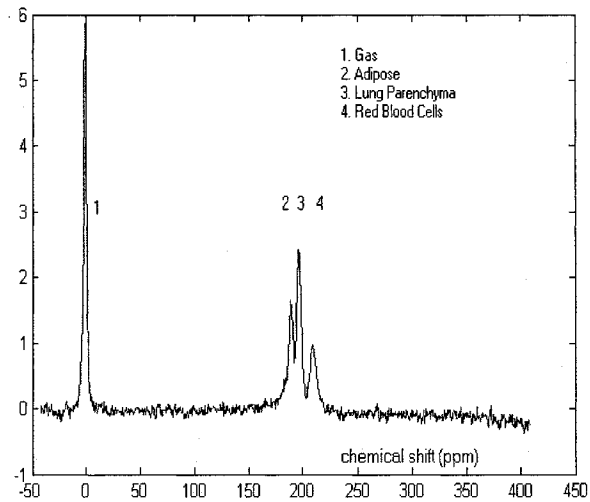


Figure 2.3 Frequency selective pulse in time and frequency domain showing maximal effect on lung parenchyma and RBC peaks and minimal effect on gas peak.

Furthermore, the accumulated phase as a function of time and z coordinate is given by :

$$\phi_G(z,t) = -\int_0^t dt' \omega_G(z,t') = -\gamma z \int_0^t dt' G(t') \quad (2.35)$$

where the limits of integration are the times at which the gradient begins (time=0) and ends (time = t). The resulting signal is then given by the 1-D imaging equation:

$$s(t) = \int dz \rho(z) e^{i\phi_G(z,t)} \quad (2.36)$$

Combining Eqns 2.35 and 2.36 the signal can be represented as a function of the spatial frequency k :

$$s(k) = \int dz \rho(z) e^{-i2\pi k(t)z} \quad (2.37)$$

where $k(t)$ is given as the integral below with limits of integration as in Eqn. 2.35 :

$$k(t) = \frac{\gamma}{2\pi} \int_0^t dt' G(t') \quad (2.38)$$

The signal is therefore the Fourier transform of the spin density of the object, and hence by using the inverse Fourier transform it is possible to reconstruct the spin distribution :

$$\rho(z) = \int dk s(k) e^{+i2\pi kz} \quad (2.39)$$

The imaging equation (Eqn 2.37) can be generalized to 3-D and to arbitrary gradient pulses in the form :

$$s(k_x, k_y, k_z) = \iiint dx dy dz \rho(x, y, z) e^{-i2\pi(k_x x + k_y y + k_z z)} \quad (2.40)$$

The time dependent components of \vec{k} are defined in a fashion similar to Eqn 2.38 above :

$$k_x(t) = \frac{\gamma}{2\pi} \int_0^t G_x(t') dt' \quad (2.41)$$

$$k_y(t) = \frac{\gamma}{2\pi} \int_0^t G_y(t') dt' \quad (2.42)$$

$$k_z(t) = \frac{\gamma}{2\pi} \int_0^t G_z(t') dt' \quad (2.43)$$

2.2.2. Pulse Sequences for Imaging

There are two broad classes of imaging pulse sequences : spin echo and gradient echo. Spin echo sequences use a 180 °pulse (following an initial 90° excitation pulse) to refocus spin isochromats and generate a spin echo, a phenomenon first described by Hahn [95]. These require an equilibrium magnetization which recovers between pulses, and require relatively long times since the regeneration of the equilibrium magnetization is dependent on T₁. While they could be used for hyperpolarized gas imaging, practical difficulties in producing perfect 180° pulses limit their use. Gradient echo pulse sequences use a flip angle which does not convert all the magnetization to transverse magnetization, and are therefore not dependent on recovery of the equilibrium magnetization. Consequently they are faster than spin echo sequences. For reasons discussed later, gradient echo sequences are advantageous for hyperpolarized xenon MR imaging. Gradient echo sequences can be used to acquire images in 2-D slices or 3-D volumes.

A conventional 2-D gradient echo sequence is shown in Figure 2.4. The radiofrequency or RF pulse excites the slice defined by the slice selection gradient G_{zss}.

The negative or dephasing lobe of the Gz gradient returns the spins in the excited slice to zero phase. Subsequently, the phase encoding gradient (by convention taken to be along the Y-axis) introduces a gradient for a fixed time τ_{PE} . At each repetition of the cycle, a different value of k_y is encoded corresponding to $\gamma G_{PE} \tau_{PE} / 2\pi$. The readout gradient G_R is conventionally applied along the x axis and is also called the frequency encoding gradient. The initial negative lobe induces a phase distribution with a negative spatial frequency k_x , and as the positive lobe following causes a progressive rephasing of the spins, the k_x value returns to zero and then increases. The ADC (analog to digital converter) samples data at intervals Δt which determine the bandwidth ($1/\Delta t$) and hence the field of view in the x-direction (FOV_x) as defined by :

$$FOV_x = \frac{1}{\Delta k_x} = \frac{1}{\frac{\gamma}{2\pi} G_{xR} \Delta t} . \quad (2.44)$$

Similarly, the field of view in the phase encode direction(y or z) is given by :

$$FOV_y = \frac{1}{\Delta k_y} = \frac{1}{\frac{\gamma}{2\pi} \Delta G_{PE} \tau_{PE}} . \quad (2.45)$$

The extent of k space sampled determines the spatial resolution($\Delta_x, \Delta_y, \Delta_z$) along each axis such that the larger the k space extent the smaller the resolution. For the frequency encode direction, Nishimura gives the expression $k_{\max} = \gamma G_{xR} \tau_x / 4\pi$ [98] and so:

$$\Delta_x \approx \frac{1}{2k_{x \max}} = \frac{1}{\frac{\gamma}{2\pi} G_{xR} \tau_x}. \quad (2.46)$$

For the phase encode direction , $k_{\max} = G_{PE \max} \tau_{PE}$ and so :

$$\Delta_y \approx \frac{1}{2k_{y \max}} = \frac{1}{\frac{\gamma}{2\pi} 2G_{PE \max} \tau_{PE}}. \quad (2.47)$$

The k space trajectory corresponding to the pulse sequence in Figure 2.4 is shown in Figure 2.5. The particular order of acquisition is called sequential ordering or sequential acquisition [99].

The extension of a 2-D sequence to a 3-D sequence requires the addition of a phase encode step along the slice select or z-axis, as shown in figure 2.6. Each RF pulse excites a volume called a slab, and each is followed by a different phase encoding gradient. The advantages of 3-D volumetric imaging include better control over the

thickness of the slices, which can be made thinner than in the 2-D multislice case. Secondly, the adjacent slices are truly contiguous with no slice gap as in the 2-D multislice case. Thirdly, the duration of each pulse can be shortened because the slab is thicker, and the echo time (TE) can also be shortened. The principal disadvantage of 3-D volumetric imaging is the increased acquisition time. The order in which the various spatial frequencies are acquired traces a path in k-space called the trajectory. The most common trajectory used is called the 3-D Fourier transform (3-DFT) and consists of lines parallel to the k_x axis. This particular acquisition scheme provides easy reconstruction via a 3-D FFT or Fast Fourier transform, accounting for its popularity [98].

2.2.3 Hyperpolarized Xenon MRI

Imaging with hyperpolarized noble gases requires a different approach from proton MR imaging due to the non-renewable nature of the magnetization. The signal strength S is given by [103] :

$$S = \frac{N|\gamma|\hbar\omega_0 P_N}{2} \quad (2.48)$$

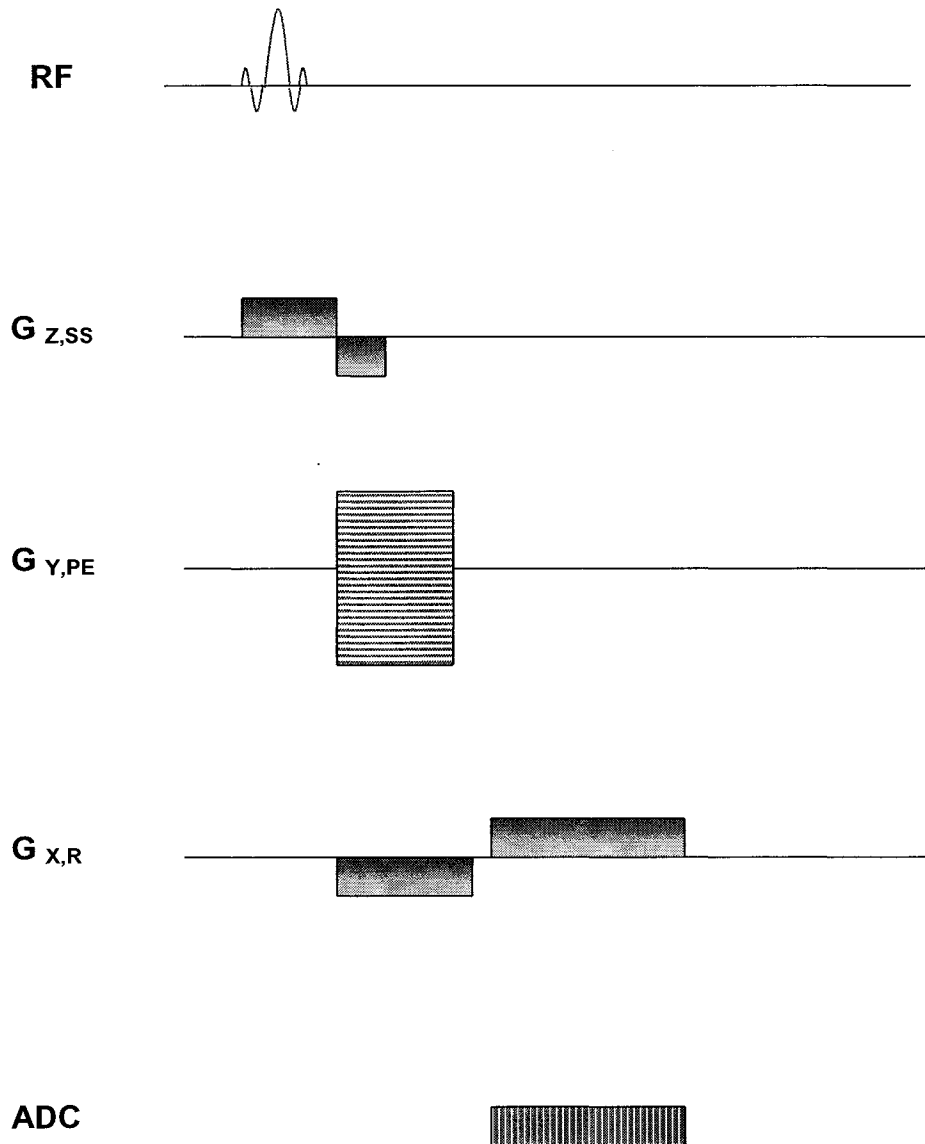


Figure 2.4 Gradient echo pulse sequence adapted from [93].

$G_{z,SS}$: slice select gradient

$G_{y,PE}$: phase encode gradient

$G_{x,R}$: Read gradient

ADC: analog to digital converter

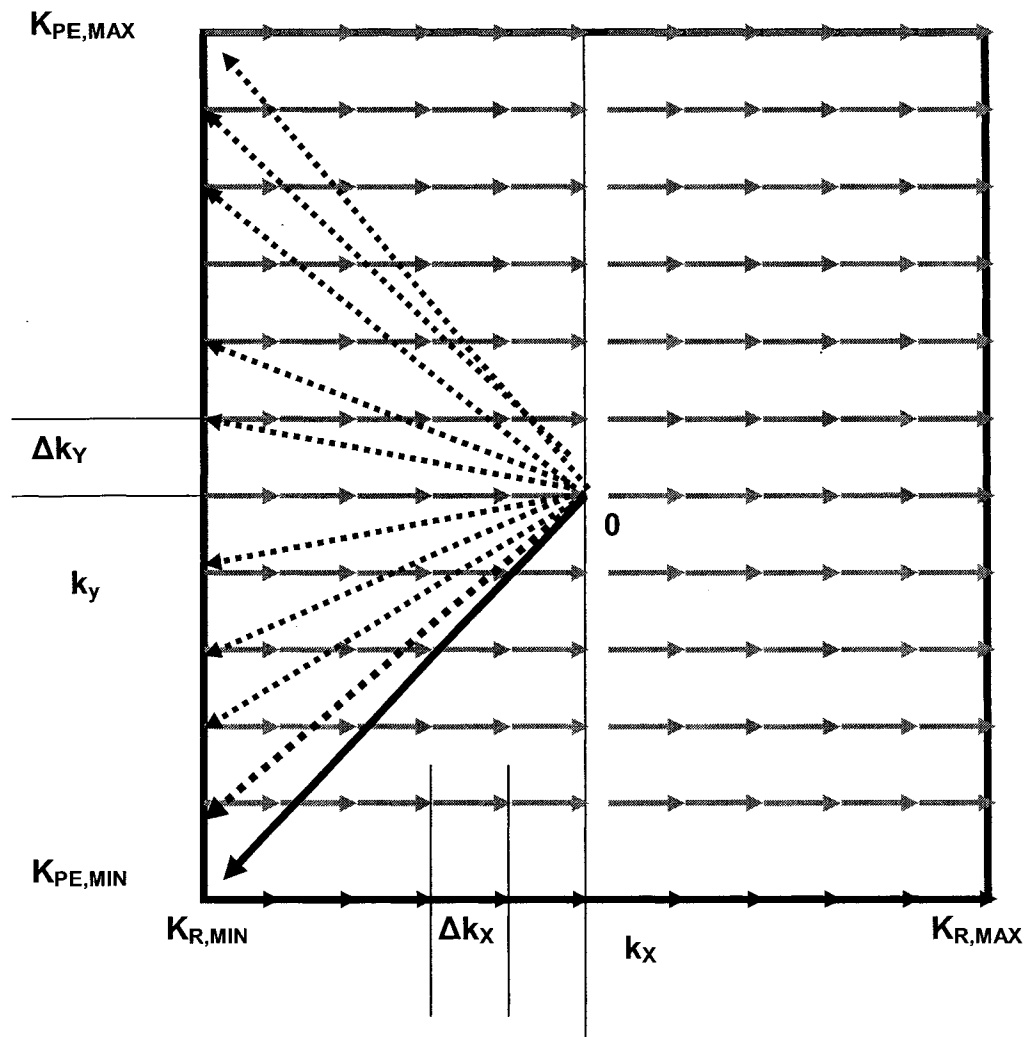


Figure 2.5 k-space trajectory for gradient echo pulse sequence of Figure 2.4. A diagonal trajectory results as k_x and k_y are changed simultaneously (long bold arrow) after which the read gradient steps through a complete set of k_x values leaving k_y constant (short bold arrows). A new cycle involves returning to a new k_y value (long dashed arrows). K_R and K_{PE} are the k space coordinates governed by the read gradient and phase encoding gradient lobes respectively. Adapted from [99].

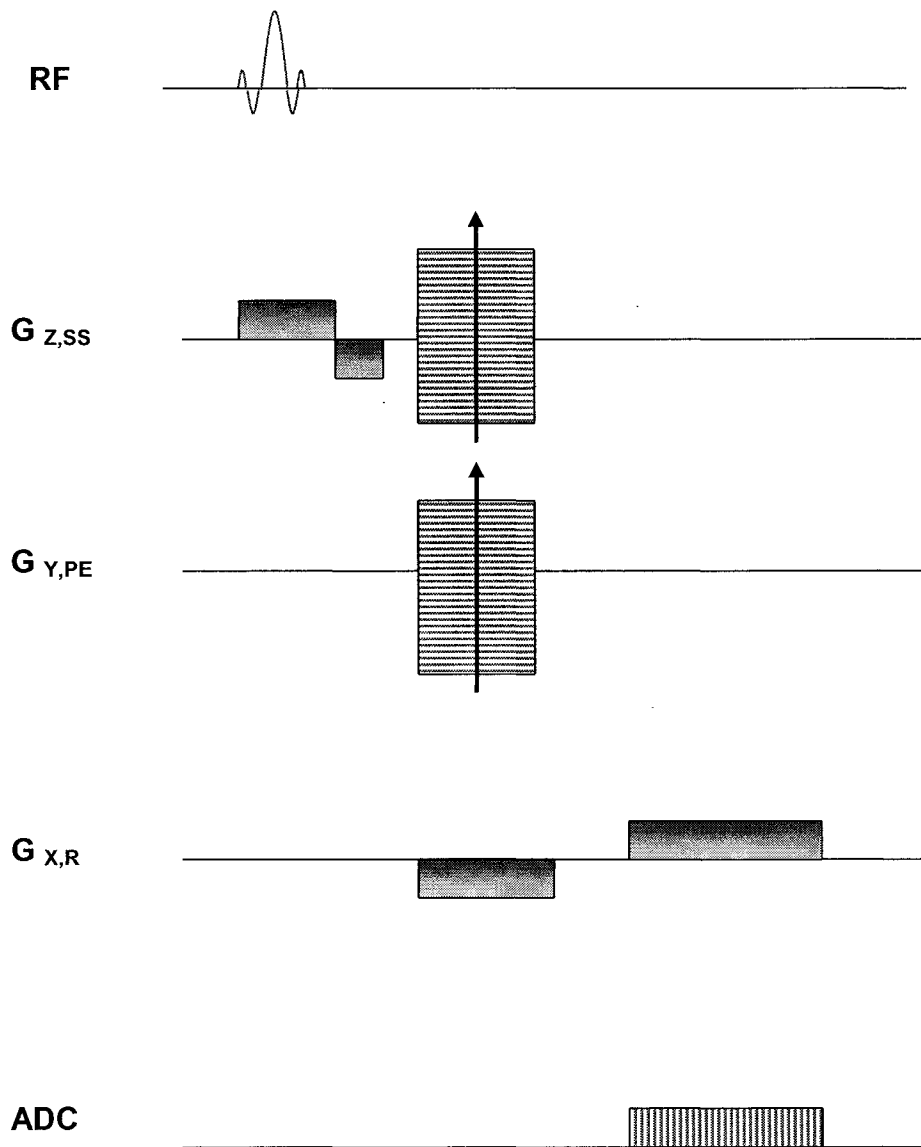


Figure 2.6 3-D FT pulse sequence in which the y and z directions are phase encoded. Figure legends as in Figure 2.4. Adapted from [99].

(where N is the number of spins and P_N is the polarization fraction) in contrast to proton imaging where :

$$S = \frac{N|\gamma|\hbar^2\omega_0^2}{4kT} \quad (2.49)$$

Zhao et al reviewed the use of gradient echo techniques in a glass cell containing hyperpolarized xenon [104]. One consequence of using a constant flip angle α during an inspiratory breath-hold is that the remaining magnetization after n excitations is not renewed during the TR interval and is given by :

$$M_{z,n} = M_z(0) \cos^n \alpha . \quad (2.50)$$

If multiple excitations of constant α are used, the signal from the n th excitation is given by [105] :

$$S(n) = M_z(0) \exp[-(n+1)TR/T_1] \cos^{n-1} \alpha \sin \alpha . \quad (2.51)$$

This scheme leads to a progressive reduction in the magnitude of the signal from one pulse to the next, resulting in artefactual reduction in signal from one line of k-space to another. A variable flip angle scheme suggested by Zhao [104] and earlier by Sobering [106] has been suggested to keep the magnitude of the transverse magnetization constant by employing , for the nth excitation of a train of N, a flip angle given by [104] :

$$\alpha_n = \tan^{-1} \left(\frac{e^{-\frac{(N-n)TR}{T_1}}}{\sqrt{N-n}} \right). \quad (2.52)$$

Since T_1 in hyperpolarized ^{129}Xe imaging is on the order of $10^4 \times TR$, the above expression reduces to:

$$\alpha_n \approx \tan^{-1} \left(\frac{1}{\sqrt{N-n}} \right). \quad (2.53)$$

By assuming that the thermal magnetization is negligible, and that all residual transverse magnetization is destroyed between excitations (e.g. by spoiler gradients), Zhao et al [104] calculated the transverse magnetization after the nth pulse to be:

$$S(n) = M_z(0) \exp[-(n+1)TR/T_1] \sin \alpha_n \prod_{j=1}^{n-1} \cos \alpha_j. \quad (2.54)$$

They further calculated that in order for the transverse magnetization to remain constant at its initial value $S_1=M_z(0)\sin \alpha_1$, the nth flip angle must be given by :

$$\alpha_n = \sin^{-1} \left(\frac{\exp[(n-1)TR/T_1] \sin \alpha_1}{\prod_{j=1}^{n-1} \cos \alpha_j} \right). \quad (2.55)$$

In general, the number of excitations that can be used is limited by the initial flip angle ; when $\alpha_n = \pi/2$, all available magnetization is used up. In a later publication, Zhao and Albert explored other pulse sequences and demonstrated images of glass cells of hyperpolarized xenon obtained with echo planar imaging (EPI) as well as spin echo based sequences such as rapid acquisition with relaxation enhancement (RARE) and gradient and spin echo (GRASE) [107].

2.3 Derivation of Xenon Diffusing Capacity for Red Blood Cells and Lung Parenchyma

It is assumed that diffusion occurs passively along a concentration gradient and follows Fick's law, whereby the net gas flux is given by:

$$F_{gas} = A(C_A - C_c). \quad (2.56)$$

Here F_{gas} is the flux of gas in ml/min/mm Hg, A is the diffusional conductance of the alveolar membrane, and C_A and C_C are the concentrations of the gas in the alveolar air and capillary blood respectively. The conductance itself depends on a number of factors. First, it is directly proportional to the surface area of the capillary-alveolar surface area. Second, it is proportional to the solubility of the gas in the water of the alveolar wall. Third, it is inversely proportional to the thickness of the alveolar membrane. Fourth, it is inversely proportional to the square root of the molecular weight of the gas. Fifth, it is dependent on the diffusion properties of the alveolar-capillary membrane itself, which may be altered by disease. Finally, for gases which undergo chemical reaction with hemoglobin (CO , O_2) or with other constituents of blood (CO_2), a factor must be included for the rate constant of those reactions [102].

There are many experimental measures of gas exchange available. However the principal measure of gas exchange in routine use in clinical medicine is the diffusing capacity of carbon monoxide or D_{LCO} . The test is done by having a subject breathe gas with a small concentration (0.3%) of carbon monoxide and helium as previously described in the Introduction. The purpose of the following section is to define a diffusing capacity for xenon into red blood cell and lung parenchyma compartments separately, using the currently accepted definition of D_{LCO} as a guide. The key idea is that D_{LCO} is defined as the product of a rate constant for the exponential removal of CO from alveolar gas multiplied by the total alveolar volume and divided by the atmospheric-alveolar pressure difference, as described by Eqn 1.8. In order to construct the analogous diffusing capacity for xenon, the equivalent quantities must be measured. Since alveolar volume can be measured by hyperpolarized xenon MR imaging, and the pressure of administered xenon

gas is known, xenon diffusion capacity can be defined separately for each compartment in an identical fashion as for carbon monoxide (D_{LXeLP} for lung parenchyma and D_{LXeRBC} for the red blood cells) if the equivalent of k_{CO} for xenon (K_{Xe}) is known. To obtain K_{Xe} , it is necessary to measure the decline in xenon magnetization as a function of time and extract a rate constant for the exponential decline. This can be done [108] but has the disadvantage of combining the losses due to uptake into the red blood cell and lung parenchyma compartments. In order to preserve the differentiation between the two compartments, it is desirable to define two new rate constants K_{XeRBC} and K_{XeLP} as follows:

$$K_{XeRBC} = \frac{1}{T_{trRBC}} \quad (2.57)$$

$$K_{XeLP} = \frac{1}{T_{trLP}} \quad (2.58)$$

where T_{trLP} and T_{trRBC} are the recovery time constants for the red blood cell and lung parenchyma compartments as defined below. Mansson et al [91] solved the 1-D diffusion equation for the single alveolar diffusion model with boundary conditions appropriate for their method of dynamic spectroscopy (which incorporated 90° pulses to saturate the

dissolved phase compartments followed by spectral acquisition at a variable delay time) and obtained the following expression:

$$S(\tau) = S_0 \left(1 - e^{-\frac{\tau}{T_{tr}}} \right) + S_1 \tau \quad (2.59)$$

Where S is magnetization, S_0 and S_1 are fit parameters, and T_{tr} is the gas transfer time (equivalent to τ_1 in the notation of Mansson et al and also being the time constant describing the exponential recovery of magnetization as a function of delay time). The T_{tr} for each compartment (T_{trLP} or T_{trRBC}) is obtained by fitting experimental data to equation 2.59. The assumption made in defining K_{XeRBC} and K_{XeLP} as above is that the time course of magnetization recovery in the red blood cells or lung parenchyma is the inverse of the magnetization loss in the alveolar gas compartment due to exchange with the corresponding dissolved phase compartment. This would seem a reasonable assumption given that there are no other compartments seen using hyperpolarized xenon lung spectroscopy, except for the adipose tissue which is negligible in the time scale of interest as it appears only in spectra with a time delay of approximately 5s. It is then possible to define, in analogy with Equation 1.8:

$$D_{LXeRBC} = \frac{K_{XeRBC} V_A}{P_B - P_{H_2O}} \quad (2.60)$$

$$D_{LXeLP} = \frac{K_{XeLP} V_A}{P_B - P_{H_2O}}. \quad (2.61)$$

These quantities are not corrected for STPD and are therefore not formally equivalent to the D_{LCO} but they incorporate the same physiological factors. Then, by analogy with the Roughton-Forster equation for CO (Equation 1.9) a similar expression for the total xenon diffusion capacity or D_{LXe} can be written:

$$\frac{1}{D_{LXe}} = \frac{1}{D_{LXeLP}} + \frac{1}{D_{LXeRBC}}. \quad (2.62)$$

3. Methods

3.1 MR Imaging Equipment

All experiments were performed in a 1.89 T horizontal bore cryomagnet (Magnex, Abingdon, UK) controlled by a MR5000 console and software (MRRS, Surrey, UK). A quadrature bird cage coil (12 cm i.d. 12.5 cm L) tuned to the xenon frequency (22.18 MHz) was used for imaging and spectroscopy (Morris Instruments, Ottawa ON).

3.2 Pulse Sequences

Xenon MR imaging of rat lungs and calculation of lung volumes was performed as described by White [109, 110]. A variable flip angle 3D gradient echo pulse sequence was used at a resolution of 64X16X16 (TE = 4ms, TR = 16 ms). The variable flip angles were calculated according to Equation 2.53. The pulse sequence development and volume imaging were done by Steven White, Carleton University as part of a M.Sc. thesis [109].

The spectroscopy pulse sequence is shown in Figure 3.1. The pulse sequence consisted of a series of 2 pulse band selective pulse separated by a delay time τ , and was written by Dr. Albert Cross, Carleton University. Each pair of pulses consisted of 250 μ s RF pulses with a carrier frequency placed near the lung parenchyma. As discussed in

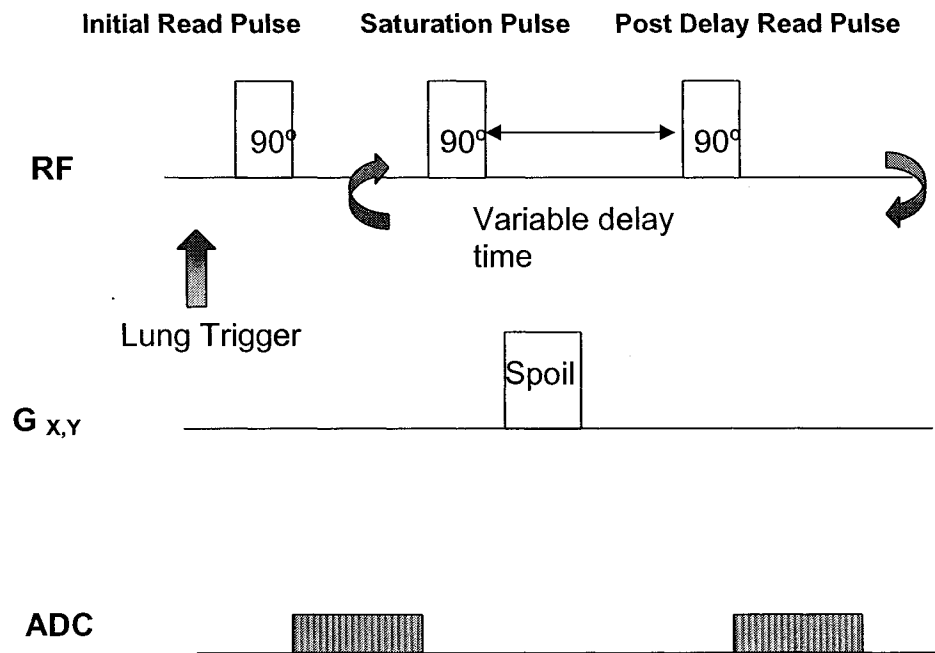


Figure 3.1.

Spectroscopy pulse sequence. Pulses between the curved arrows are repeated for each delay time. The initial read pulse acquires the first spectrum of the series, which is used for normalization but does not correspond to a delay time. Subsequent pairs of pulses acquire spectra corresponding to the separation between the saturation and read pulses. This variable delay time ranged from 1ms to 1000 ms.

Chapter 2, these pulses would result in spins in the lung parenchyma and RBC compartments experiencing a 90° flip angle whereas the spins in the gas phase would experience a very low flip angle. The bandwidth and amplitude of the pulses were adjusted such that the dissolved xenon experienced approximately a 90° pulse while the gas resonance was near the minimum of the power spectrum of the RF pulses and had been previously shown to experience a low ($< 1^\circ$) tip angle pulse [111]. Gradients were used after the first pulse of each pair to dephase the magnetization in the dissolved phase compartments. This avoided unwanted coherence between residual magnetization and subsequent excitations. After the variable delay time τ , the second pulse of the pair was followed by data acquisition. Thus one spectrum was acquired per pulse pair, and 13 pulse pairs were applied per breathhold. The very first pulse of the sequence was not paired as it was used to acquire a spectrum which would be used to normalize the lung parenchyma and RBC peaks of the succeeding pulse pair. The τ values were, in sequence, 1ms, 3 ms, 7 ms, 25 ms, 40 ms, 75 ms, 500 ms, 1000ms, 200ms, 50 ms, 35 ms, and 20 ms. This sequence of τ values was chosen in order to distribute the data points in a logarithmic fashion, with more samples in areas of the curve having greater rate of change. Furthermore, as the gas peak was undergoing decay to thermal equilibrium with a T_1 of 9.0 ± 2.8 s [111], very small τ values were placed earlier and large ones later to ensure adequate SNR. The spectra contained 2048 points acquired with a spectral width of 10 kHz.

3.3 Imaging Procedure

Hyperpolarized xenon was accumulated as xenon ice in a trap at liquid nitrogen temperatures. A five minute accumulation period was used for each xenon breath as this was established in pilot experiments as the optimal collecting time to obtain maximal lung expansion and signal-to-noise ratio [111]. Since the flow rate was 3-4 ml/min of xenon, a 5 minute accumulation yielded 15-20 cc of xenon which was sufficient to maximally expand the rat lung. After accumulation, the ice was thawed in a water bath and administered as a bolus to the experimental animal via a three way connector attached to a tracheostomy (16G) catheter. Care was taken to switch the three way valve from ventilator to xenon administration system as close to end expiration as possible, to minimize gas trapping in the lung. An inline pressure release valve situated proximal to the animal was set to 100 mbar above atmospheric pressure to avoid barotrauma and ensure a constant pressure breath-hold. This valve was noted to release consistently at each lung inflation, indicating that constant pressure breaths were being achieved. Initiation of pulse sequences for imaging or spectroscopy was gated to the maximal expansion of the rib cage as measured by a pressure transducer connected to an oscilloscope. The experimental set up is shown in Figure 3.2.

3.4 Production of Hyperpolarized Xenon

A custom made polarizer following the design of Moudrakovski et al [112] modified according to Cross et al [111] was pressurized to 550 kPa using a mixture of 1% natural abundance (26.4%) Xenon, 10% N₂ and 89 % He. The polarizer contained two chambers, shown in Figure 3.2. Prior to entering the polarizer, the gas was passed through an oxygen trap (Chromatographic Research Supplies, Louisville KY) and a water trap (Labclear, Oakland CA) in order to remove these impurities which could cause T₁ relaxation and/or oxidation of the rubidium. The gas then entered the first chamber where it mixed with rubidium vaporized by a heating coil controlled by a temperature controller (Barnant, Barrington IL). Subsequently the gas flowed into the second chamber (optical cell) where spin polarization of the rubidium vapour by circularly polarized laser light took place. Xenon was concurrently polarized by spin exchange with Rb vapour in the same chamber. The light source was a 60W 795nm diode laser array (Coherent, Santa Clara CA). The flow rate was regulated using a needle valve (Swagelock, Willoughby OH) downstream from the optical cell. The flow rate was monitored using an inline flowmeter (Fathom Technologies, Round Rock TX) and maintained at approximately 0.32 L/min. The amount of xenon produced was therefore 3-4 ml/min. The degree of polarization in the optical cell was monitored using a spectrophotometer (Ocean Optics, Dunedin FL). The polarization varied from 6 to 15 %. The polarization was determined by applying a series of 90° pulses to the flowing hyperpolarized xenon in a 1 cm solenoidal coil and comparing the signal obtained with that from a sealed thermal sample containing 505kPa of ¹²⁹Xe and 152 kPa of O₂.

The signal of each sample was normalized by the concentration of ^{129}Xe in the sample.

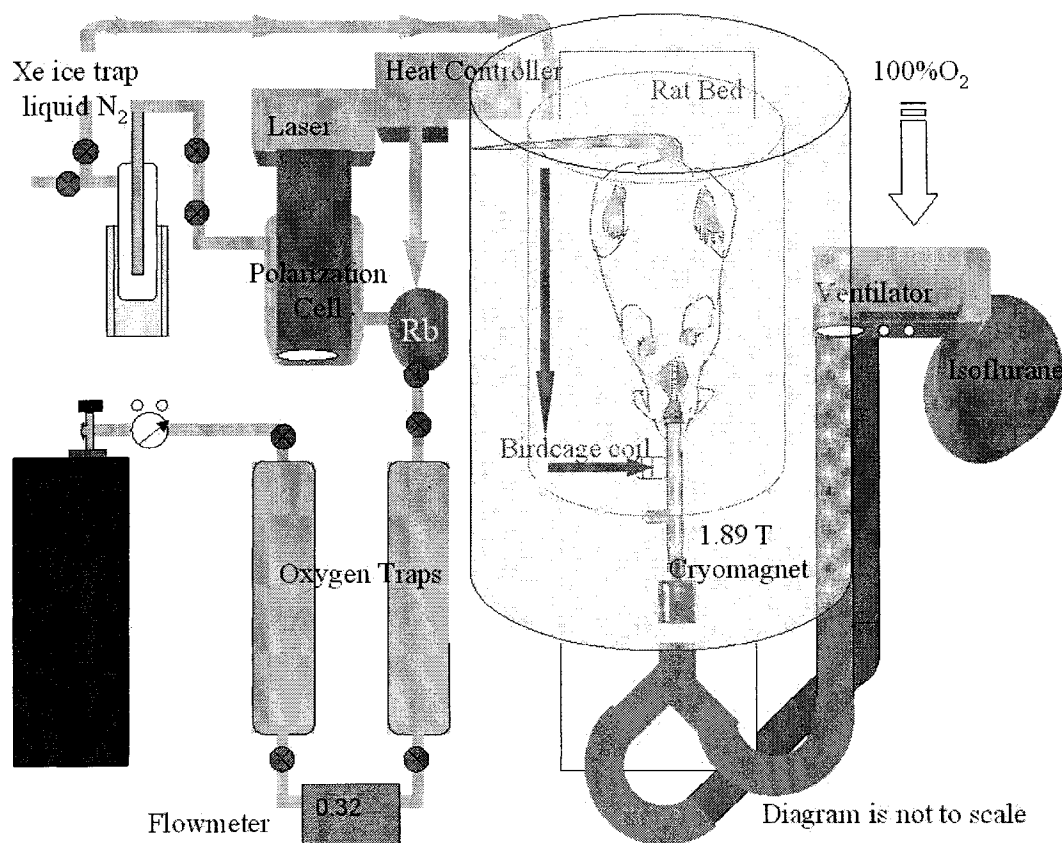


Figure 3.2
Experimental apparatus showing magnet, hyperpolarized xenon flow system, xenon administration system, and tracheostomized rat. Grey arrows show the flow of xenon from the flow system to rat via a three way valve.

The polarization in the hyperpolarized gas was calculated as the product of the thermal polarization (1.78×10^{-6} from a theoretical calculation) and the ratio of the normalized signal from the hyperpolarized sample to that from the thermal sample. A number of

factors affected the polarization achieved, including the age of the cell, the flow rate of xenon, and the temperature of the cell. The polarization was optimized by setting the temperature controller to 180 °C and allowing the rubidium to vaporize. The polarization was determined as above, and the temperature controller incremented slowly (e.g. in 5° increments, until reasonable polarization was reached. As the age of the cell increased, the rubidium oxidized and led to decreased efficiency of polarization.

3.5 Animal Preparation and Histology Grading

All animal experiments were approved by the local ethics committee (Animal Care Committee, Carleton University, Ottawa ON) and were in accordance with the standards of the Canadian Council for Animal care (CCAC 1993). Twelve male Wistar rats (300-350g, Charles River Laboratories, Quebec) were used, of which six were anesthetized with i.m. ketamine/xylazine and exposed to intratracheal instillation of 350 µL of 1.4×10^6 fungal spores/mL suspended in normal saline. The instillation was carried out by Dr. Thomas Rand of St. Mary's University, Halifax, who also performed the histological analysis of the lungs. The animals were transported by air to Ottawa. At 24-48 hours post exposure, diseased rats were anesthetized with 3% isoflurane (Biomedica Animal Health, Cambridge ON) administered via nosecone with a ADS1000 veterinary anesthesia system (Engler Corp, Hialeah FL) connected to a T3150 isoflurane vaporizer (Benson Medical Industries Markham ON). Tracheostomy was performed with a 16 gauge iv catheter (Terumo, Somerset NJ) and secured with ligatures after surgical exposure of the trachea.

Oxygen saturation and heart rate were monitored continuously with a 8500V pulse oximeter (Nonin, Plymouth MN). After tracheostomy anesthesia was continued with the same system set to mechanical ventilation with 100% O₂ (Praxair, Ottawa, ON) and 1.25% isoflurane. All animals tolerated surgery and mechanical ventilation well with no desaturation. After the experiment, the animals were euthanized by i.v. barbiturate injection and the dissected lungs were fixed in formalin and stained with Hematoxylin and Eosin as previously described.(47). Histological grade of inflammation was assessed by determining the percentage of random 250X microscope field occupied by alveolar air space at 20 sites of spore impaction per animal . Grading was assigned according to the degree of alveolar space reduction as follows: 0% , grade 0; less than 10%, grade 1;10-25%, grade 2; 25-50%, grade 3; 50-75%, grade 4; more than 75%, grade 5.

3.6 Data Analysis

3.6.1 Volume Calculation

The volumes were calculated from the 3-D images acquired for each of three xenon breaths per rat. The volume estimation procedure was carried out in Matlab (Mathworks, Natick, MA) by S.White as described previously [109, 110]. Data were zero filled to a matrix of 128 x 128 x 128. After Fourier transformation using the Matlab fft function, magnitude scaled images were constructed. A limit threshold was empirically chosen to separate the signal from the background. The noise parameter σ was estimated by defining Regions of interest (ROIs) on contiguous slices in the field of view (FOV) to

encompass voxels known to be empty. The ROIs were defined such that they encompassed a similar range as the dimensions of the imaged object in the frequency-encode dimension. For a vector m containing the magnitudes of N_m voxels, the maximum likelihood background noise parameter $\hat{\sigma}_{ML}$ was calculated :

$$\hat{\sigma}_{ML} = \sqrt{\frac{1}{2N_m} \sum_{i=1}^{N_m} m_i^2} \quad (3.3)$$

Due to large the FOV used, a large number of voxels in the images consisted of background noise. To reduce the sensitivity of the volume estimation to such voxels, the images were cropped in three dimensions to a FOV with boundaries much closer to the gas volume boundary. ROIs were then drawn in regions of the image assumed to contain “full” voxels and the corresponding N_f voxel magnitudes were stored in a vector f . The maximum likelihood estimator for the sample \hat{A}_{MLfull} was calculated by numerically solving the following equation using the Matlab fsolve function :

$$\hat{A}_{MLfull} - \frac{1}{N} \sum_{i=1}^{N_f} f_i \frac{I_1\left(\frac{\hat{A}_{MLfull} f_i}{\hat{\sigma}_{ML}^2}\right)}{I_0\left(\frac{\hat{A}_{MLfull} f_i}{\hat{\sigma}_{ML}^2}\right)} = 0 \quad (3.4)$$

The frequency of voxel magnitudes in cropped images were then placed in n_{bins} bins centered linearly on values between zero and maximum voxel magnitude. The two

vectors F and M_F contained the frequencies and magnitudes respectively, and were plotted to produce a histogram of voxel magnitudes. To reduce bias between bin magnitude values, A_F was computed by solving the maximum likelihood estimator equation for the magnitude bin values M_F :

$$A_{F_i} - M_{F_i} \frac{I_1 \left(\frac{A_{F_i} M_{F_i}}{\hat{\sigma}_{ML}^2} \right)}{I_0 \left(\frac{A_{F_i} M_{F_i}}{\hat{\sigma}_{ML}^2} \right)} = 0 \quad (3.5)$$

To further reduce the effects of zero signal voxels on volume estimation, a low magnitude cutoff, A_T , was chosen such that voxels in the cropped image with magnitudes below A_T were not included in the volume calculation. The threshold was chosen by alternating between the slice and projection representations of the image as well as the histogram, and choosing the value that rejected as many background voxels as possible without rejecting voxels containing gas signal. Volume was then computed as:

$$V = \frac{FOV}{N_{FE} \cdot N_{PE}^2} \frac{1}{\hat{A}_{MLfill}} \sum_{i=1}^{n_{bins}} A_{F_i} F_i \quad (3.6)$$

for all $A_{F_i} > A_T$, where N_{FE} and N_{PE} are the zero filled dimensions of the image and FOV is the volume of the imaged space. The method assumes that T_1 is long compared to the time of data acquisition. Furthermore, since the “full” voxels in the context of in vivo lung also contain some lung tissue and are not 100% gas, the calculated volumes are properly termed “upper limit” volumes. In phantom studies the volume measurement obtained accuracies of 6% [109].

3.6.2 Determination of Gas Transfer Times (T_{tr})

The sequential spectra obtained for each of five breath-holds for each rat were analyzed as follows. Using a graphical user interface written in MATLAB (Natick, MA), the raw data were zero filled, multiplied by a 30Hz exponential filter, and Fourier transformed. The resulting spectra underwent zero and first order phase correction. Spectral peaks were fitted to a Lorentzian function and the area under each peak determined. The area under each lung parenchyma peak and RBC peak was normalized by the area of the gas peak of the preceding spectrum (hence the need for an initial unpaired “read” pulse at the beginning of the pulse sequence to normalize the spectrum obtained by the first pulse pair). The mean of the five normalized peak area values (based on separate breathholds) were plotted against the corresponding delay time to obtain gas transfer curves for each compartment. The error on each point was calculated as the standard deviation of the five values. A nonlinear least squares fit of the data to Equation 2.59 was performed using MATLAB. The gas transfer parameter was obtained along with the fitting error.

3.6.3 Calculation of Diffusing Capacities

The diffusing capacities for each of the lung parenchyma, RBC, and whole lung were calculated using Equations 2.60, 2.61 and 2.62. Errors for ratios and products of measured quantities were propagated according to standard formulae i.e. the errors of the individual measurements were added in quadrature[113].

3.6.4 Statistical Analysis

Comparison of the group means for normal rats and the diseased rats was performed using Students t-test (two tailed, unequal variance) to calculate the P values [113, 114]. The procedure for each parameter to be compared was as follows. The mean value of the parameter for each group was calculated. The variance for each group (σ_1^2 and σ_2^2) was calculated. The difference between the two means was calculated. The variance of the difference between the two means (σ_d^2) was calculated as follows:

$$\sigma_d^2 = \frac{\sigma_1^2}{n_1} + \frac{\sigma_2^2}{n_2} \quad (3.7)$$

where n_1 and n_2 are the number of subjects in each group. Then the t value was calculated by:

$$t = \frac{\bar{x}_1 - \bar{x}_2}{\sigma_d} \quad (3.8)$$

where the numerator is the difference in the two group means and the denominator is the square root of σ_d^2 . A t-table at $(n_1 + n_2 - 2)$ degrees of freedom with the level of significance required ($p = 0.05$) was used to find the tabulated t value. If the calculated t value exceeded the tabulated value then the means were considered significantly different.

4. Results

The results of the experiments are presented as follows. A typical spectrum of hyperpolarized xenon in rat lung *in vivo*, as well as a sequential plot of multiple spectra obtained during a breath-hold, are presented. Gas transfer curves for diseased and normal rats are shown. A 3-D image of hyperpolarized xenon inflating rat lungs is shown to typify the datasets from which the volume calculations were made. The normal rats and diseased rats are compared with respect to the various measured and calculated parameters. Photomicrographs of rat lung are used to demonstrate the grades of inflammation, and the correlation between histological grade and the xenon diffusing capacities is shown.

4.1 Hyperpolarized Xenon Spectroscopy

4.1.1. Typical Spectrum of Hyperpolarized ^{129}Xe in Rat Lung *in vivo*.

Figure 4.1 shows a spectrum obtained from a rat lung *in vivo*. Three peaks can be seen, corresponding to the gas peak at 0 ppm, the lung parenchyma peak at 196 ppm and the red blood cell peak at 214 ppm. This spectrum corresponds to a long delay time of 5000 ms. A typical stacked plot of the spectra obtained during one breath hold is shown in Figure 4.2. Each spectrum in the series corresponds to a unique delay time.

4.1.2 . Gas Transfer Curves for Diseased and Control Rats.

The areas under the peaks for the red blood cell and lung parenchyma peaks were plotted against the delay time. Some representative plots are shown in Figures 4.3 and 4.4 for diseased and normal rats respectively. For each rat, the lung parenchyma curve and the red blood cell curve are shown on the same page for comparison but on separate axes to preserve clarity. The error bars reflect the mean and standard deviation of five sets of data from 5 separate breath holds. The gas transfer times (T_{tr}) for each compartment corresponding to each plot are listed in Table 4.1. These T_{tr} values were obtained by fitting the data to Eqn. 2.17 as previously described.

4.2 Hyperpolarized ^{129}Xe MRI and Volume Measurements

A representative image of rat lungs during inflation with hyperpolarized xenon is shown in Figure 4.5. This represents a 2-D projection of the 3-D data set in the three orthogonal axes representing the anterior - posterior direction (y-axis), the craniocaudal direction (z-axis) and the left-right direction (x-axis) of the rat. A volumetric rendering of the 3-D data set is shown in Figure 4.6. The volumes for the control and diseased rats are shown in Table 4.1, as the mean and standard deviation of three independent measurements.

4.3 Xenon Diffusing Capacities

The xenon diffusion capacities for the red blood cell and lung parenchyma separately were calculated using Eqn. 2.7 and Eqn.2.8 and are shown for each control and diseased rat in Table 4.2 . The total diffusion capacity was calculated for each animal according to equation 2.10 and is also shown in Table 4.2.

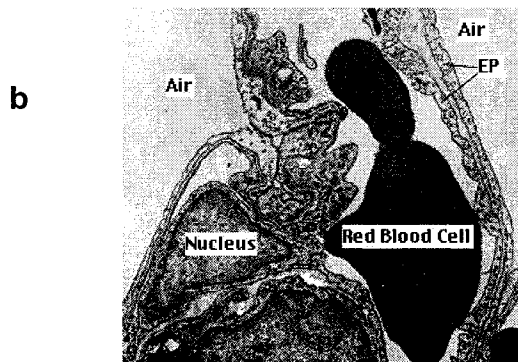
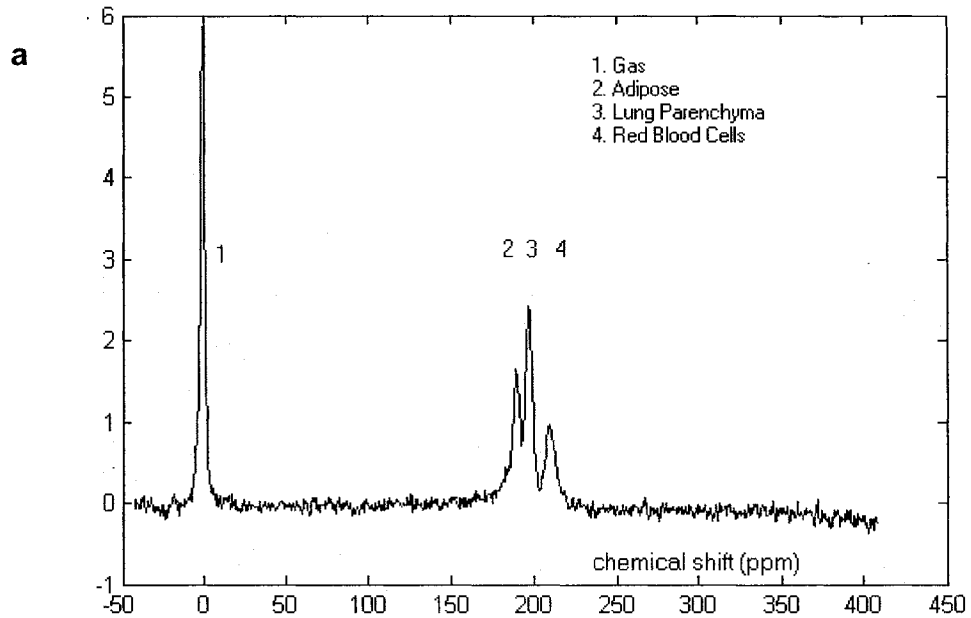
4.4 Histological Grade of Lung Inflammation

Photomicrographs of histological sections from the diseased rats are shown in Figure 4.7, illustrating the characteristics of each grade of inflammation. Magnification is 250X for all photomicrographs. The overall histological grade for each experimental animal is shown in Table 4.2. The correlation of the three diffusing capacities with histological grade are shown in Figures 4.8, 4.9, and 4.10.

4.5 Comparison of the Control and Diseased Groups

Table 4.3 compares the control and diseased rats with respect to the mean and standard deviation of all parameters, including lung volumes, T_{tr} , and diffusion capacities for red blood cell and lung parenchyma. The error in the T_{tr} parameters reflects fitting error (corrected chi square ± 1).

The statistical significance of the difference between the means for each is also shown as a P-value derived from the two tailed Students-t test.



Source: www.usr.rcn.com/biologyPages/pulmonary

Figure 4.1

(a) Typical ^{129}Xe spectrum from in vivo rat lung at delay time of 5000 ms showing gas, lung parenchyma, red blood cell, and adipose tissue/heart resonances. The latter (peak 2) does not appear in the time scales (1-1000 ms) used in the current work. The ordinate is peak amplitude in arbitrary units. (b) Electron micrograph of alveolar-capillary interface showing the anatomical relationship of red blood cells, pneumocytes or lung parenchyma (EP = epithelial cell) and airspaces.

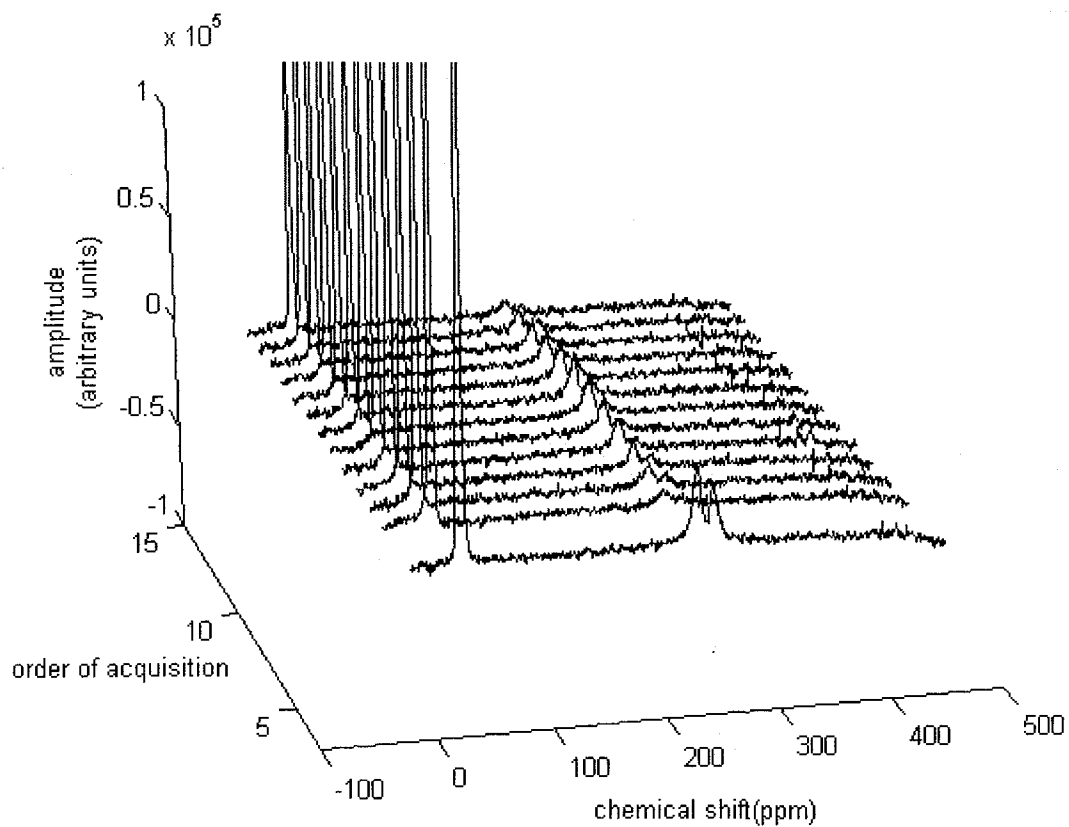
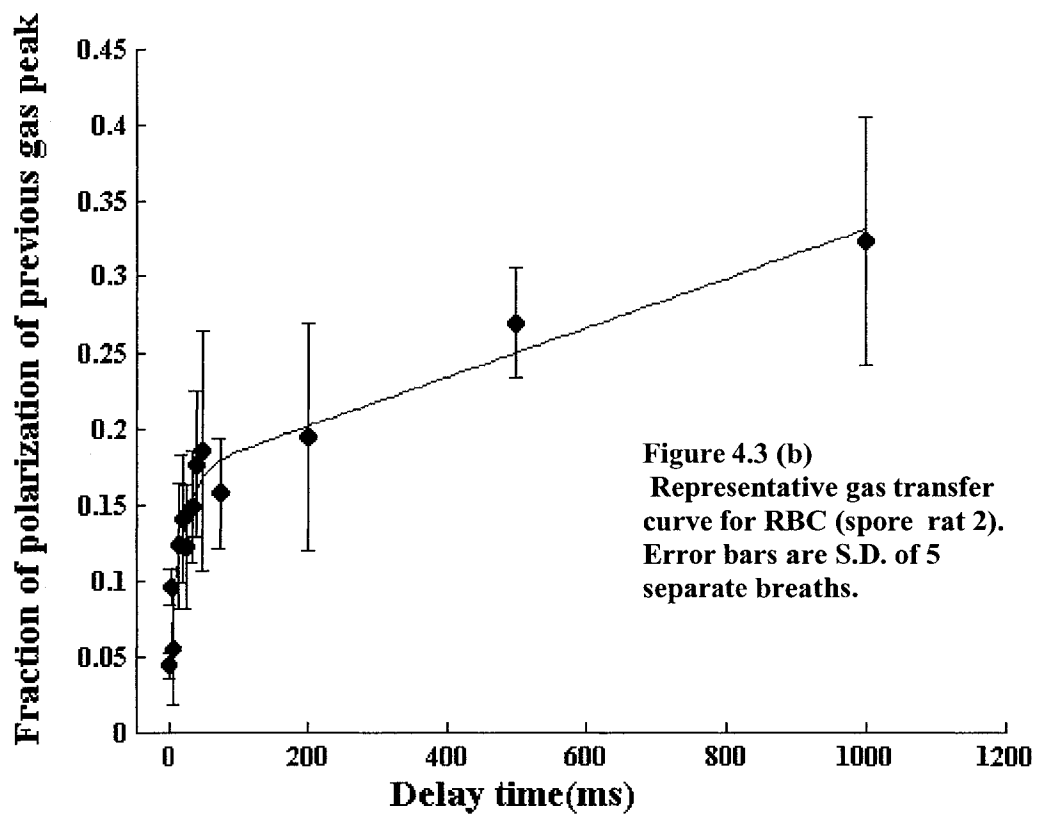
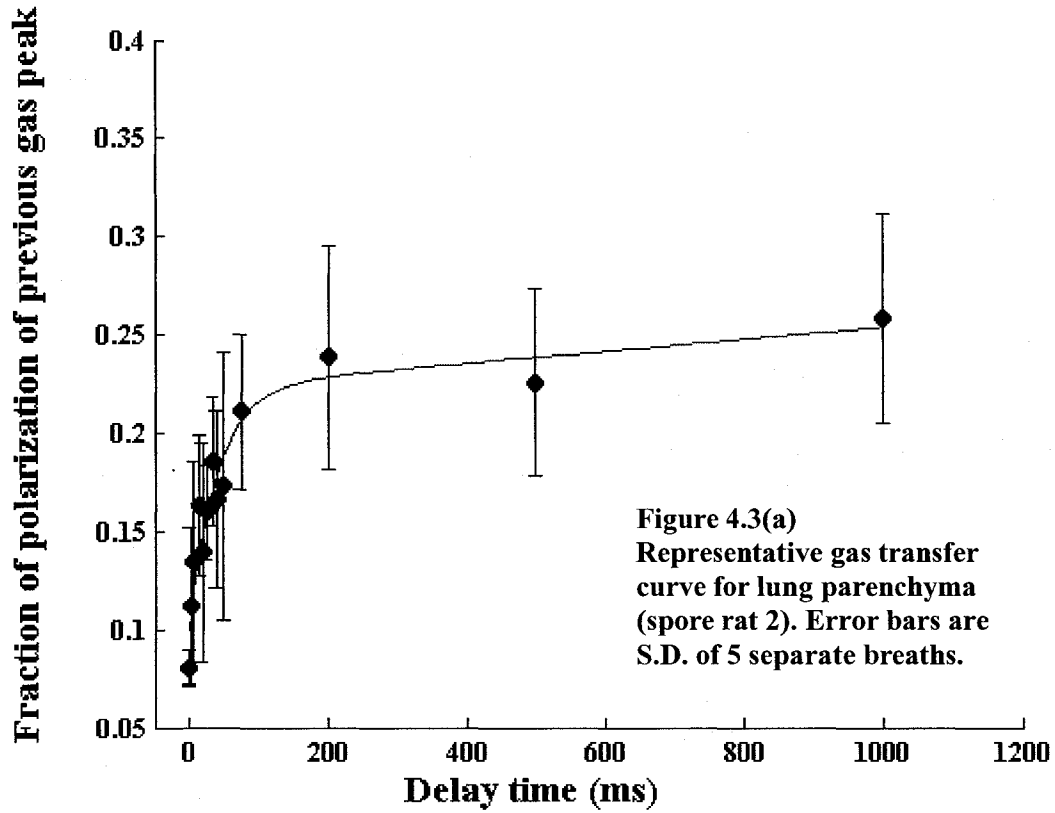


Figure 4.2
Sequential plot of hyperpolarized xenon spectra obtained during a single breath-hold *in vivo*. Each spectrum following the initial spectrum corresponds to a different delay time.



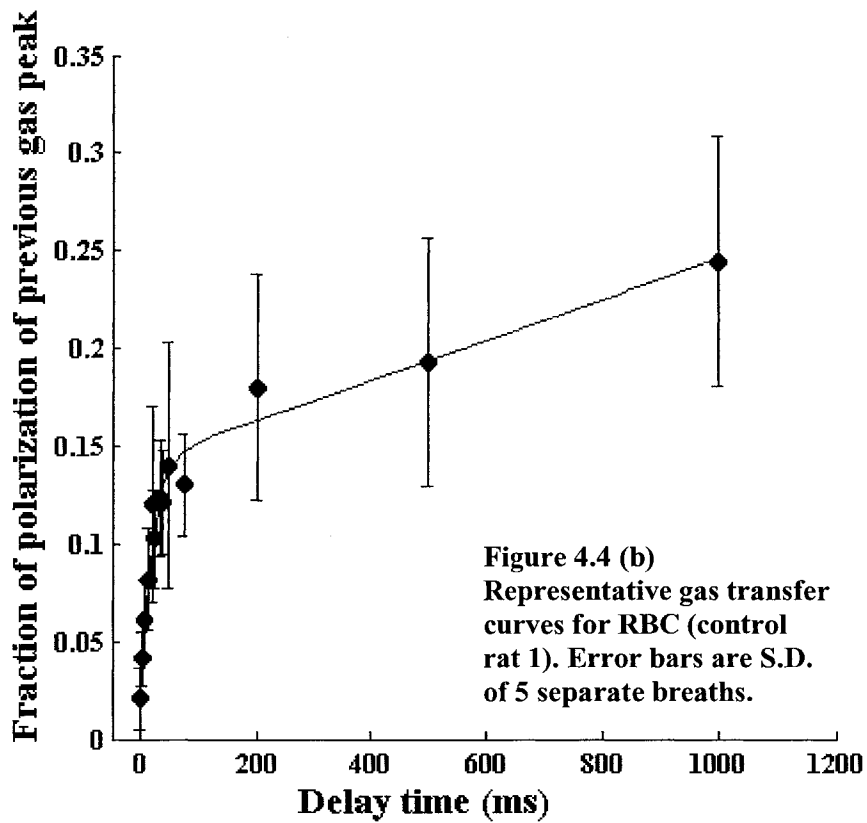
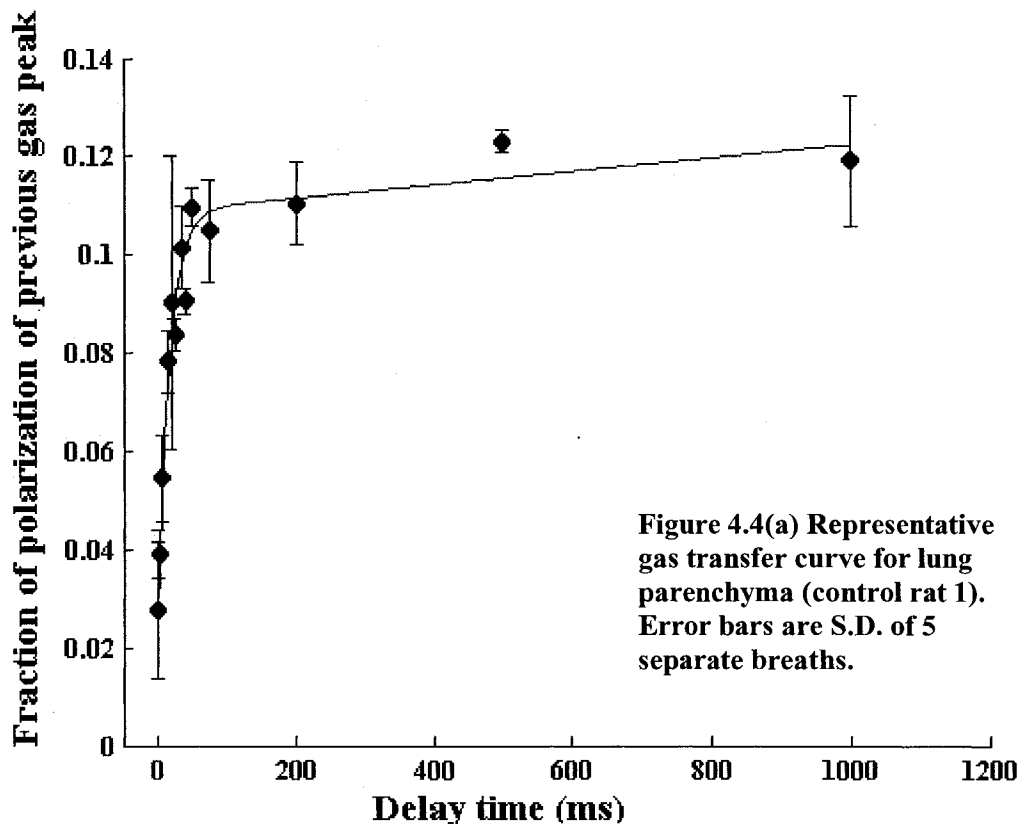


Table 4.1. Comparison of gas transfer times and lung volumes for individual control and diseased rats

Control Rat No.	Ttr _{LP} (ms)	Ttr _{RBC} (ms)	Lung Volume (ml)	Diseased Rat No.	Ttr _{LP} (ms)	Ttr _{RBC} (ms)	Lung Volume (ml)	Histo-logy Grade
1	17.3±2.9	20.7±4.6	16.4±4.5	1	42.9±9.1	40.2±25.1	12.3±2.4	2
2	22.43±5	32.3±8.4	14.4±0.8	2	40.41±2.3	19.3±8.35	11.8±0.7	3
3	24.4±6.0	24.3±6.6	16.2±0.9	3	29.9±10.2	22.7±8.5	10.6±1.6	4
4	20.5±4.2	31.6±4.3	14.2±0.3	4	28.1±7.4	24.2±10.8	8.2±1.4	4
5	23.9±4.0	16.3±3.4	15.5±0.1	5	24.1±7.9	11.6±2.7	14.4±1.6	1
6	22.2±3.7	11.3±4.2	19.0±0.9	6	42.4±9.6	33.1±22.5	11.6±2.4	4
mean±SD	21.8±2.6	22.8±8.3	16.0±1.8	mean±SD	34.6±8.2	25.2±10.1	11.5±2.0	

Table 4.2. Comparison of D_{LXeRBC}, D_{LXeLP}, and D_{LXe} for individual control and diseased rats

Control Rat No.	D _{LXeLP} (ml/min/mmHg)	D _{LXeRBC} (ml/min/mmHg)	D _{LXe} (ml/min/mmHg)	Diseased Rat No.	D _{LXeLP} (ml/min/mmHg)	D _{LXeRBC} (ml/min/mmHg)	D _{LXe} (ml/min/mmHg)	Histo-logy Grade
1	72.1±23.2	60.2±41.0	32.8±23.0	1	21.9± 6.2	23.4±6.8	11.3±4.0	2
2	48.8±8.1	33.9±14.6	20.0±9.2	2	22.2±6.9	46.4±12.4	15.0±6.1	3
3	50.5±12.8	52.1±19.5	25.9±11.7	3	27.1±10.0	35.5±11.2	15.4±7.2	4
4	53.8±10.8	34.3±15.3	20.8±10.3	4	22.6±6.9	25.9±5.6	12.0±4.1	4
5	49.4±8.4	72.4±16.6	29.3±8.4	5	45.3±15.7	94.0±22.4	30.6±12.3	1
6	65.5±11.4	128.2±87.2	43.3±30.4	6	20.8±6.4	26.5±11.4	11.6±5.6	4
mean±SD	56.5±9.8	63.5±35.0	28.7±8.7	mean±SD	26.6±9.4	41.2±26.9	16.0±7.4	

Table 4.3. Comparison of parameter means (+/- SD)for the control and diseased groups

Parameter	Control Group	Diseased Group	P-value
Ttr _{LP} (ms)	21.8±2.6	34.6±8.2	0.006
Ttr _{RBC} (ms)	22.8±8.3	25.2±10.1	0.66
Lung Volume (ml)	16.0±1.8	11.5±2.0	0.004
D _{LXeLP} (ml/min/mmHg)	56.5±9.8	26.6±9.4	< 0.001
D _{LXeRBC} (ml/min/mmHg)	63.5±34.9	41.9±26.9	0.15
D _{LXe} (ml/min/mmHg)	28.7±8.7	16.0±7.3	0.011



FIGURE 4.5 Maximum intensity projection of the volumetric 3-D image of xenon in rat lung *in vivo* in the x axis (right surface), the y axis (upper surface), and z axis (bottom). These projections correspond to transverse, coronal and axial projections respectively. Courtesy Steven White

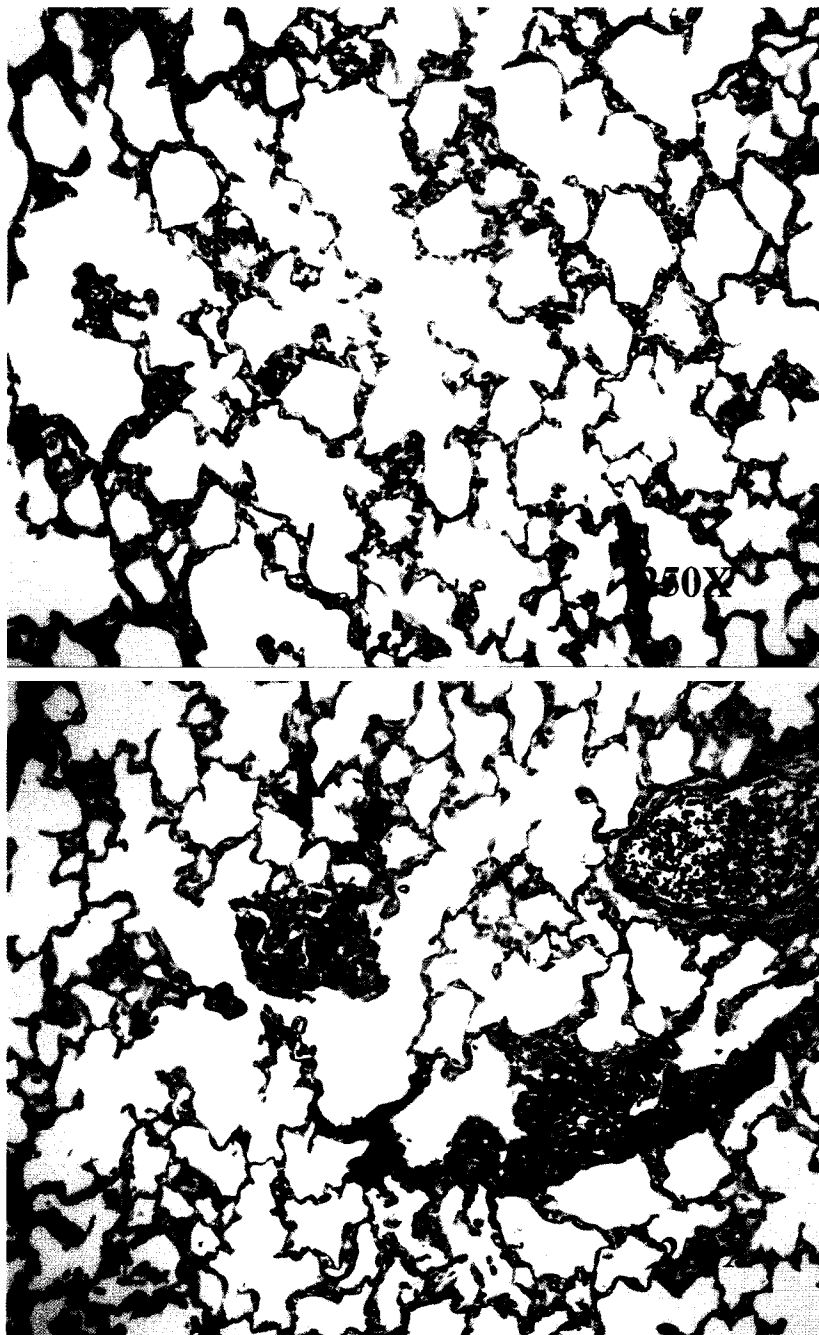


FIGURE 4.6. Hematoxylin-eosin stained rat lung showing grade I inflammation (top) and grade 2 inflammation (bottom) in diseased animals intratracheally instilled with *Stachybotrys chartarum* spores. Courtesy Thomas Rand

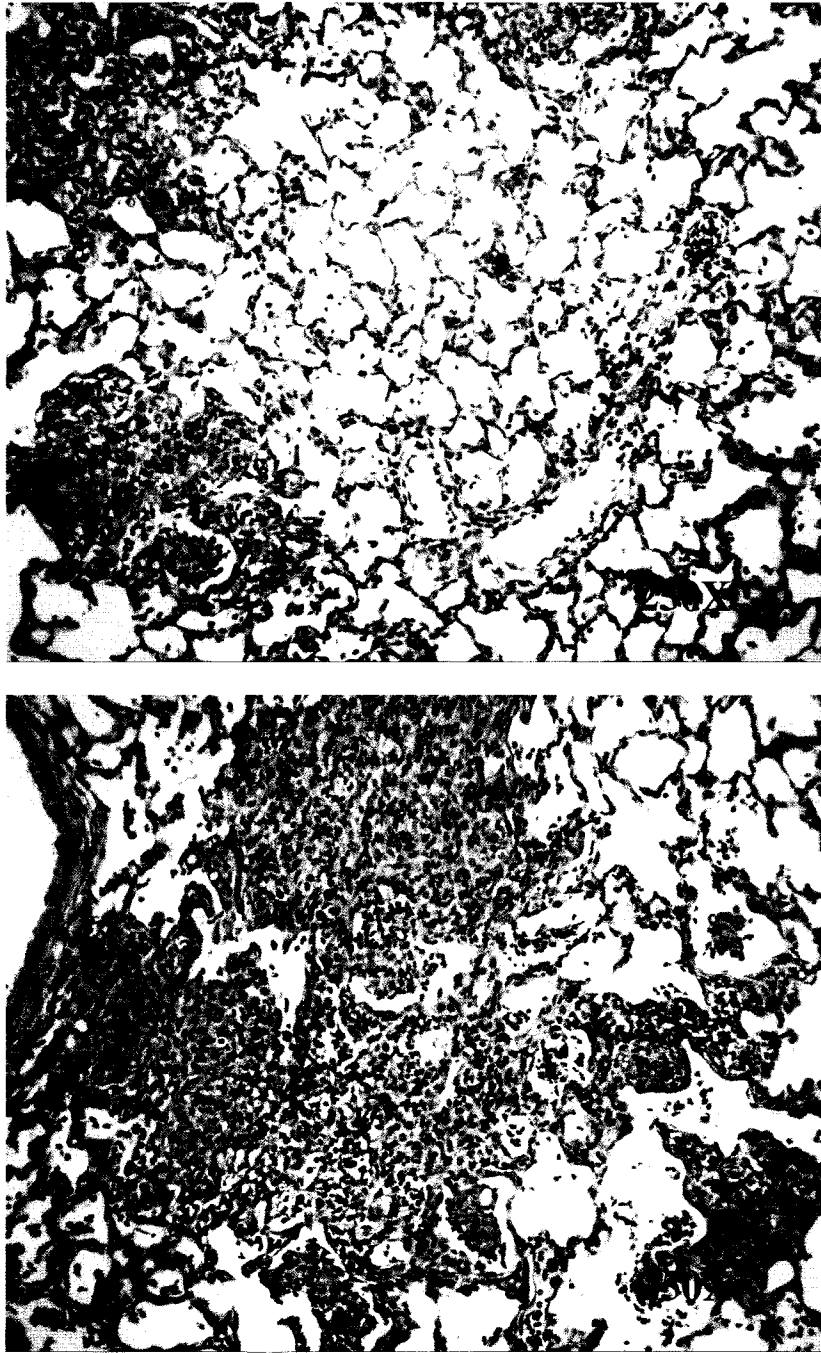


FIGURE 4.7. Hematoxylin-eosin stained rat lung showing grade 3 inflammation (top) and grade 4-5 inflammation (bottom) in diseased animals intratracheally instilled with *Stachybotrys chartarum* spores. Increased destruction of alveolar spaces with fibrotic granulomatous reaction is evident with increasing histological grade. Courtesy Thomas Rand.

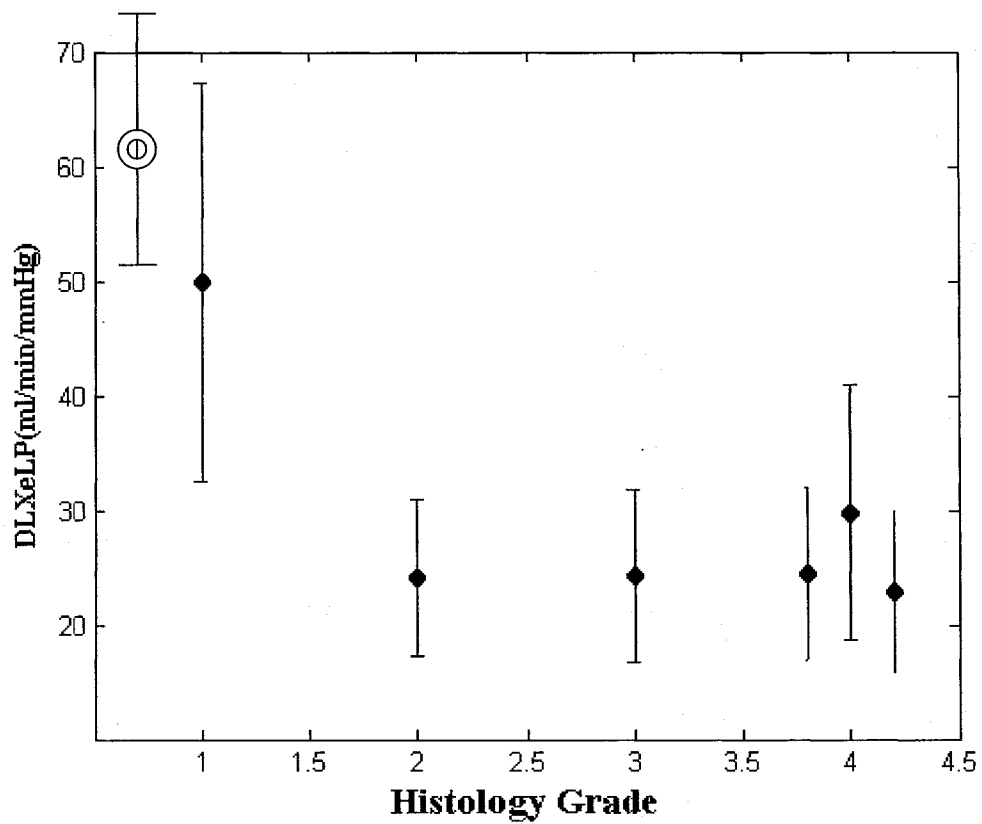


FIGURE 4.8. Correlation of xenon diffusing capacity for lung parenchyma (D_{LXeLP}) with histology grade in diseased rats. The three bars at right are actually histology grade 4 but are offset for clarity. Open circle represents mean and S.D. of 5 normal rats.

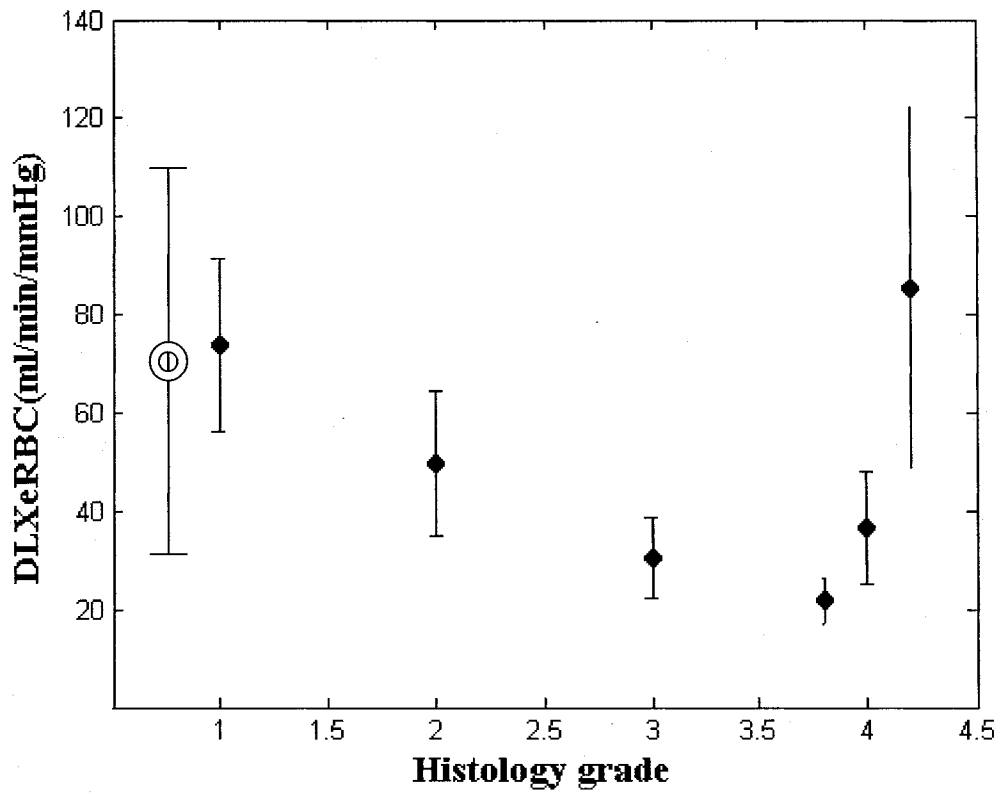


FIGURE 4.9. Correlation of xenon diffusing capacity for red blood cells (D_{LXeRBC}) with histology grade in diseased rats. The three bars at right are actually histology grade 4 but are offset for clarity. Open circle represents mean and S.D. of 5 normal rats.

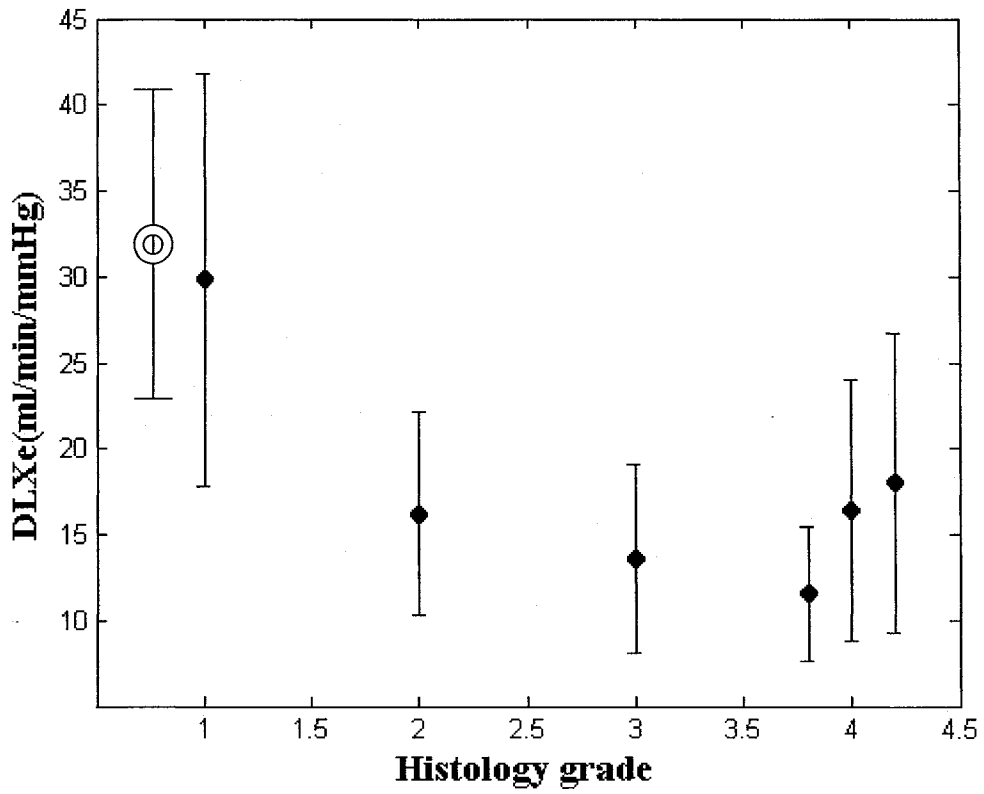


FIGURE 4.10. Correlation of xenon diffusing capacity for lung (DL_{Xe}) with histology grade in diseased rats. The three bars at right are actually histology grade 4 but are offset for clarity. Open circle represents mean and S.D. of 5 normal rats.

5. Discussion and Future Work

5.1 Restatement of Results and Comparison with Previous Work

The gas transfer times for the lung parenchyma in control rats, as well as the increase seen in rats with lung inflammation, are consistent with those reported by Mansson et al [91]. In a LPS model of lung inflammation, the control rats had transfer times for lung tissue and red blood cells of 29 ± 4 ms and 25 ± 4 ms respectively, while corresponding values for the LPS rats were 40 ± 5 ms and 31 ± 8 ms. The rats used in that study were also male Wistars; the method of xenon administration consisted of multiple air breaths followed by three xenon breaths, the last of which was prolonged for a seven second breath hold, and a tidal volume of 1ml/kg was used. The present investigation used a constant pressure method as opposed to a constant volume method, and the xenon was administered as a single breath close to TLC. It is likely that the volumes of the lungs were different. Since k_{CO} increases exponentially with decreased V_A , the net result is a slight reduction in D_{LCO} at lower lung volumes [97]. The gas transfer times correspond to the inverse of the xenon equivalent of k_{CO} , which would lead to higher transfer times at lower lung volumes. Hence, the values obtained in the current work are reasonable.

The lung volumes measured by hyperpolarized xenon MR imaging are somewhat higher than values reported for total lung capacity by plethysmography. Total lung capacity was found to be 12.23 ± 0.55 ml in anesthetized, tracheostomized Sprague Dawley rats weighing 307 ± 10 g [115]. The higher value of lung volume in normal rats (16 ± 2 ml)

found in the current work may reflect xenon in additional volumes such as alveolar tissue and pulmonary capillary as well as volume averaging over voxels at the lung boundary. Furthermore, the algorithm used defines the highest intensity voxel in the image as being 100% gas, which leads to an overestimate of volume as high as 20% [109]. However, other authors have predicted somewhat higher volumes; for example for 348 g Sprague Dawley rats 17.5 ml has been predicted [36], which is in good agreement with the volumes obtained from hyperpolarized ^{129}Xe MR imaging. Hence, the lung volume measurements are also reasonable.

5.2 Comparison of Xenon Diffusing Capacity and D_{LCO} .

The xenon diffusing capacity as defined above is analogous to but not identical with, the D_{LCO} . Most importantly, the D_{LCO} is measured over a 8 second time period, while the xenon diffusion capacity described in the present work is measured over a 1 second period with most of the exponential change occurring over tens to hundreds of milliseconds. Consequently, the D_{LCO} is measuring a much slower process of absorption than the xenon measurement, leading to a smaller time constant (or k_{CO}) and a smaller numerical value for the D_{LCO} in comparison to the xenon diffusing capacity. Hence, the xenon measurement will be sensitive to changes in gas diffusion on short time scales and may provide a window into gas diffusion in vivo which is different from D_{LCO} .

The carbon monoxide diffusing capacity in rats has been predicted as a function of body weight by Takazawa *et al.* For a 300 g rat, the D_{LCO} measured over a 8 second breath-hold is predicted to be 0.181 ml/min/mmHg[115]. The diffusivity of xenon

(solubility/square root of molecular weight) can be calculated to be 7.65 times that of CO, using MW of 129 and 28 and solubilities (Bunsen coefficients) in plasma at 37 °C of 0.353 [68] and 0.0215 [35]. Multiplying by the factor of 7.65, the xenon diffusing capacity corresponding to the 8 second breath-hold is 1.385 ml/min/mmg Hg. The xenon diffusing capacities measured in the current study are much greater, by an order of magnitude. This is accounted for by the much shorter time scale (less than 1s) over which the xenon measurements were made, leading to a much shorter T_{tr} and consequently a larger time constant. It is not known whether measurement of xenon diffusing capacity over a longer time scale would yield values similar to the D_{LCO} . Such long time scales were avoided in this study to avoid hypoxia and physiological compromise of rats. Ruppert *et al* however, have shown that with respect to T_{tr} of xenon in dogs, the peak areas showed a rapid increase to a plateau value at inter-pulse delay times of 500 ms to 1000 ms, and then a further rise and second plateau at delay times approaching 9 seconds [86]. It is likely that if the xenon diffusing capacities were to be measured over those time scales, other time constants of exponential recovery would be found.

5.3 Interpretation of Current Results

Of the three measured quantities (T_{trRBC} , T_{trLP} and lung volume), the latter two are significantly different in the diseased and normal rats. The increased T_{trLP} is likely due to the fibrosis and inflammation demonstrated histologically, which pose a barrier to gas diffusion. The T_{trRBC} is not significantly different, indicating that the disease model presented here does not cause significant changes in the diffusion properties of the

capillary bed. One would expect some change in this parameter, since both blood vessels and lung parenchyma are affected by the inflammatory changes, but one possible explanation is that blood vessels in areas of inflammation contribute relatively little to the RBC peak, perhaps due to preferential distribution of xenon to areas of lung with relatively normal compliance (see below). Thus, determination of xenon diffusing capacities in localized regions of lungs might be of interest.

Of the three derived parameters (D_{LXeLP} , D_{LXeRBC} , and D_{LXe}) the first is the strongest discriminant of abnormal gas exchange. D_{LXeLP} is much greater for normal rats compared to diseased rats (56 ± 11 ml/min/mmHg vs 27 ± 9 ml/min/mmHg, $p < 0.001$). The D_{LXeRBC} was not significantly different between the normal and the diseased rats (64 ± 35 ml/min/mmHg vs 42 ± 27 ml/min/mmHg, $p = 0.15$), despite a trend to being reduced in the latter group. This was due to the large degree of scatter in the gas transfer curves for the red blood cell compartment, reflecting a lower SNR relative to the lung parenchyma peak. The overall diffusing capacity D_{LXe} was also significantly higher in the control rats than the diseased rats (29 ± 9 ml/min/mmHg vs 16 ± 7 ml/min/mmHg, $p = 0.01$) and is also a good discriminant of abnormal gas exchange.

While there are no previous published measurements of xenon diffusing capacity to compare these results with, the proportional change in xenon diffusing capacity observed was similar to the degree of reduction in D_{LCO} reported with other rat disease models. For example, in an ozone induced model of lung inflammation, 20% reduction in D_{LCO} was reported [116], which is similar to the 50% reduction in D_{LXeLP} seen here. In an experimental model of rat lung inflammation using intratracheal paraquat, a 25% reduction in D_{LCO} was found, with a 69% reduction at 36 hours post instillation [117]. A

radiation model of lung fibrosis found reductions of 25% in D_{LCO} relative to control lung, although that was a chronic model over four months [118]. Hence, the percentage changes in xenon diffusing capacity found in the current work are in keeping with previous work, which increases confidence in the measurement.

The correlation of the changes in the above parameters with histological grade is interesting. The one rat with a relatively low degree of inflammation (grade 1) had parameters more similar to the normal rats than the rats with greater degrees (grades 2-4) of inflammation, as shown in Figures 4.8 to 4.10. Within the more severely inflamed rats, similar reductions in lung volume and D_{LXcLP} and D_{LXe} and similar increases in T_{trLP} were seen. This may be due to the complexity of the disease (i.e. heterogeneous distribution of granuloma, a variable volume of lung tissue being affected). While sampling error is also possible, it is striking that all the different grades of lung inflammation led to qualitatively similar changes in the D_{LXcLP} , T_{trLP} and lung volume. This may imply that a certain threshold volume of granulomatous tissue is responsible for much of the change seen, and that further inflammation contributes relatively little to these measured parameters of gas exchange. The distribution of xenon during the breath hold would likely be preferentially distributed to areas with higher compliance i.e. normal lung and lung with minimal inflammation. The more heavily involved areas of lung, receiving relatively little ventilation, may have a correspondingly reduced contribution to the sum of transfer times over all alveoli. The diffusing capacities would in that case be paradoxically more sensitive to lower or intermediate grades of inflammation and less sensitive to higher grades of inflammation, in which low compliance would result in “undersampling” of more heavily diseased alveoli. In general, the measured T_{trLP} can be expected to be a

function of both actual gas exchange barriers on the level of individual alveoli, and the distribution of the alveoli with respect to compliance. With respect to T_{trRBC} , there was no significant difference between the normal and diseased rats, although the standard deviation was higher than for the T_{trLP} . This may reflect the relative paucity of capillaries in the diseased areas of lung (see Figure 4.6 and 4.7) with most RBCs passing through relatively normal lung. Interestingly, there does seem to be an inverse correlation between D_{LXeRBC} and histological grade (Figure 4.9) .

In summary, these results are encouraging in that clear differences are demonstrated between the normal and diseased rats, with the latter evidencing reductions in gas exchange i.e. longer T_{trLP} , and lower D_{LXeLP} and D_{LXe} .

5.4 Sources of Error

The lung volumes were determined to an average error of 6% for normal rats and 13% for diseased rats. The T_{trLP} fitting error was 18% on average for the normal rats and 27% for the diseased rats. The T_{trRBC} fitting error was 24% on average for normal rats and 46 % for diseased rats. Hence, the gas transfer times contribute the most error to the calculated xenon diffusing capacities, and there is a tendency for the diseased animals to have more variability .

The volume of xenon administered during each breath-hold can be assumed to be reproducible given the relatively low error of the lung volume measurement. The measurement of volume is actually an upper limit estimate, due to the fact that a maximal intensity voxel was assumed to be 100% xenon. In future, use of the tracheal signal as the “full” voxel will improve the volume estimates.

There are several sources of the variability in the gas transfer times. The system of pressure actuated valves and tubing used to deliver the sublimated xenon to the rat is one. Another is the phase of the ventilatory cycle at which the three way valve at the intratracheal cannula is shut off to the ventilator and opened to the xenon delivery system. Depending on the timing, there may be greater or lesser amounts of the oxygen/isoflurane mixture remaining in the rats' lungs. Thirdly, there could be some variability in the triggering of the pulse sequence, leading to slight changes in the volume at which the spectra were acquired. Finally, there may be physiological changes in the rats lungs with successive inhalations of xenon as the experiment proceeds, although the physiological state of the rats as measured by O₂ saturation and heart rate was not compromised in any of the experiments.

Improvement in SNR and hence reduction in error can also be achieved by the use of multiple xenon breaths as shown by Mansson et al [91].

5.5 Future Work and Conclusions

The work presented here suggests that the xenon diffusing capacity may be a useful measure of gas exchange, which merits further evaluation.

5.5.1 Measurement of Xenon Diffusing Capacity in other Experimental Models of Lung Disease

The xenon diffusing capacity D_{LXe} , and D_{LXeLP} were good discriminators of pulmonary disease in the *Stachybotrys chartarum* spore instillation model, where the diffusion barrier was found to be mainly associated with the lung parenchyma and not the red blood cell compartment. This disease model corresponds to the category of diseases causing diffuse loss of alveolar units, such as idiopathic pulmonary fibrosis and hypersensitivity pneumonitis, in which V_A is low, k_{CO} is low, and D_{LCO} is markedly reduced [28]. In this study, the corresponding xenon parameters showed a similar pattern, of low lung volumes, increased T_{trLP} or decreased K_{XeLP} , and markedly reduced D_{LXe} . In clinical practice, D_{LCO} is often low in the above diseases and it would not be unreasonable to expect that the xenon diffusing capacity would parallel the D_{LCO} in being useful in these conditions, although the direct comparison has not yet been done. In contrast, D_{LXeRBC} , was not a good discriminator of diseased and control rats. According to Hughes and Pride the k_{CO} is found to be decreased in four distinct disease groups: diffuse alveolar damage, pulmonary hypertension, intrapulmonary shunting, and airflow obstruction [28]. Since the k_{CO} reflects both alveolar and capillary components, a low k_{CO} could correspond to a higher T_{trLP} or T_{trRBC} or a combination of both. Furthermore, lung volume is lower in diffuse alveolar damage and airflow obstruction. This implies that the xenon diffusing capacity might be expected to be most reduced in these two disease groups. Furthermore, the T_{trRBC} and D_{LXeRBC} might be more sensitive than the corresponding parameters for the lung parenchyma in those disease groups where capillaries are destroyed i.e. pulmonary hypertension. It would therefore be of interest to extend these measurements to these disease models.

5.5.2 Measurement of Xenon Diffusing Capacity in Human Subjects

The method of administration presented in the current work permits the acquisition of spectra at constant pressure in a single breath, which will likely be important in human subjects in whom constant pressure breaths will be easier to replicate than constant volume breaths. Since xenon spectra from human volunteers have been obtained from lungs and brain [119], the extension of the method to human subjects is likely to be straightforward. The larger volume of the human lung would improve SNR relative to the rat lung. While it would be important to investigate possible anesthetic effects of the xenon, as healthy volunteers breathing 300-500cc of xenon reported numbness and nausea which was ascribed to the anesthetic effects of xenon, the time course of the study is relatively rapid, facilitating the washout of xenon between breaths. This would be expected to minimize any adverse effects. The larger volume of xenon in a human chest also raises the possibility of spatially localized diffusing capacities for red blood cells and lung parenchyma, although this will require significant improvements in SNR such as increased polarization or improvements in coil design.

Extension to humans is important because the D_{LCO} is often used to make critical decisions regarding therapy, such as initiation of immunosuppressive therapy or lung surgery [39]. Xenon diffusing capacity measurement is likely to be useful in the same contexts if it permits further stratification of human disease. Standardizing the terminology of the xenon diffusion study with that of the carbon monoxide diffusion

capacity will also facilitate its eventual acceptance by clinicians. While much future work will be required before xenon diffusion capacities and gas transfer times play a role in clinical decision making, the current results support further evaluation of the method .

5.5.3 Conclusions

Several conclusions can be drawn from these results. Specifically, the research questions corresponding to the hypotheses stated in the introduction can be answered, with reference to Figures 5.1 and 5.2 which present the measured and calculated parameters for the diseased and normal rats in a graphical format. Each question and its answer are as follows:

(i). can gas transfer times (T_{tr}) for the lung parenchyma and RBC compartments be reliably determined in normal rats and rats diseased by *Stachybotrys chartarum* spore induced pneumonitis?

The answer is yes for the lung parenchyma compartment, as the normal and diseased groups show a standard deviation of approximately 10% and 25% respectively for T_{trLP} . The determinations for the red blood cell compartment remain much more variable with standard deviations of about 40% for T_{trRBC} .

(ii). can xenon diffusing capacities for lung parenchyma and RBC be calculated reproducibly for normal and diseased rats?

The answer is yes for the lung parenchyma compartment which has a standard deviation of about 16% for D_{LXeLP} in normal rats and 30% in diseased rats. For the RBC compartment (D_{LXeRBC}) the answer is no, as there was a much greater variability in the

normal and the diseased groups. The significance of this variability is uncertain, and may represent the poorer SNR of the smaller RBC resonance.

(iii). are these measures of gas exchange significantly different between the two groups ?

The answer is yes for the T_{trLP} ($P=0.006$), lung volume ($P=0.004$), D_{LXeLP} ($P<0.001$), and D_{LXe} ($P=0.01$), which show a significant difference between the groups. The answer is no for the T_{trRBC} ($P=0.66$) and the D_{LXeRBC} ($P=0.15$), which are not significantly different.

(iv). is there a correlation between the severity of histological changes and these measures of gas exchange in the diseased animals?

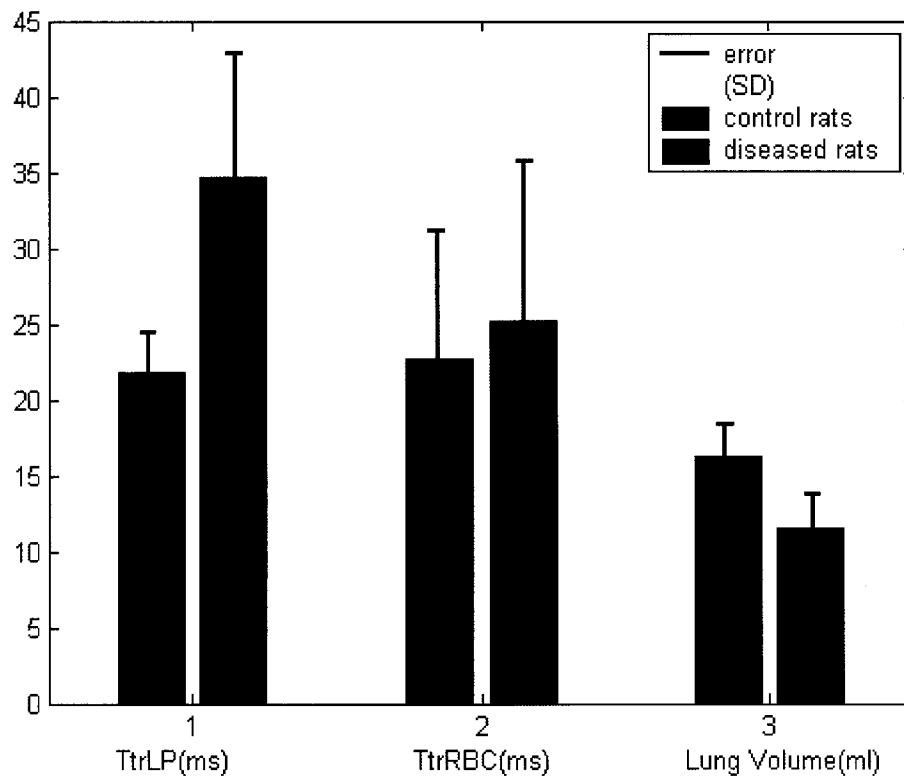


Figure 5.1 Comparison of normal and diseased animals with respect to measured parameters

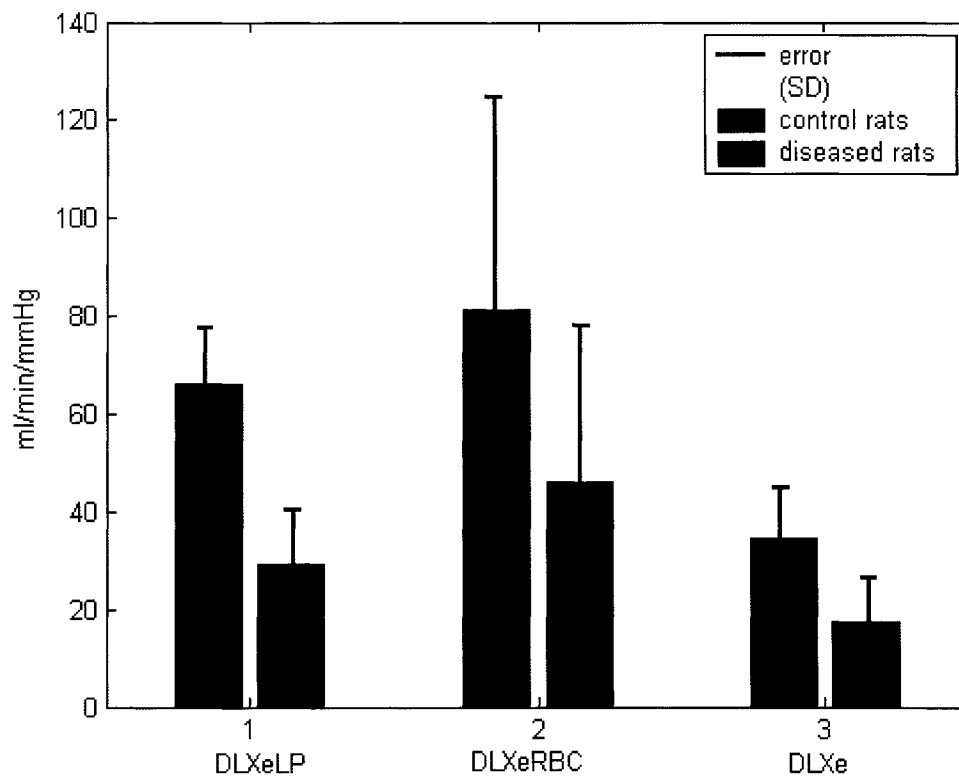


Figure 5.2 Comparison of normal and diseased animals with respect to calculated parameters

The answer is yes, as more severe histology was associated with decreased D_{LXeLP} , D_{LXeRBC} , and D_{LXe} , although the sample size was small.

The results reported here support the further evaluation of the xenon diffusing capacity as a measure of gas exchange in animal and human subjects. Of particular interest is the potential clinical application in detection of early stages of lung inflammation although further reductions in the error in the measurement are required for this to be feasible.

References

- [1] Roca J, Rodriguez-Roisin R, Wagner PD, Pulmonary and peripheral gas exchange and their interactions. pp 1-25. In : *Pulmonary and peripheral gas exchange in health and disease*. Roca J, Rodriguez-Roisin R, Wagner PD (editors). Vol 148 in the series « *Lung biology in health and disease* » Marcel Dekker (2000).
- [2] Piiper J, Scheid P, Model for capillary alveolar equilibration with special reference to O₂ uptake during hypoxia, *Respir. Physiol.* 46 :193-208 (1981).
- [3] NHLBI morbidity and mortality chartbook, 2000. Available at <http://www.nhlbi.nih.gov/resources/docs/cht-book.htm>.
- [4] Statistics. World Health Report 2000. World Health Organization, Geneva. 2000. Available from URL: <http://www.who.int/whr/2000/en/statistics.htm>.
- [5] Murray CJ, Lopez AD. Alternative projections of mortality and disability by cause 1990-2020: Global Burden of Disease Study. *Lancet.* 1997;349:1498-1504.
- [6] Lorenz JN, A practical guide to evaluating cardiovascular renal and pulmonary function in mice. *Am J Physiol. Regulatory Integrative Comp Physiol* 282:R1565-R1582 (2002).
- [7] Schuster DP, Kovacs A, Garbow J, Recent advances in imaging the lungs of small animals. *Am J Resp Cell Mol Biol* 30:129-138 (2004).

- [8] Roca J, Rodriguez-Roisin R, Wagner PD. Pulmonary and Peripheral Gas exchange and their interactions, pp. 1-25. In : *Pulmonary and peripheral gas exchange in health and disease*. Roca J, Rodriguez-Roisin R, Wagner PD (editors). Vol 148 in the series « *Lung biology in health and disease* » Marcel Dekker (2000).
- [9] Albertine KH. Structural organization and quantitative morphology of the lung. In: *Application of magnetic resonance to the study of the lung*. Cutillo AG and Ailion DC (editors). Blackwell Futura Publishing, New York (1996).
- [10] Staub NC, Schiltz EL. Pulmonary capillary length in dog cat and rabbit. *Respir. Physiol.* 5:371-378 (1968).
- [11] Schlosser D, Heyse E, Bartels H. Flow rates of erythrocytes in the capillaries of the lung. *J. Appl. Physiol.* 20:110-112 (1965).
- [12] Johnson RL, Spicer WS, Bishop JM, Forster RE, Pulmonary capillary blood flow and diffusing capacity during exercise, *J. Appl. Physiol.* 15 :893-902 (1960).
- [13] Wagner PD. Diffusion and chemical reaction in pulmonary gas exchange. *Physiol. Rev.* 57:257-312 (1977).
- [14] Riley RL, Cournand A, 'Ideal' alveolar air and analysis of ventilation perfusion relationships in the lungs. *J. App. Physiol.* 1:825-847 (1949).
- [15] Ball WCJ, Steward PB, Newsham LGS, Bates DV, Regional pulmonary function studied with Xenon 133. *J Clin Invest.* 41:519-531 (1962).
- [16] Dolfuss RE, Milic-Emili J, Bates DV, Regional ventilation of the lung studied with boluses of 133 xenon, *Resp. Physiol.* 2:234-246 (1967).
- [17] West JB, Dollery CT, Distribution of blood flow and ventilation-perfusion ratio in the lung measured with radioactive CO₂. *J. Appl. Physiol.* 15:405-419(1960).

- [18] Glenny RW, Lamm JEM, Albert RK, Robertson HT, Gravity is a minor determinant of pulmonary blood flow distribution. *J. Appl. Physiol.* 71:629-629 (1991).
- [19] Fahri LE, Elimination of inert gas by the lung. *Respir. Physiol.* 3:1-11 (1967).
- [20] Wagner PD, Saltzmann HA, West JB, Measurement of continuous distributions of ventilation-perfusion ratios:theory. *J. Appl. Physiol.* 36:588-599 (1974).
- [21] Wagner PD, Laravuso RB, Uhl RR, West JB, Continuous distributions of ventilation-perfusion ratios in normal subjects breathing air and 100% O₂. *J. Clin. Invest.* 54:54-68 (1974).
- [22] Johnson RL, Curtis SE, Experimental approaches to the study of gas exchange. pp 45-119. In : *Pulmonary and peripheral gas exchange in health and disease*. Roca J, Rodriguez-Roisin R, Wagner PD (editors). Vol 148 in the series « *Lung biology in health and disease* » Marcel Dekker (2000).
- [23] Lilienthal JL, Riley RL, Proemmel DD, Franke RE, An experimental analysis in man of the pressure gradient from alveolar air to arterial blood during rest and exercise at sea level and at high altitude. *Am. J. Physiol.* 174:199-216 (1946).
- [24] Schuster KD, Kinetic of pulmonary CO₂ transfer studied by using labelled carbon dioxide C¹⁶O¹⁸O. *Respir. Physiol.* 60:21-37 (1985).
- [25] West JB. *Pulmonary pathophysiology: the essentials, 5th edition*. Williams and Wilkins (1995).
- [26] Hughes JMB, Bates DV, Historical review of the carbon monoxide diffusing capacity(D_{LCO}) and its membrane (D_M) and red cell (θV_C) components, *Respiratory Physiology and Neurobiology* 138:115-142 (2003).

- [27] Hughes JMB, The single breath transfer factor (TLCO) and the transfer coefficient (K_{CO}): a window onto the pulmonary circulation, *Clin.Physiol.Funct.Imaging*. 23:63-71 (2003)
- [28] Hughes JM , Pride NB, In defence of the carbon monoxide diffusion coefficient $K_{CO}(TL/V_A)$, *Eur. Resp J*. 17:168-174 (2001).
- [29] Ogilvie CM, Forster RE, Blakemore WS, Morton JW, A standardized breath holding technique for the clinical measurement of the diffusing capacity of the lung for carbon monoxide, *J.Clin.Invest*. 36 :1-17. (1957).
- [30] Krogh M, The diffusion of gases through the lungs of man, *J.Physiol*.49: 271-296(1915).
- [31] American Thoracic Society, Single breath carbon monoxide diffusing capacity (Transfer factor), *Am J Respir Crit Care Med*. 152:2185-2198. (1995).
- [32] Roughton FJW, Forster RE, Relative importance of diffusion and chemical reaction rate of exchange of gases in the human lung, with special reference to true diffusing capacity of pulmonary membrane and volume of blood in the lung capillaries, *J.Appl.Physiol* 11:290-302 (1957).
- [33] Roughton FJW, Forster RE, Cander L, rates at which carbon monoxide replaces oxygen from combination with human hemoglobin in solution and in the red cell, *J.Appl.Physiol*. 11;269-276 (1957).
- [34] Johnson RL, Spicer WS, Bishop JM, Forster RE, Pulmonary capillary blood flow and diffusing capacity during exercise, *J.Appl.Physiol*. 15 :893-902 (1960).

- [35] Zavorsky GS, Quiron KB, Massarelli PS, Lands LC, The Relationship Between Single-Breath Diffusion Capacity of the Lung for Nitric Oxide and Carbon Monoxide During Various Exercise Intensities, *Chest*. 125: 1019 – 1027(2004).
- [36] Stahl WR, Scaling of respiratory variables in mammals, *J.Appl.Physiol*. 22:453-460(1967).
- [37] Agusti AGN. Interstitial Lung Diseases. pp 263-284. In : *Pulmonary and peripheral gas exchange in health and disease*. Roca J, Rodriguez-Roisin R, Wagner PD (editors).Vol 148 in the series « *Lung biology in health and disease* » Marcel Dekker (2000).
- [38] Mohsenifar Z, Lee SM, Diaz P, Criner G, Scirba F, Ginsburg M, Wise RA, Single-breath diffusing capacity of the lung for carbon monoxide: a predictor of Pa_O₂, maximum work rate, and walking distance in patients with emphysema, *Chest*. 123(5):1394-400 (2003).
- [39] Fitting JW, Transfer factor for carbon monoxide:a glance behind the scene, *Swiss Medical Weekly* 134:413-418(2004).
- [40] Beckles MA, Spiro SG, Colice GL, Rudd RM, The physiologic evaluation of patients with lung cancer being considered for resectional surgery, *Chest*. 123(1 Suppl):105S-114S (2003).
- [41] Centres for Disease Control and Prevention, Acute pulmonary hemorrhage among infants-Cleveland Jan 1993-Nov 1994,*MMWR* 43:881-3 (1994).
- [42] Etzel RA, Montana E, Sorenson WG, Kullman GJ, Allan TM, Dearborn DG, Acute pulmonary hemorrhage in infants associated with with exposure to *Stachybotrys atra*, *Arch. Pediatr.Adol.Med*. 152:757-762 (1998).

- [43] Hossain MA, Ahmed MS, Ghannoum MA, Attributes of *Stachybotrys chartarum* and its association with human disease, *J. Allergy Clin. Immunol.* 113: 200-208 (2004).
- [44] Gregory L, Pestka JL, Dearborn DG, Rand TG, Localization of satratoxin_G in *Stachybotrys chartarum* spores and spore impacted mouse lung using immunocytochemistry, *Toxicol Pathology* 32:26-34 (2004).
- [45] M. Nikulin M, Reijula K, Jarvis BB, Hintikka EL, Experimental mycotoxicosis in mice induced by *Stachybotrys atra*, *Fundam Appl Toxicol.* 35:182-188(1997).
- [46] Yike I, Miller MJ, Sorenson WG, Walenga R, Tomashefski JF, Dearborn DG, Infant animal model of mycotoxicosis induced by *Stachybotrys chartarum*, *Mycopathologia* 154:139-152 (2001).
- [47] Rand TG, White K, Logan A, Gregory L, Histological, immunohistochemical and morphometric changes in lung tissue in juvenile mice experimentally exposed to *Stachybotrys chartarum* spores, *Mycopathologia* 156: 119-131(2002).
- [48] C. Rao C, Burge HA, Brain JD, The time course of response to intratracheally instilled toxic *Stachybotrys chartarum* spores in rats, *Mycopathologia* 149: 27-34 (2000).
- [49] Thrall RS, Scalise PJ, Bleomycin. pp 231-292. In : *Pulmonary fibrosis*. Sem Hin Phan and RS Thrall (editors). Vol 80 in the series « *Lung biology in health and disease* » Marcel Dekker (1995).
- [50] Evans MJ, Oxidant gases. *Environ. Health Perspect.* 55 :85-95 (1984).
- [51] Sandy MS, Moldeus P, Ross D, Smith MT, Role of redox cycling and lipid peroxidation in biperidyl herbicide cytotoxicity. *Biochem. Pharmacol.* 35 :3095-3101 (1986).

- [52] McCord JM, Oxygen derived free radicals in postischemic tissue injury. *N.Eng.J.Med.* 312 :159-163 (1985).
- [53] Lemaire I, Silica- and Asbestos-induced pulmonary fibrosis. pp 319-346. In : *Pulmonary fibrosis*. Sem Hin Phan and RS Thrall (editors).Vol 80 in the series « *Lung biology in health and disease* » Marcel Dekker (1995).
- [54] Pickrell JA, Abdel-Mageed AB, Radiation induced pulmonary fibrosis pp 363-375. In : *Pulmonary fibrosis*. Sem Hin Phan and RS Thrall (editors).Vol 80 in the series « *Lung biology in health and disease* » Marcel Dekker (1995).
- [55] Nader ND, Knight PR, Davidson BSA, Safaee SS, Steinhorn DM, Systemic perfluorocarbons suppress the acute lung inflammation after gastric acid aspiration in rats, *Anesth. Analg.* 90 : 356-361 (2000).
- [56] Cherubini A, Bifone A, Hyperpolarized xenon in biology, *Prog. Nuc.Mag.Res. Spec.* 42 : 1-30 (2003).
- [57] Pietraß T, Gaede HC, Optically polarized ¹²⁹Xe in NMR spectroscopy, *Adv. Mater.* 7:826-838 (1995).
- [58] Goodson BM, Using injectable carriers of laser-polarized noble gases for enhancing NMR and MRI, *Concepts Magn.Reson.* 11(4): 203-223 (1999).
- [59] Goodson BM Kaiser L, Pines A, NMR and MRI of laser polarised noble gases in molecules, materials and medicine, *Magnetic resonance and brain function: approaches from physics*, IOP press (1999).
- [60] Chupp T, Swanson S, *Advances in atomic, molecular and optical physics*, 45: 41(2001)
- [61] Mair RW, Walsworth RW, *Appl. MagnReson.*2:159-167 (2002).

- [62] Goodson BM, Nuclear Magnetic Resonance of Laser-Polarized Noble Gases in Molecules, Materials, and Organisms, *J.Magn.Reson.*155:157-216 (2002).
- [63] Landon C, Berthault P, Vovelle F, Desvaux H, Magnetization transfer from laser-polarized xenon to protons located in the hydrophobic cavity of the wheat nonspecific lipid transfer protein, *Protein Sci.* 10: 762-770 (2001).
- [64] Bowers CR, Storhaug V, Webster CE, Bharatam J, Cottone A, Gianna R, Betsey K, Gaffnet BJ, Exploring Surfaces and Cavities in Lipxygenase and Other Proteins by Hyperpolarized Xenon-129 NMR , *J.Am.Chem.Soc.* 121:9370-9377(1999).
- [65] Wolber J, Cherubini A, Dzik-Juras AS, Leach MO, Bifone A, Spin-lattice relaxation of laser-polarized xenon in human blood, *Proc.Natl.Acad.Sci.USA.*96:3664-3669 (1999).
- [66] Rubin SM, Spence MM, Goodson BM, Wemmer DE, Pines A, Evidence of nonspecific surface interactions between laser-polarized xenon and myoglobin in solution, *Proc.Natl.Acad.Sci. USA.* 97:9472-9475(2000).
- [67] Wilson GJ, Santyr GE, Anderon ME, DeLuca PM, Longitudinal relaxation times of ¹²⁹Xe in rat tissue homogenates at 9.4 T, *Magn. Reson. Med.*41:933-938(1999).
- [68] Abraham MH, Kamlet MJ, Taft RW, Doherty RM, Weathersby PK, Solubility properties in polymers and biological media. 2. The correlation and prediction of the solubilities of nonelectrolytes in biological tissues and fluids, *J.Med.Chem.* 28:865-870 (1985).
- [69] Zhao L, Venkatas AK, Balamore D, Jolesz FA, Albert MS. *Proc ISMRM, 6th meeting* 1908(1998).

- [70] Wolber J, Rowland IJ, Leach MO, Bifone A, Perfluorocarbon emulsions as intravenous delivery media for hyperpolarized xenon, *Magn. Reson. Med.* 41:442-449 (1999).
- [71] Callot V, Canet E, Brochet J, Viallon M, Humblot H, Briquet A, Tournier H, Cremillieux Y, MR perfusion imaging using encapsulated laser-polarized ^3He , *Magn Reson. Med.* 46:535-540(2001).
- [72] Duhamel G, Choquet P, Grillon E, Lamalle L, Leviel JL, Ziegler A, Constantinesco A, Xenon-129 MR imaging and spectroscopy of rat brain using arterial delivery of hyperpolarized xenon in a lipid emulsion, *Magn. Reson. Med.* 46:208-212(2001).
- [73] Swanson SD, Rosen MS, Coulter KP, Welsh RC, Chupp TE, Distribution and dynamics of laser polarized ^{129}Xe magnetization *in vivo*, *Magn Reson Med.* 42:1137-1145 (1999).
- [74] Kastler, A, Quelques suggestions concernant la production optique et la detection optique d'une inegalite de population des niveaux de quantification spatiale des atomes. Application a l'experience de Stern et Gerlach et a la resonance magnetique. *J Phys Radium* 11:255-265 (1950).
- [75] Grover BC, Noble gas NMR detection through noble-gas rubidium hyperfine contact interaction. *Phys. Rev, Lett.* 40:391-392 (1978).
- [76]. Moller HE, Chen XJ, Saam B, Hagspiel KD, Johnson GA, Altes TA, de Lande EE, Kauczor HU, MRI of the lungs using hyperpolarized noble gases, *Magn. Reson. Med.* 47:1029-1051(2002).

- [77] Happer W, Miron E, Schaefer S, Schreiber D, van Wijngaarden WA, Zeng X, Polarization of the nuclear spins of noble gas atoms by spin exchange with optically pumped alkali metal atoms, *Phys Rev A*.29:3092-3110 (1984).
- [78] Driehuys B,Cates GD,Happer W, Surface relaxation mechanisms of laser- polarized ^{129}Xe , *Phys.Rev.Lett.*74:4943-4946 (1995).
- [79] Walker TG, Happer W, Spin exchange optical pumping of noble gas nuclei, *Rev.Mod.Phys.* 69:629-642 (1997).
- [80] Gatzke M, Cates GD, Driehuys BF, Happer W, Saam B, Extraordinarily slow nuclear spin relaxation in frozen laser polarized ^{129}Xe , *Phys. Rev. Lett.* 70 :690-693(1993).
- [81] Kuzma NN, Patton B, Raman K, Happer W, Fast nuclear spin relaxation in hyperpolarized Solid ^{129}Xe , *Phys. Rev.Lett.* 88:147602 (2002).
- [82] Cates GD, Benton DR, Gatzke M, Happer W, Hasson KC, Newbury NR., Laser production of large nuclear-spin polarization in frozen xenon, *Phys.Rev.Lett.*65:2591-2594(1990).
- [83] Lang S , Moudrakovski IL, Ratcliffe CI, Ripmeester JA, Santyr G, Increasing the spin-lattice relaxation time of hyperpolarized xenon ice at 4.2 K, *Appl. Phys. Lett.* 80:886 (2002).
- [84] Wagshul ME, Button TM, Li HF, Liang Z, Springer CF, Zhong K, Wishnia A, *In vivo* MR imaging and spectroscopy using hyperpolarized ^{129}Xe , *Magn.Reson. Med.* 36;183-191(1996).
- [85] Sakai K, Bilek AM, Oteiza E, Walsworth RL, Balamore D, Jolosz FA, Albert MS, Temporal Dynamics of Hyperpolarized ^{129}Xe resonances in living rats, *J. Mag.Res.series B.* 111:300-304(1996).

- [86] Ruppert K, Brookeman JR, Hagspiel KD, Driehuys B, Mugler III, JP, NMR of hyperpolarized ^{129}Xe in the canine chest: spectral dynamics during a breath-hold, *NMR Biomed.* 13:220-228 (2000).
- [87] Ruppert K, Brookeman JR, Hagspiel KD, Mugler III JP, Probing lung physiology with xenon polarization transfer contrast (XTC), *Magn.Reson. Med.* 44:349-357(2000).
- [88] Ruppert K, Mata JF, Brookeman JR, Hagspiel KD, Mugler III JP, Matching experimental data to a 1D ^{129}Xe gas exchange model, *Proc. ISMRM* 11:1686 (2004).
- [89] Ruppert K, Mata JF, Brookeman JR, Hagspiel KD, Mugler III JP, *Proc. ISMRM* 10(2003).
- [90] Ruppert K, Mata JF, Brookeman JR, Hagspiel KD, Mugler III JP, Exploring Lung function with hyperpolarized ^{129}Xe nuclear magnetic resonance, *Magn.Reson.Med.* 51:676-687(2004).
- [91] Mansson S, Wolber J, Driehuys B, Wollmer P, Golman K, Characterization of diffusing capacity and perfusion of the rat lung in a lipopolysaccharide disease model using hyperpolarized ^{129}Xe , *Magn Res.Med.* 50:1170-1179 (2003).
- [92] Ruppert K, Mata J, Brookeman J, Hagspiel K, Mugler JP III. Matching experimental data to a 1D ^{129}Xe gas exchange model. *Proc. ISMRM 11th Annual Meeting* 1686 (2004).
- [93] Rabi II, Zacarias JR, Millman S, Kusch P. A new method of measuring nuclear magnetic moments. *Phys Rev.* 53: 318 (1938)
- [94] Bloch F, Nuclear induction, *Phys Rev.* 70:460-474 (1946)
- [95] Hahn EL, Spin echoes, *Phys Rev.* 80:580-594 (1950)
- [96] Abragam A, *The principles of nuclear magnetism.* Oxford (1961)
- [97] Slichter CP, *Principles of magnetic resonance, 3rd edition,* Springer Verlag (1990)

- [98] Nishimura DG, *Principles of magnetic resonance imaging* ©DG Nishimura (1996)
- [99] Haacke EM, Brown RW, Thompson MR, Venkatesan R, *Magnetic resonance imaging: physical principles and sequence design*. John Wiley and Sons (1999).
- [100] Rabi II, Ramsey NF, Schwinger J., Rotating coordinates in magnetic resonance problems, *Rev. Mod.Phys.* 26:167-171 (1954).
- [101] Bracewell RN, *The Fourier transform and its applications*, 3rd edition.McGraw-Hill (1999).
- [102] Lauterbur PC, Image formation by induced local interactions:examples employing nuclear magnetic resonance, *Nature*. 242:190-191 (1973).
- [103].Moller HE, Chen XJ, Saam B, Hagspiel KD, Johnson GA, Altes TA, de Lande EE, Kauczor HU, MRI of the lungs using hyperpolarized noble gases, *Magn. Reson. Med.* 47:1029-1051(2002).
- [104] Zhao L, Mulkern R, Tseng C-H, Williamson D, Patz S, Kraft ., Walsworth RL, Jolezsz FA , Albert MS, Gradient-echo imaging considerations for hyperpolarized ¹²⁹Xe, *J. Magn. Reson.B* 113:179-183 (1996).
- [105] Moller HE, Chen XJ, Chawla MS, Driehuys B, Hedlund LW, Johnson GA, Signal dynamics in magnetic imaging of the lung with hyperpolarized noble gases, *J.Magn. Reson.* 135:133-143 (1998).
- [106] Sobering GS, Shiferaw Y. *Proc. ISMRM*, 3:979 (1995).
- [107] Zhao L, Albert MS, Biomedical imaging using hyperpolarized noble gas MRI: pulse sequence considerations, *Nucl. Inst. Meth. Phys.Research.A.* 402:454-460 (1998).
- [108] Ruppert K,Mata JF, Brookeman JR, Hagspeil KD, Mugler JP III. Xenon uptake and exchange dynamics in the rabbit lung. *Proc. ISMRM* 10 (2002).

- [109] White S. Volume estimation from three dimensional ^{129}Xe magnetic resonance images, *M.Sc. Thesis, Dept of Physics, Carleton University* (2004).
- [110] White S, Cross A, Santyr G. Absolute volume estimation from 3D hyperpolarized xenon images: a Monte Carlo and phantom study. *Physics in Canada*. 60:91(2004).
- [111] Cross AR, Santyr G, Rand T, Cron G, Wallace J, Abdeen N, *In vivo* spectroscopy of ^{129}Xe in fungal spore inflamed rat lungs. *Proc. ISMRM* 11:1394 (2003).
- [112] Moudrakovski I, Lang S, Ratcliffe C I, Simard B, Santyr G, Ripmeester J A, Chemical shift imaging with continuously flowing hyperpolarized xenon for the characterization of materials. *J. Magn. Res.* 144:372-7 (2000).
- [113] Brandt S, Data Analysis. Springer , New York (1999).
- [114] Fogiel M, Statistics Problem Solver. Research and Education Association, Piscataway NJ, (1994).
- [115] Takazawa J, Miller FJ, O'Neil JJ. Single breath diffusing capacity and lung volumes in small laboratory mammals. *J. Appl. Physiol.* 48:1052-1059 (1980).
- [116] Gross KB, White HJ. Pulmonary functional and morphological changes induced by a 4-week exposure to 0.7 ppm ozone followed by a 9-week recovery period. *J Toxicol Environ Health*. 17(1):143-57 (1986).
- [117] Lam HF, Takezawa J, Gupta BN, Van Stee EW, Comparison of the effects of diquat and paraquat on lung compliance, lung volumes, and single breath diffusing capacity in the rat. *Toxicology* 18:111-123 (1980).
- [118] Pauluhn J, Baumann M, Hirth-Dietrich C, Rosenbruch M, Rat model of lung fibrosis: comparison of functional, biochemical, and histopathological changes four months after single irradiation of the right hemithorax. *Toxicology* 161:153-165 (2001).

[119] Mugler JP III, Driehuys B, Brookeman JR, Cates G, Berr SS, Bryant RG, Caniel TM, deLange EE, Wagshul ME, MR imaging and spectroscopy using hyperpolarized ^{129}Xe gas: preliminary human results. *Magn. Reson. Med.* 37:809-815 (1997).